IMPROVING ULTRASONIC IMAGING USING NOVEL CODED EXCITATION TECHNIQUES

BY

JOSE RAFAEL SANCHEZ

DISSERTATION

Submitted in partial fulfillment of the requirements
for the degree of Doctor of Philosophy in Electrical and Computer Engineering
in the Graduate College of the
University of Illinois at Urbana-Champaign, 2010

Urbana, Illinois

Doctoral Committee:

Assistant Professor Michael L. Oelze, Chair
Associate Professor Minh N. Do
Assistant Professor Jonathan J. Makela
Professor William D. O'Brien, Jr.

ABSTRACT

In ultrasound imaging, the axial resolution depends on the source bandwidth. Recently, a novel coded excitation and pulse compression technique, known as Resolution Enhancement Compression (REC), was developed. REC enhances the -6 dB bandwidth of an ultrasonic imaging system. In this dissertation, the limitations of the REC technique were explored and specific imaging applications were examined.

Several factors that could limit the improvements in ultrasonic imaging afforded by REC were assessed. First, it was hypothesized that a Wiener filter could adversely affect the compression performance of coded excitation because it had the potential to boost the harmonics due to nonlinear distortion. When the Wiener filter operated near an inverse filter the harmonics were boosted, resulting in increased sidelobes. Pre-filtering of the harmonics was found to solve this problem. Second, it was hypothesized that the larger the bandwidth boost desired, the smaller the voltage that could be applied at the center frequency. When doubling the bandwidth, the center frequency voltage was 6 dB below the band edges of the pre-enhanced chirp. Finally, the effects of attenuation were evaluated. Because of the attenuation, a larger shift in the center frequency due to the larger bandwidth was identified.

Several applications for the REC technique in biomedical imaging were explored. It was hypothesized that the variance of the speckle could be reduced further when using frequency compounding and REC. By using the bandwidth enhancement delivered by REC, the trade off between improved contrast and axial resolution was extended. Similarly, REC was combined with quantitative ultrasound (QUS) techniques to improve parametric images of estimated scatterer diameter. Larger bandwidths were observed to lead to a smaller variance in spectral estimates, thereby improving QUS image contrast.

Finally, novel techniques for improving the compression of codes in ultrasonic imag-

ing were developed and assessed. The effects of the spatially varying nature of a transducer's impulse response and echo signal-to-noise ratio (eSNR) throughout the depth of field of the source were evaluated. Significant improvements in image quality were realized through the use of Wiener filters that accounted for the spatially varying eSNR.

To my wife Mary Ann, my dogs Smudge and Jaxx,
my family, and my friends,
who kept my poles inside the unit circle.

ACKNOWLEDGMENTS

I would like to thank my PhD adviser Dr. Michael L. Oelze for his tremendous support throughout the last four and a half years of my life. Dr. Oelze taught me a wealth of knowledge from an academic perspective and a significant amount of research skills, which were critical in the completion of my degree. Dr. Oelze always pushed me to strive for the best, which was frustrating at times, but I grew into a better researcher as a result of his actions. I really appreciated how patient he was when reading my manuscripts. It was such a delight to work with him, that I hope we will still collaborate in the future.

I would like to thank the members of my doctoral committee: Dr. Michael Oelze, Dr. Minh N. Do, Dr. Jonathan J. Makela, and Dr. William D. O'Brien Jr. Their comments and suggestions were greatly appreciated, specifically, the ones made to improve the clarity of this dissertation. All four of these individuals are great investigators with an overwhelming amount of knowledge and skills.

I would like to acknowledge the hard work and dedication of Darren Pocci who assisted me with the quantitative ultrasound study, Marko Orescanin who assisted me with the creation of a cone phantom, and Roberto J. Lavarello who helped me significantly during the final stretch of my Ph.D. It was a pleasure for me to work with all the wonderful people from the Bioacoustics Research Laboratory (BRL) at the University of Illinois.

I would like to thank my family for their support. I love you all and hope to spend more time with you.

I would like to thank my wife, Mary Ann. She has been the main support behind this PhD. She was there when I was frustrated, happy, angry, and excited. Most importantly, she was there when I needed her. She is the inspiration in my life. My success belongs

to her.

I would like to thank various organizations for the funding support they provided during my graduate studies: National Institutes of Health and the SURGE Fellowship program at the University of Illinois.

TABLE OF CONTENTS

CHAPTER 1

INTRODUCTION

Spatial resolution in ultrasonic imaging is one of many parameters that impact image quality. Therefore, mechanisms to improve system spatial resolution could result in improved ultrasound imaging and diagnostic performance including earlier cancer detection and screening, accuracy in tumor staging, and accuracy of thrombus detection and many other improvements to diagnostic imaging [1]. Spatial resolution in an ultrasonic imaging system is dictated by the beam and focal properties of the source (focal number, source bandwidth, etc.), tissue attenuation, nonlinearity of the medium, tissue inhomogeneity (phase abberation, spatial variations in the refractive index), and sound speed [1].

In ultrasound, axial resolution is improved as the bandwidth of the transducer is increased, which typically occurs for higher center frequencies. However, the attenuation of sound typically increases as frequency increases, which results in a decrease in penetration depth. Therefore, there is an inherent tradeoff between spatial resolution and penetration in ultrasonic imaging. One way to increase the penetration depth without reducing axial resolution is by increasing the excitation pulse amplitude. However, increased excitation amplitude results in increased pressure levels that could result in unwanted bioeffects, e.g., heating or damage to tissues [2]. Therefore, increasing the excitation pulse amplitude is not always a viable solution.

An alternate solution would be to increase the excitation pulse duration by using coded excitation which increases the total transmitted energy and allows for the minimization of the transmitted peak power [3, 4]. However, elongating the signal duration has the negative effect of decreasing the axial resolution of the ultrasonic imaging system. In order to restore the axial resolution after excitation with a coded signal, pulse compression is used. Pulse compression can be realized by using many filtering meth-

ods such as matched filtering, inverse filtering, and mismatched filtering. The main disadvantage of using coded excitation and pulse compression would be the introduction of range sidelobes that can appear as false echoes in an image. The introduction of range sidelobes is a detriment to ultrasonic image quality because it can reduce the contrast resolution [5]. The main advantage cited for using coded excitation is that it is known to improve the echo signal-to-noise ratio (eSNR) by increasing the time-bandwidth product (TBP) of the coded signal. This improvement in eSNR results in greater depth of penetration in the range of a few centimeters for ultrasonic imaging and improved image quality; i.e., increased eSNR can actually increase contrast resolution. Furthermore, this increase in penetration depth allows the possibility of shifting to higher frequencies with larger bandwidths in order to increase the spatial resolution at depths where normally it would be difficult to image.

1.1 Coded Excitation: Literature Review

Coded excitation and pulse compression techniques have been used successfully in radar since the early 1950s. Originally, radar work performed at Sperry Gyroscope Company [6] used an FM chirp to obtain a 10 dB increase in average signal power, all the while increasing the range detection by 78% with their coded excitation and pulse compression scheme. Other areas such as communications use spread spectrum techniques that utilized phase codes with a transversal filter for pulse compression.

In ultrasound, coded excitation (Golay code) and pulse compression was first tackled by Takeuchi [7, 8] in 1979. In this work, Takeuchi established the differences in signal processing between radar and ultrasound coded systems; specifically, clutter suppression vs. object detection, and TBPs on the order of 10^4 vs. 20, respectively. Takeuchi attributed the limitation in the TBP in ultrasonic imaging to the interaction of frequency-dependent attenuation in tissues and the imaging system time-gain compensator. Although not discussed in Takeuchi's research, a limited TBP results in a decrease of signal-to-noise ratio. In addition, ultrasound suffers from hardware complexity and implementation problems. As a result, coded excitation was not studied in the medical ultrasound community until the 1990s.

In 1992, O'Donnell [9] used a coded excitation (pseudochirp) and pulse compression

(equalization filtering) technique to improve the eSNR of an ultrasound phased array imaging system by 15-20 dB. The coded excitation and pulse compression technique contained sidelobes around the -45 dB amplitude level. Nonetheless, the system developed by O'Donnell still had some stringent requirements for practical implementation and significant sidelobes levels.

By the late 1990s, a plethora of manuscripts regarding the subject of coded excitation and pulse compression in ultrasound had been published. In 1994, Rao [10] extended the work performed by Takeuchi by evaluating the effects of attenuation on a linear chirp, which resulted in eSNR degradation. Pollakowski and Ermert [11] evaluated the use of nonlinear coded signals that match the spectrum of the ultrasonic transducer. In 1996, Shen and Ebbini [12, 13] developed a new approach for the compression using the pseudo-inverse operator. Moreover, Passmann and Ermert [14] developed a system that improved dermatological and ophthalmological ultrasound images by using a nonlinear frequency modulated chirp along with very high frequencies. Haider et al. [15] developed a pulse elongation and deconvolution scheme that used a stabilized inverse filter to reduce sidelobe artifacts.

In 2005, *IEEE Transactions on Ultrasonics, Ferroelectrics, and Frequency Control* published a special issue on coded waveforms in ultrasonic imaging that included a comprehensive study on coded excitation and pulse compression by Misaridis and Jensen [5, 16, 17]. Misaridis and Jensen established the basic principles of pulse compression, evaluated design methods of linear FM signals and mismatched filters, and investigated methods to increase the frame rate in ultrasonic imaging when using modulated excitation signals. In 2006, Oelze [18] developed a coded excitation and pulse compression scheme that improves the axial resolution of an ultrasonic imaging system without introducing large range lobes. The technique developed by Oelze, which is known as resolution enhancement compression or REC, is the foundation of this dissertation; therefore, a more detailed explanation is provided in the following section.

1.2 REC: Resolution Enhancement Compression

REC [18] is a coded excitation and pulse compression technique that uses convolution equivalence (shown in Fig. 1.1) to improve the axial resolution and enhance the band-

width of an ultrasonic imaging system. In REC, a desired pulse-echo impulse response, $h_2(t)$ (Fig. 1.1(d)), is synthetically generated so that time duration is less when compared to the true ultrasonic system pulse-echo impulse response, $h_1(t)$ (Fig. 1.1(a)). As a result, the corresponding bandwidth of $h_2(t)$ is larger than the bandwidth of $h_1(t)$. To obtain the desired impulse response for the imaging system, a pre-enhanced chirp, $v_{pre}(t)$ (Fig. 1.1(b)), is used to excite the source. The pre-enhanced chirp is obtained through convolution equivalence which is described by the following expression:

$$v_{pre}(t) * h_1(t) = v_{lin}(t) * h_2(t), \tag{1.1}$$

where $v_{lin}(t)$ is the linear chirp shown in Fig. 1.1(e). The pre-enhanced chirp is used to selectively excite an ultrasonic source with different energies at chosen frequencies. By exciting the transducer with the pre-enhanced chirp, the bandwidth can be enhanced due to the increase of energy in the frequency bands that normally would be filtered in some measure by the bandpass nature of the transducer. Conceptually, to obtain a constant eSNR per frequency channel across the desired bandwidth, the additional amount of energy required on transmit at the outer frequency bands will depend on the original transducer's bandwidth and the amount of bandwidth boost desired.

Once the source is excited with a pre-enhanced chirp, the received echo is compressed using a Wiener filter based on convolution equivalence. The resulting backscattered signal has an impulse response $h_2(t)$. Wiener filtering is described by the following equation:

$$\beta_{REC}(f) = \frac{V_{lin}^{'*}(f)}{|V_{lin}^{'}(f)| + \gamma \overline{eSNR}^{-1}(f)}, \tag{1.2}$$

where f is frequency, and γ is a smoothing parameter that controls the tradeoff between bandwidth enhancement (axial resolution), gain in eSNR, and sidelobe levels. $V_{lin}^{'}(f)$ is the Fourier spectrum of a modified linear chirp that is used to restore convolution equivalence as the signal is slightly altered and filtered by electronics. $V_{lin}^{'}(f)$ is defined as:

$$V_{lin}^{'}(f) = \frac{H_2^*(f)}{|H_2(f)|^2 + |H_2(f)|^{-2}} \cdot H_{out}(f), \tag{1.3}$$

where $H_2(f)$ is the Fourier spectrum of the desired response, $h_2(t)$, and $H_{out}(f)$ is the Fourier spectrum of an echo obtained from a planar reflector located at the focus upon

excitation with a pre-enhanced chirp. $\overline{eSNR}(f)$ is the average eSNR [19] per frequency channel and is defined as:

$$\overline{eSNR}(f) = \frac{|H_{2c}(f)|^2 E\{|F(f)|^2\}_f}{E\{|\eta(f)|^2\}_\eta}, \tag{1.4}$$

where $|F(f)|^2$ is the power spectral density (PSD) of the object function, $|\eta(f)|^2$ is the PSD of the noise, and $|H_{2c}(f)|^2$ is the PSD of the echo signal over noise, $h_{2c}(t)$, which is defined as

$$h_{2c}(t) = E\{g(t)\}_{noise}, \tag{1.5}$$

where E is the expectation value of the argument and $g(t)$ is the echo signal over noise. To obtain $\overline{eSNR}$ experimentally, a measure of the noise per frequency channel is first obtained by estimating the mean of the PSD of a noise measurement from a water bath that contains no imaging target while using the same equipment settings. Thereafter, the signal (which contains noise) power is divided by the noise per frequency channel to get $\overline{eSNR}$.

Figure 1.2 illustrates the enhanced bandwidth of REC by displaying the PSD of the conventional pulsing (CP) and REC waveforms due to a reflection from a point scatterer in a simulated attenuating medium. In the simulation, the attenuation parameter α was set to 0.5 dB $\text{MHz}^{-1}\text{cm}^{-1}$. The simulated source has a center frequency of 10 MHz and the point scatterer is located at an axial distance of 50 mm. The bandwidths at -6 dB were 7.2 MHz and 12.1 MHz for CP and REC, respectively. The original source bandwidths at -6 dB before the inclusion of attenuation and scattering effects into the simulation were 7.9 MHz and 15.5 MHz for CP and REC, respectively. This result illustrated that with REC the bandwidth can be enhanced over conventional ultrasonic imaging methods.

1.3 Outline of Research Topic

A proof of concept for the REC technique has been developed by Oelze [18]. However, the impact that the REC technique may have in improving the diagnostic capabilities of conventional and quantitative ultrasound (QUS) imaging has not been established. Therefore, the overall goal of the studies in this dissertation were classified into two

categories:

1. Characterization of the REC technique: The REC technique allows the bandwidth and the axial resolution of an ultrasonic imaging system to be enhanced. An important piece of information regarding the use of the REC technique in diagnostic imaging would be to establish the practical limitations of the technique. To characterize the technique, some imaging quality metrics must be used to quantify the improvements obtained or to establish potential tradeoffs. The effects of nonlinear distortion and frequency-dependent attenuation on the pre-enhanced chirp were evaluated. The potential of transducer heating by excitation of a pre-enhanced chirp was evaluated. Finally, the effects of the spatially varying nature of a transducer's impulse response and the spatial dependence of the eSNR throughout the image were evaluated. These studies represent an in-depth examination of the limitations of coded excitation for ultrasound imaging in general and for the REC technique specifically.

2. Exploration of potential applications where REC could be beneficial: Three applications were evaluated where the improved axial resolution and increased bandwidth available from REC could be beneficial. First, REC was evaluated in combination with frequency compounding to extend the tradeoffs between axial resolution and improved contrast. In the second application, REC was assessed for improving contrast and spatial resolution in QUS imaging.

This dissertation is organized into five parts: introductory remarks (Chapter 1), characterization of the REC technique (Chapter 2), applications where the larger bandwidth obtained using REC helped to improve ultrasound images (Chapter 3), the spatially varying Wiener filter (Chapter 4), a brief summary of the findings (Chapter 5).

1.4 Figures

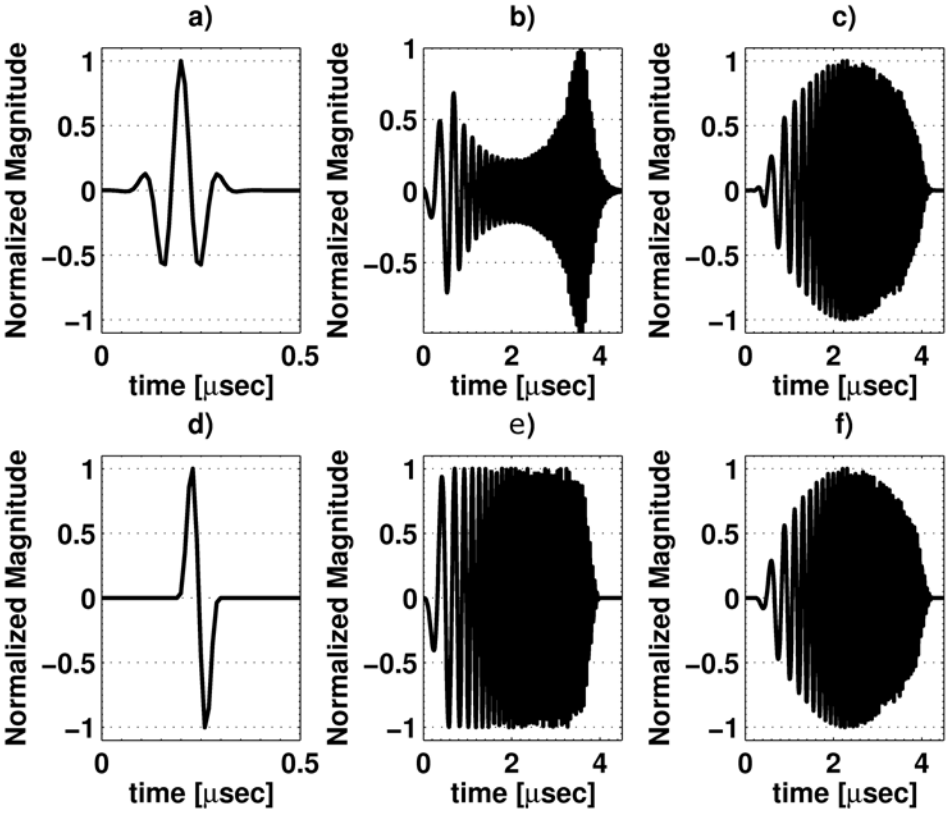

Figure 1.1: Convolution equivalence scheme from a MATLAB simulation: (a) pulse-echo impulse response for a source with an 80% -6-dB bandwidth, (b) pre-enhanced chirp used to excite the 80% bandwidth source, (c) convolution of 80% source with pre-enhanced chirp, (d) pulse-echo impulse response of a desired source with a 150% -6-dB bandwidth, (e) linear chirp used to excite the 150% bandwidth source, (f) convolution of 150% source with linear chirp.

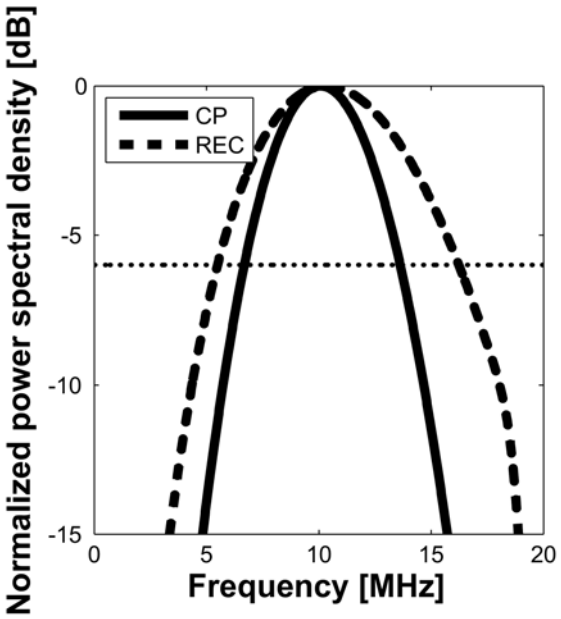

Figure 1.2: Simulated power spectrum of CP and REC (compressed) from a point scatterer in an attenuated medium with $\alpha = 0.5$ dB $\text{MHz}^{-1}\text{cm}^{-1}$ using a 10 MHz source. The frequency shift for REC and CP were insignificant as the shape of the frequency response was not symmetrical.

CHAPTER 2

CHARACTERIZATION OF THE REC TECHNIQUE

2.1 The Effects of Nonlinear Distortion on the Compression of REC Echoes

2.1.1 Introduction

In ultrasound, when the excitation waveform is low in pressure amplitude, wave propagation is described by the linear wave equation. In the development of the linear wave equation, the higher order terms in the general acoustic equations (equation of state, equation of continuity, Euler's equation of force) are negligible. The one-dimensional linear wave equation [20] is

$$\frac{\partial^2 \xi}{\partial t^2} = c_0 \frac{\partial^2 \xi}{\partial x^2} \tag{2.1}$$

where c_0 is the small signal speed of sound, ξ is the particle displacement, and t is time.

In cases where low pressure amplitudes are used, the eSNR may be relatively low, which in turn provides poor sensitivity. Therefore, larger pressure amplitudes may be necessary to improve the eSNR but at the expense of possible nonlinear effects of the medium that distort the pressure wave. To further understand the effects of nonlinearity, the development of the linear wave equation must be modified to include higher order terms.

In the derivation of the linear wave equation the higher order terms from the Taylor series expansion of the equation of state were assumed to be negligible. For the nonlinear equation of state the quadratic and linear terms of the Taylor series are used. Specifically, the nonlinear equation of state [21] is expressed as

$$p = As + \frac{B}{2}s^2, \tag{2.2}$$

where s is the condensation. Furthermore, A and B are defined as:

$$A = \rho_0(\frac{\partial P}{\partial \rho}) = \rho_0 c_0^2 \tag{2.3}$$

$$B = \rho_0^2(\frac{\partial^2 P}{\partial \rho^2}), \tag{2.4}$$

where ρ_0 is the ambient density, ρ is density, and P is the total pressure. Moreover, the one-dimensional nonlinear continuity equation [21] can be described by

$$s = -\frac{\partial \xi}{\partial x}(1 - \frac{\partial \xi}{\partial x}), \tag{2.5}$$

where x is the spatial coordinate. If expression (2.5) was substituted into (2.2) and then only the linear and quadratic terms were kept, the resulting development can be obtained:

$$p = -A\frac{\partial \xi}{\partial x} + A\beta_n(\frac{\partial \xi}{\partial x})^2, \tag{2.6}$$

where β_n [22] is a parameter that quantifies the nonlinear properties of the medium and is referred to as the Beyer parameter or the coefficient of nonlinearity. The Beyer [22] parameter is given by

$$\beta_n = 1 + \frac{B}{2A}, \tag{2.7}$$

where the ratio B/A [20] is

$$B/A = \frac{\rho_0}{c_0^2}(\frac{\partial^2 P}{\partial \rho^2}). \tag{2.8}$$

The expression in (2.6) can be substituted into the 1D Euler's equation [20] which yields

$$-\nabla_x p = -\frac{\partial p}{\partial x}. \tag{2.9}$$

The resulting expression is the nonlinear wave equation:

$$\frac{\partial^2 \xi}{\partial t^2} = c\frac{\partial^2 \xi}{\partial x^2}, \tag{2.10}$$

where c is defined as

$$c = c_0[1 - 2\beta_n(\frac{\partial \xi}{\partial x})]. \tag{2.11}$$

A comparison between the linear and nonlinear wave equations suggests that any vari-

ation in the pressure is a result of changes in the speed of sound. In fact, the speed of sound term can be approximately written as [21]

$$c = c_0 + \beta_n u \tag{2.12}$$

where u is the particle velocity. For a linear system, β is zero and the nonlinear wave equation reverts to the classical wave equation. In the nonlinear case, the speed of sound will be a function of the small signal speed of sound and particle velocity. For a plane wave, pressure is proportional to particle velocity. Therefore, the nonlinear effects arise from the fact that the speed of the wave is a function of pressure. The compressional portion of the pressure wave travels faster than the rarefactional portion, which causes the overall waveform to distort as shown in Fig. 2.1. This distortion comes from the transfer of energy from the fundamental into higher harmonics. Besides nonlinear propagation resulting from the medium characteristics, odd harmonics can be generated by the crystal geometry of the transducer.

In terms of coded excitation and pulse compression, it was hypothesized that nonlinear distortion could be detrimental to the compression performance when using a Wiener filter with a smoothing parameter. If the operating point of the Wiener filter were to approach an inverse filter, then the harmonics could be significantly amplified causing a large mismatch between the excitation signal and the received signal. Nonetheless, several researchers have taken advantage of the nonlinear distortion to improve the contrast-to-tissue ratio (CTR) when using coded excitation. Borsboom et al. [23, 24] found that with a chirped excitation the response of a microbubble was 3 and 6 dB higher for the second and third harmonics, respectively, when compared to conventional pulsing techniques. In that work, compression was performed by using a matched filter based on the harmonic components resulting in a sidelobe-to-mainlobe ratio of -60 dB. Chiao and Xiaohui [3] evaluated simulations of nonlinear distortion using phase codes to quantify the tradeoff of penetration depth and resolution by using a matched filter. However, the effects that nonlinear distortion may have on the compression of coded signals when using a Wiener filter have not been fully evaluated, specifically in an experimental setting.

2.1.2 Methods and procedures

In this study, the effects of nonlinear distortion on the compression of coded excitation echoes when using a Wiener filter were evaluated. Typically, when nonlinear distortion is not present, operating the Wiener filter as an inverse filter reduces the sidelobe levels and provides the best performance in terms of axial resolution. However, an inverse filter has the side effect of boosting the noise outside of the transducer's passband. When nonlinear distortion is present, using a Wiener filter that closely approximates an inverse filter will result in amplification of the harmonics in the signal. The amplification of the harmonics from the filter could result in a loss of the axial resolution enhancement and increased sidelobe levels. One possible solution to this problem would be to prefilter the echo signals to remove the higher harmonics before applying the compression filter.

Image quality metrics

To evaluate the effects that nonlinear distortion may have on the compression of coded excitation echoes, the following image quality metrics were used:

1. Compressional-to-rarefactional pressure amplitude ratio (CRPR): CRPR is used to quantify the asymmetry in the amplitude of the pressure wave as result of nonlinear distortion [25]. CRPR was evaluated pre- and post-compression.

2. Second-harmonic-to-fundamental ratio (SHFR): SHFR is the ratio of the amplitude of the center frequency of the second harmonic to the amplitude of the center frequency of the fundamental [25]. The higher the SHFR, the more significant the nonlinear distortion will become. SHFR was evaluated pre- and post-compression.

3. Sidelobe-to-mainlobe ratio (SMR): SMR is an important metric used to determine the quality of the compression and is defined by quantifying sptial sidelobes using

$$SMR(x) = 20 \cdot \log_{10}\left(\frac{g^{'}_{sidelobe}(x)}{g^{'}_{mainlobe}(x)}\right), \tag{2.13}$$

   where $g^{'}(x)$ is the echo waveform. There is no gold standard in terms of acceptable sidelobe levels; however, [15] suggests that -45 dB is acceptable for most ultrasonic imaging purposes. For this work, short range sidelobes will be defined as those

sidelobes within one mainlobe width from the mainlobe while long range sidelobes are defined as all other sidelobes.

4. Modulation transfer function (MTF): MTF [26] is an important metric for determining axial resolution of an imaging system. MTF is the magnitude of the optical transfer function and is defined by

$$MTF(k) = \left|\frac{H(k)}{H(0)}\right|, \tag{2.14}$$

where $H(k)$ is the spatial Fourier transform of the envelope of the compressed waveform. The wave number value, k_0, where the value of the MTF curve is 0.1, is used to determine the axial resolution of the imaging system. The axial resolution is defined as

$$\lambda = 1/2 \cdot (2\pi)/k_0. \tag{2.15}$$

Experimental setup

To evaluate the effects of nonlinear distortion, experimental measurements were acquired in pulse-echo mode with a single-element (f/3) transducer (Panametrics, Waltham, MA) having a center frequency of 5 MHz and a -6 dB bandwidth of 74%. The bandwidth was increased to 148% using REC. The experimental setup consisted of generating a pre-enhanced chirp in MATLAB (The Mathworks Inc., Natick, MA). The resulting waveform was then downloaded to an arbitrary waveform generator (Tabor Electronics W1281A, Tel Hanan, Israel). The excitation signal was sampled at a rate of 100 MHz and amplified by an RF power amplifier (ENI 3251, Rochester, NY). The amplified signal (50 dB) was connected to the transducer through a diplexer (Ritec RDX-6, Warwick, RI). The echo signal was received by a pulser-receiver (Panametrics 5800, Waltham, MA), which was displayed on an oscilloscope (Lecroy 9354 TM, Chester Ridge, NY) for visual verification. The echo signal was recorded at a rate of 100 MHz by a 12-bit A/D (Strategic Test Digitizing Board UF3025, Cambridge, MA) for further processing by a PC. In addition to pulse-echo measurements, a Marconi hydrophone was used to obtain pressure measurements at the focus of the source. When in pulse-echo mode, the target used for imaging was a Plexiglas reflector located at the focus of the source.

To quantify the effects of nonlinear distortion on the compression, the pre-enhanced chirp was evaluated at four different output excitation voltage levels from the Tabor arbitrary waveform generator: 18 mV, 178 mV, 355 mV, and 710 mV. These voltages, which correspond the the peak amplitude in the pre-enhanced chirp, were amplified by 50 dB with a power amplifier. The pressure waves at the focus of the transducer were acquired with a calibrated hydrophone. The respective rarefactional pressure levels were estimated at: 69.7 kPa, 1.3 MPa, 2.7 MPa, and 4.0 MPa, respectively.

To predict the nonlinear distortion of the waveforms based on the pressure values, the discontinuity distance was calculated. The discontinuity distance is defined as the distance where significant nonlinear distortions of the waveform occur. The discontinuity distance, L_d, [20] is given by:

$$L_d = \frac{1}{\beta M k}. \tag{2.16}$$

B/A is equal to 5 for water at 20 °C. M [20] is the mach number which is defined as

$$M = \frac{U_0}{c_o} = \frac{P_0}{\rho c_o^2}, \tag{2.17}$$

where U_0 and P_0 are the particle velocity and pressure of the wave, and ρ and c_0 are the density and the speed of sound of the medium, i.e., water. Finally, k is the acoustic wave number. From (2.16), the pressure needed to produce significant nonlinear distortion of the waveform at a distance of 57 mm with a 5 MHz source proapagating in water is 517 kPa. Hence, at 517 kPa it is expected that significant effects of nonlinear distortion will start to occur.

2.1.3 Results

The pre-compression CRPRs for the aforementioned pressure levels were 1.14, 1.18, 1.16, and 1.23, respectively, suggesting higher waveform assymetry for the higher pressure values used. Similarly, the pre-compression SHFRs were -30.3 dB, -30.7 dB, -31.7 dB, and -24.9 dB, respectively, suggesting more energy was transferred to the higher harmonics with the increased pressure. The results from the first three pressure levels were not very different from each other. Therefore, these results indicated that nonlinear distortion effects were most visible for the 4.0 MPa case. Therefore, to simplify the discussion,

the 1.3 MPa and the 4.0 MPa cases were examined in further detail.

The PSD of REC compressed signals evaluated for three different γ parameters along with the CP reference are shown in Fig. 2.2(a). The three γ parameters were chosen in order to establish the effects of nonlinear distortion on the compression performance when matched filtering, inverse filtering and the operating state in between matched and inverse filtering were used. The SHFRs after compression for the 1.3 MPa and the 4.0 MPa cases as the Wiener filter approached a matched filter were -70 dB and -36 dB, respectively. These results suggest that a matched filter aids in the reduction of the nonlinear effects as the 1.3 MPa case resulted in an approximate decrease of 40 dB in the SHFR while the 4 MPa case saw an approximate reduction of 11 dB in the SHFR. However, a matched filter is known to introduce sidelobes as observed in Fig. 2.2(b). For example, the SMR results have short-range sidelobes at -25 dB and -20 dB and long-range sidelobes at -37 dB and -32 dB for the 1.3 MPa and 4 MPa REC cases, respectively. Another detriment of matched filtering is that the resolution suffers as the signal length increases due to the correlation. As a consequence, the MTF results shown in Fig. 2.2(c) indicate that the axial resolution for CP was 209 μm while the axial resolutions for the 1.3 MPa and 4 MPa cases were 300 μm and 298 μm. Overall, nonlinear distortion did not significantly affect the compression results when using a Wiener filter that approached a matched filter. However, for improving axial resolution and maintaining small sidelobes, the matched filter is not ideal.

On the other extreme, as the Wiener filter approached an inverse filter the opposite effects were encountered. In Fig. 2.2(a) it is clearly visible that the second harmonic and even the third harmonic (for the 4 MPa case) were stronger than the fundamental. As the Wiener filter approached an inverse filter the SHFR after compression for the 1.3 MPa and the 4.0 MPa cases were -0 dB. These results suggest that when nonlinear distortion is present, an inverse filter based on the impulse response of the system is detrimental as the 1.3 MPa case was characterized by an approximate increase of 17 dB in second harmonic amplitude while the 4 MPa case was characterized by an approximate increase of 25 dB in second harmonic amplitude. This increase in harmonic power led to larger sidelobe levels as shown in Fig. 2.2(b), which is especially noticeable when comparing the two pressure levels. For the 4 MPa case, the SMR short-range sidelobes

started at -10 dB while the long-range sidelobes were at -20 dB. For the 1.3 MPa case, the SMR short-range sidelobes started at -14 dB while the long-range sidelobes were at -30 dB. Furthermore, the MTF results revealed that the axial resolution for the 4 MPa case suffered because of the harmonic boost caused by the Wiener filter as it approached an inverse filter. Specifically, the evaluation of the MTF in Fig. 2.2(c) resulted in estimated axial resolution values for the 1.3 MPa and 4 MPa cases of 138 μm and 269 μm, respectively. Overall, nonlinear distortion negatively affected the compression, specifically by increasing the sidelobes and decreasing the axial resolution, when using a Wiener filter that approached an inverse filter.

A middle approach would be to use the gamma parameter to select a point between these the inverse and matched filter. Figure 2.2(a) indicates that for the case where the Wiener filter was between an inverse and matched filter response, the SHFR for the 1.3 MPa and the 4.0 MPa cases were -31 dB and -17 dB, respectively. For the 1.3 MPa case, the SMR was -30 dB for the short-range sidelobes and was -35 dB for the long-range sidelobes. For the 4 MPa case, the SMR was -32 dB for short-range sidelobes and was -34 dB for the long-range sidelobes. The values for the axial resolution determined by the MTF was 166 μm for the 1.3 MPa case and 151 μm for the 4 MPa case. In this approach, improvements in axial resolution were achieved compared to the matched filtering case. Furthermore, sidelobe levels were moderately improved when compared to both matched filtering and inverse filtering. These results along with the results for the matched filtering and inverse filtering case are summarized in Table 2.1

Pre-compression filtering

In the previous analysis, only changes in the gamma parameter were used to address the effects of nonlinear distortion. However, alternate schemes can be used to address nonlinear distortion effects in pulse compression. By applying a band-pass filter prior to compression, the harmonic content introduced by the nonlinear distortion could be suppressed and, as a consequence, improve the performance of the compression. To illustrate, a simple frequency domain Tukey window band-pass filter with a 50% taper ratio was applied to the pre-compressed echo data as shown in Fig. 2.3. The equation describing the Tukey window is as follows:

$$w(n) = \begin{cases} 1.0, & 0 \leq |n| \leq \alpha\frac{N}{2} \\ 1/2(1+\cos(\pi\frac{n-\alpha\frac{N}{2}}{2(1-\alpha)\frac{N}{2}})), & \alpha\frac{N}{2} \leq |n| \leq \frac{N}{2}. \end{cases} \tag{2.18}$$

The PSDs of REC compressed results evaluated for three different gamma parameters along with the CP reference are shown in Fig. 2.4(a). For all three Wiener filter scenarios, the SHFR values after compression for both the 1.3 MPa and the 4.0 MPa cases were well below -50 dB. The matched filter had SMR values of -19 dB for the short-range sidelobes and and -50 dB for the long-range sidelobes in the 1.3 MPa case. For the 4 MPa case, the SMR was -20 dB and -47 dB for the short- and long-range sidelobes, respectively.

In the case of an inverse filter, the sidelobe levels had an SMR of -22 dB for the short-range sidelobes and -45 dB for the long-range sidelobes for both 1.3 MPa and 4 MPa cases. These results suggest that the pre-compression filtering not only improved the compression results by removing the harmonics introduced by nonlinearities as shown in the 4 MPa case, but also aided in the reduction of sidelobe levels when the harmonic content was not as dominating as in the 1.3 MPa case.

MTF analysis resulted in estimates of the axial resolution for CP of 209 μm. The values of the axial resolution determined through the MTF using pre-compression filtering and then an inverse filter were 128 and 127 μm for the 1.3 MPa and 4 MPa cases, respectively. For the matched filter case, the axial resolution values were 148 and 137 μm for the 1.3 MPa and 4 MPa cases, respectively. Based on these results, the pre-compression filtering of the echo signals resulted in significant benefits in terms of reduction in sidelobe levels and improvements in axial resolution.

The effects of attenuation on nonlinear distortion when exciting with a pre-enhanced chirp

In soft tissues, ultrasonic attenuation typically increases with frequency. Consequently, the effects of nonlinear distortion are minimized in some fashion when imaging soft tissues due to the frequency-dependent attenuation. Specifically, the effects of nonlinear distortion are reduced because the higher frequency harmonic content is attenuated more rapidly than the fundamental. As a result, nonlinear distortion result in ex-

cess attenuation of the signal. Values highlighting the attenuation coefficients [27] of several human soft tissues are listed in Table 2.2. To evaluate the effects of frequency-dependent attenuation on the echoes that have been distorted by nonlinear propagation, the uncompressed echo data were modified by multiplying with a frequency-dependent attenuation term to simulate the effects of tissue attenuation synthetically on experimental data. Based on the range of attenuation coefficient values listed in Table 2.2 [28], attenuation coefficients of 0.0, 0.1, 0.3, 0.5, and 1.0 dB $\mathrm{MHz}^{-1}\mathrm{cm}^{-1}$ were evaluated.

The SHFR results for the aforementioned attenuation coefficient values are listed in Table 2.3. Furthermore, in Fig. 2.5 it can be observed from the PSD that the harmonic content was reduced as the attenuation coefficient increased. These results indicate that frequency-dependent attenuation aided the compression by mitigating some of the effects caused by nonlinear distortion of the signal. Even though attenuation appears to be beneficial, i.e., it ameliorated some of the effects brought on by nonlinear propagation, attenuation naturally reduced the bandwidth of the imaging system as shown in Fig. 2.5. Consequently, as the bandwidth was reduced the center frequency was shifted to lower frequency. The effects of the shift in center frequency due to attenuation on the REC technique will be discussed in Section 2.2.1.

2.1.4 Conclusion

The results of this study indicate that unless the harmonics are filtered prior to compression, the use of a Wiener filter operating as an inverse filter should be avoided in order to obtain adequate compression performance that minimizes sidelobe levels. The tradeoffs in moving away from an inverse filter are that the improvements in the axial resolution are minimized and sidelobes can be increased. When the echo signals were filtered prior to compression, significant improvements in both sidelobe levels and axial resolution were achieved by forcing the Wiener filter closer to an inverse filter state. Finally, attenuation could be a significant contributor in removing some of the distortion effects caused by nonlinear propagation, which would allow for improved compression performance.

2.2 Practical Limitations of the REC Technique

During the course of this study there were several limitations or hypothetical limitations encountered and characterized involving the REC technique. These limitations will be highlighted in the subsequent sections.

2.2.1 Center frequency shift and bandwidth reduction due to attenuation

The effects of frequency-dependent attenuation on coded signals have been investigated by several researchers [5, 10]. Therefore, the most significant effect that needed to be quantified in terms of the REC technique was the shift in center frequency caused by frequency-dependent attenuation and the amount of bandwidth reduction. It was hypothesized that the bandwidth using REC would have a larger shift in center frequency due to frequency-dependent attenuation as it contains a larger bandwidth compared to CP methods. The shift in center frequency can be modeled by describing the impulse response as a Gaussian function defined by

$$H(f) = Ae^{-\frac{(f-f_0)^2}{2\sigma^2}}, \tag{2.19}$$

where f is the frequency, A is the amplitude of the bandwidth at the center frequency, f_0, and σ is the standard deviation of the Gaussian distribution which would be representative of the bandwidth. The effects of frequency-dependent attenuation can be determined by multiplying the impulse response by the attenuation term assuming the attenuation coefficient is linear with frequency,

$$H(f,x) = Ae^{-\frac{(f-f_0)^2}{2\sigma^2}} \times e^{-4\alpha_0 fx}, \tag{2.20}$$

where α_0 is the attenuation coefficient (Np MHz^{-1} cm^{-1}) and x is the propagated distance into the media (in cm). After simplification the modified impulse response is given by

$$H(f,x) = Ae^{-\frac{(f^2-2ff_0+f_0^2-4\alpha_0 fx2\sigma^2)}{2\sigma^2}}. \tag{2.21}$$

To obtain the new center frequency, the maximum peak value was found by taking

the derivative of the expression in (2.21) and equating to zero,

$$\frac{d}{df}\left\{\frac{f^2 - 2ff_0 + f_0^2 - 4\alpha_0 f x 2\sigma^2}{2\sigma^2}\right\} = 0 \tag{2.22}$$

$$\frac{-f - 4\alpha_0 x\sigma^2 - f_0}{\sigma^2} = 0. \tag{2.23}$$

Solving for f, which is the new center frequency, the following is obtained:

$$f = f_0 - 4\alpha_0 x\sigma^2. \tag{2.24}$$

The expression in (2.24) indicates that by using the REC technique the center frequency will shift by a larger amount than CP because REC has a larger bandwidth. This phenomenon was further investigated by evaluating the effects of frequency-dependent attenuation in an experimental setting. The pre-filtered uncompressed echo data from the nonlinear propagation study was modified by multiplying with a frequency-dependent attenuation term to simulate the effects of tissue attenuation synthetically on experimental data. Based on the attenuation coefficient values listed in Table 2.2, attenuation coefficients of 0.0, 0.1, 0.3, 0.5, and 1.0 dB $\text{MHz}^{-1}\text{cm}^{-1}$ were evaluated. The experimental findings regarding center frequency shift for CP and REC (both a Wiener filter approaching an inverse filter (IF) and a Wiener filter approaching a matched filter (MF)) are summarized in Table 2.4. The bandwidth for CP was slightly less than REC-MF which was less than the bandwidth of REC-IF. The relative center frequency shift is shown in Fig. 2.6. Examination of Fig. 2.6 indicates that the smallest center frequency shift occurred with REC-MF. REC-MF obtained a small shift in center frequency because of the tremendous amount of bandwidth loss that resulted from the mismatch between the transmitted and received signals upon compression. Furthermore, as expected, the largest center frequency shift was obtained for REC-IF. This larger center frequency shift was a result of having the largest bandwidth.

Decreases in bandwidth due to attenuation were also observed (see Table 2.5 and Fig. 2.7). Interestingly, it was observed that the CP bandwidth increased for some attenuation values and then decreased for as the attenuation values got larger. This phenomenon occurred because the actual shape of the spectrum was asymmetrical. This phenomenon is shown in Fig. 2.8. For the pulse from the transducer, a sharper

falloff was observed in the bandwidth after the center frequency then before the center frequency. Therefore, when multiplying by a decaying exponential (attenuation) the bandwidth became larger for some small attenuation values. With REC, this increase in center frequency was not present as the pre-enhanced chirp boosted the frequencies in a manner such that the resulting bandwidth would be more symmetrical. Figure 2.9 shows regression analysis performed on the bandwidth data from Fig. 2.7. The points in the CP data that corresponded to increased bandwidth were not used in the regression analysis. For $\alpha = 0.5$, the -6 dB bandwidths for CP, REC-IF, and REC-MF were the same. Furthermore, for $\alpha < 0.5$ REC-IF provided the best results because the -6 dB bandwidth was larger, which means improved resolution. For $\alpha > 0.5$, CP provided the best results in terms of the -6 dB bandwidth. Of course, attenuation is depth-dependent and for this particular scenario the measurements were performed at the focus. Therefore, as the object is moved closer to the source, the performance for REC-IF and REC-MF is enhanced when compared to CP. As the object moves farther away from the source, CP may perform better in terms of bandwidth. The energy in the higher frequencies in REC is still greater than for CP due to the pre-enhanced chirp used to excite the source. Therefore, with appropriate depth-dependent filtering, the enhanced bandwidth of REC may be partially restored.

2.2.2 Transducer heating due to coded excitation

When sources are excited with a coded signal, it is possible that the source can heat leading to the possibility of burning tissue or skin if the probe is placed against the skin. The use of a pre-enhanced chirp was hypothesized to lead to even more heating tha a conventional linear chirp because it was expected that the excitation of the inefficient bands of the transducer would transfer more energy to heat. The idea is that preferentially exciting the inefficient bands with more energy would increase the surface temperature of the transducer, which could be potentially harmful to the patient being imaged.

The standard which characterizes the procedure for thermal measurements of sources (IEC 60601-2-37) indicates that surface temperature measurements should be conducted in air. However, measurements performed in air cause a reflection of the acoustic power

because of the impedance mismatch, which causes self-heating. Therefore, these measurements are considered to be a worst-case scenario. The temperature at which damage to the skin starts to occur is 56 °C [29].

To evaluate the effects of heating, measurements were performed with a single-element transducer (f/3) having a center frequency of 3 MHz and a -6 dB bandwidth of 33%. A noncontact infrared thermometer (Fluke 61, Everitt, WA) with a nominal manufacturer specified resolution of 0.2 °C and an accuracy of ± 2 °C was used. The measurements were performed in air with the thermometer at 152.4 mm away from the transducer. At this distance, the infrared thermometer provided an effective spot size of 19.05 mm, which was equivalent to the diameter of the transducer. The experiment consisted of exciting the transducer at different frequencies using a continuous sinusoidal excitation at different voltage levels. Specifically, frequencies ranging from 1 MHz to 6 MHz in increments of 1 MHz and excitation voltages of 50 mV, 100 mV, and 200 mV out of the Tabor AWG were used. These voltages were amplified by a 50 dB power amplifier (ENI 2300L, Rochester, New York). The results of the measurements are shown in Fig. 2.10. The results provide sufficient evidence that heating mostly occured at the fundamental frequency of the transducer and not at the band edges.

A pre-enhanced chirp with pulse repetition frequencies of 0.5 kHz, 1 kHz, and 2 kHz and a various excitation voltages (50 mV, 100 mV, and 200 mV) were tested. For the 0.5 kHz, and 1 kHz pulse repetition frequencies, the measured temperatures were near room temperature (¡ 1% variation). The thermal measurements obtained when exciting with a pre-enhanced chirp for the 200 mV case are shown in Fig. 2.10. The results of this test did not support the hypothesis that exciting with more energy in the inefficient bands of the transducer would lead to more heating over conventional linear chirps. Therefore, a new hypothesis was proposed that exciting the transducer with a pre-enhanced chirp resulted in more energy at the inefficient bands to be reflected back to the power amplifier. This new hypothesis will have to be further tested in the future by using a KLM model (developed by Krimholtz, Leedom, and Matthaei [30]) to characterize the pressure versus voltage characteristics of a piezoelectric transducer with a pre-enhanced chirp excitation to predict heating in the source. However, the pre-enhanced chirp was not observed to produce significant heating beyond a linear

chirp excitation.

2.2.3 Pressure-limited vs. voltage-limited chirps and their effect on eSNR

The main goal of the pre-enhanced chirp is to pump more energy into the band edges in order to obtain a wider and flatter system response in terms of bandwidth. Consequently, less energy is applied at the frequencies near the center frequency compared to the band edges. In this scenario, the pre-enhanced chirp is considered to be voltage-limited when the maximum voltage that can be applied to the transducer corresponds to the maximum value of the pre-enhanced chirp. If the pre-enhanced chirp was compared to a linear chirp and if the peak voltage of both signals applied to the transducer were the same, then a drop in the pressure output would be observed for excitation using the pre-enhanced chirp. A drop in pressure could be viewed as an advantage in that there is less potential for bioeffects or for nonlinear distortion. However, the disadvantage is that the eSNR would be smaller because less energy is contained in the pre-enhanced chirp compared to the linear chirp.

The drop in eSNR was evaluated by generating several pre-enhanced chirps in MATLAB for various sources with different fractional bandwidths. The results of this study are shown in Fig. 2.11. Examination of Fig. 2.11 suggests that the lower the original bandwidth of the source and the more axial resolution boost from REC, the smaller the eSNR. Therefore, in the voltage-limited case a tradeoff between the eSNR and the amount of axial resolution boost achievable with REC was observed. Most sources used in this REC study had a fractional bandwidth on the order of 75%. If the bandwith was doubled to 150%, according to Fig. 2.11, a 7 dB drop in eSNR would be obtained when compared to a linear chirp excitation. This lower eSNR comes from the fact that the amplitude of the pre-enhanced chirp at the center frequency is lower than the amplitude of the pre-enhanced chirp at the band edges. However, a linear chirp excitation would have a higher pressure output level, which could introduce bioeffects and increase the possiblity of nonlinear effects, and would not have the benefits of a larger bandwidth provided by REC.

Although a decrease in eSNR when exciting with a pre-enhanced chirp is dependent on source bandwidth and pre-enhanced chirp boost, a gain in eSNR is obtained after

compression by a factor related to the TBP. Therefore, consideration must be taken in the design of the code in terms of desired boost and code length (i.e., the larger the code the longer the dead zone in the image). For example, assume that an ultrasound system that was excited with a linear chirp (TBP = 40) resulted in an eSNR of 50 dB prior to compression when using a 10 MHz (75% bandwidth) transducer. If the source bandwidth was doubled to 150% using a pre-enhanced chirp with a TBP of 40, a reduction of 7 dB in eSNR would be obtained according to Fig. 2.11. Therefore, the resulting eSNR prior to compression would be 43 dB. In coded excitation schemes, the eSNR increases upon compression by a factor related to the TBP. Because the TBP was the same for the linear chirp and the pre-enhanced chirp, the eSNR was effectively smaller for REC when compared to the linear chirp, but higher than the precompressed output eSNR. Moreover, because the bandwidth in REC was larger and TBP for the linear chirp and the pre-enhanced chirp were the same, the time duration of the pre-enhanced chirp was smaller, resulting in a smaller dead zone. Finally, the increase in bandwidth resulted in an improved image because of the improved axial resolution.

The case when the maximum pressure output was the same for both codes was also studied. This case is contrasted with the previous case where the voltage input was the limiting value. In this scenario, the linear chirp was considered to be pressure-limited in that the input voltage to the transducer was not the limiting factor but the subsequent output pressure was the limiting factor. Because the intensity levels of diagnostic ultrasound are regulated by the FDA, as long as the transducer can handle high voltages, the only limitation may be the output pressure from the excitation levels, i.e., a transducer is more likely to be pressure-limited vs. voltage-limited in a clinical system. When a pressure-limited linear chirp was compared to a pre-enhanced chirp it was observed that the eSNR was slightly higher for REC because both chirps had equal energy at the center frequency but the pre-enhanced chirp boosted the energy in the band edges. Consequently, the transducer was being excited with more energy using pre-enhanced chirp. The drawback for the linear chirp was that, because the voltage was reduced, the eSNR was reduced. The results of this study lead to the conclusion that as long as the output intensity is within regulations, driving the transducers at the highest possible voltages yield the best performance. The driving voltages would

need to be optimized for individual transducers taking into account the durability of the transducers to higher voltages at the inefficient bands.

The main limitation in experimental scheme was that the power amplifiers used to provide the high voltage signals in to the transducers resulted in a voltage-limited scenario. These amplifiers had an input voltage limitation of $1V_{RMS}$. Therefore, if a pre-enhanced chirp had a peak value at $1V_{RMS}$, the voltage at the center frequency would be at best $0.5V_{RMS}$ if the bandwidth was only doubled. The implications were that the maximum linear chirp voltage would be $0.5V_{RMS}$, which means that the voltage of the linear chirp was being limited by the power amplifier. As a result, the linear chirp was voltage-limited in that improved results could be achieved with a voltage higher than $0.5V_{RMS}$.

Another item of importance is the maximum voltage that can be applied to transducers. Transducers have a voltage limit that is dictated by the Curie temperature of the crystal. If a transducer reaches the Curie temperature, then the transducer's crystal depolarizes which makes the transducer useless. Therefore, special care must be taken so that the voltage input does not exceed this limit at the band edges. For a transducer with a lithium niobate crystal the Curie temperature is 1415 ° C [31].

2.3 Conclusions

In the previous sections, the REC technique was characterized and practical limitations were discussed. The detrimental effects of nonlinear distortion on the compression of REC echoes were evaluated. Overall, amplification of the harmonics when the Wiener filter operated near inverse filter mode affected the compression performance the most compared to a matched filter. When the harmonics were amplified the sidelobe levels being produced were significantly higher than when no harmonics were present. Consequently, the compression performance was improved by pre-filtering the higher harmonics to reduce sidelobe levels.

The effects of frequency-dependent attenuation and pre-enhanced chirp construction limitations were examined. Specifically, the effects that attenuation had on REC because of its larger bandwidth were examined. Overall, attenuation caused a larger center frequency shift and resulted in a larger bandwidth loss with REC than with CP.

Furthermore, the pre-enhanced chirp was evaluated in terms of center frequency amplitude versus peak amplitude. It was concluded that pressure-limited case should results in the best performance of REC in terms of eSNR and compression. However, by exciting the transducers with higher voltages, the crystal stability could be compromised and the lifetime of the transducer could be reduced.

Finally, the possible heating of the source when excited with a pre-enhanced chirp was evaluated. The pre-enhanced chirp did not produce any significant source heating greater than would be achieved with a similar linear chirp. Therefore, it was concluded that heating of the source was not of greater concern using the REC method.

Overall, the engineering tradeoffs encountered during the practical limitation studies were: nonlinear distortion vs. sidelobes, bandwidth boost vs. eSNR, attenuation vs. center frequency shift, and attenuation vs. bandwidth.

2.4 Figures and Tables

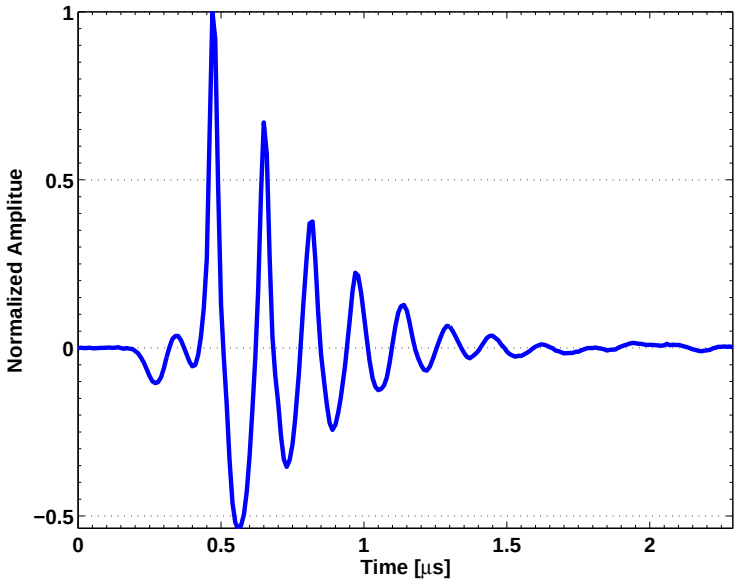

(a)

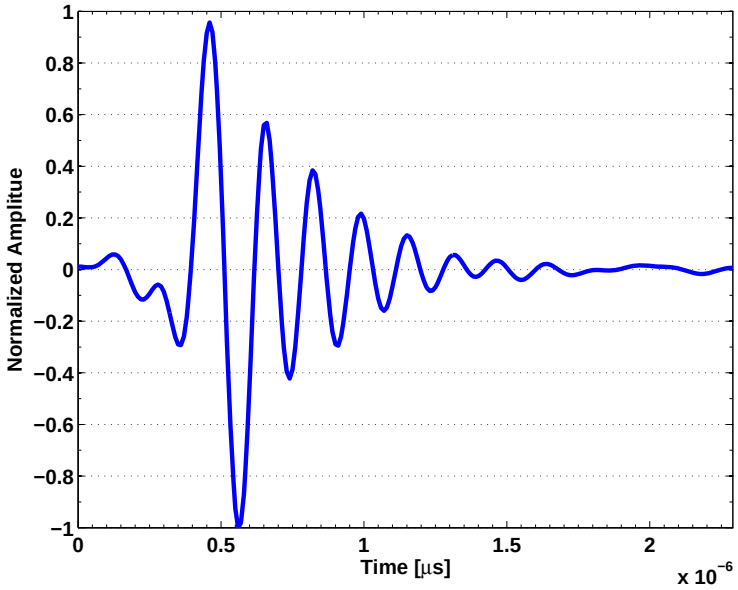

(b)

Figure 2.1: An ultrasonic waveform (a) exhibiting and (b) not exhibiting the effects of nonlinear distortion.

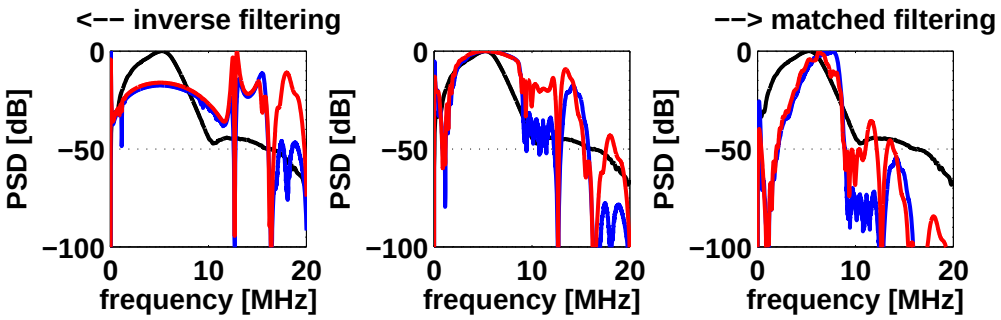

(a)

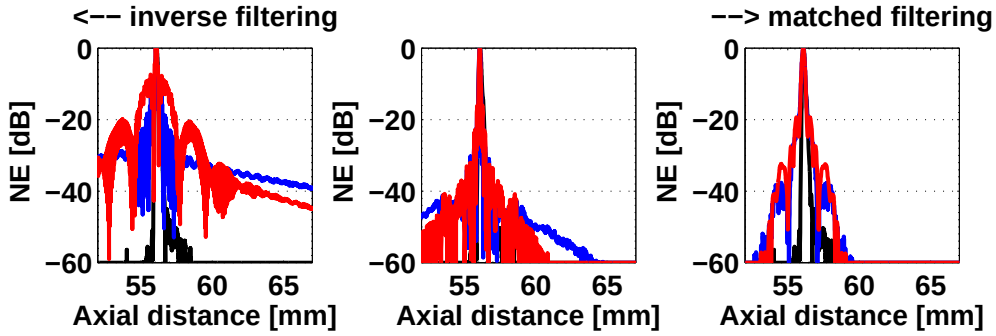

(b)

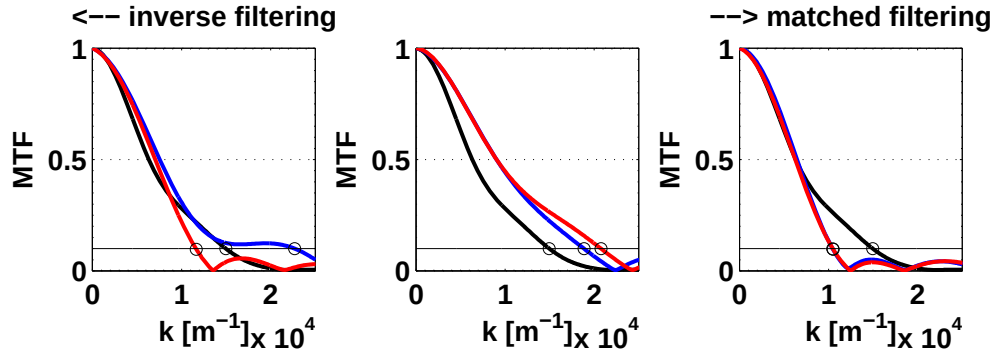

(c)

Figure 2.2: (a) PSD as a function of frequency, (b) normalized envelope as a function of axial distance, and (c) MTF as a function of wave number. From left to right shows the effects of changing the Wiener filter gamma parameter. CP is shown in black while REC values are shown in blue (1.3 MPa), and red (4 MPa). Note that the CP result is only shown as a reference and does not undergo distortion due to nonlinear propagation.

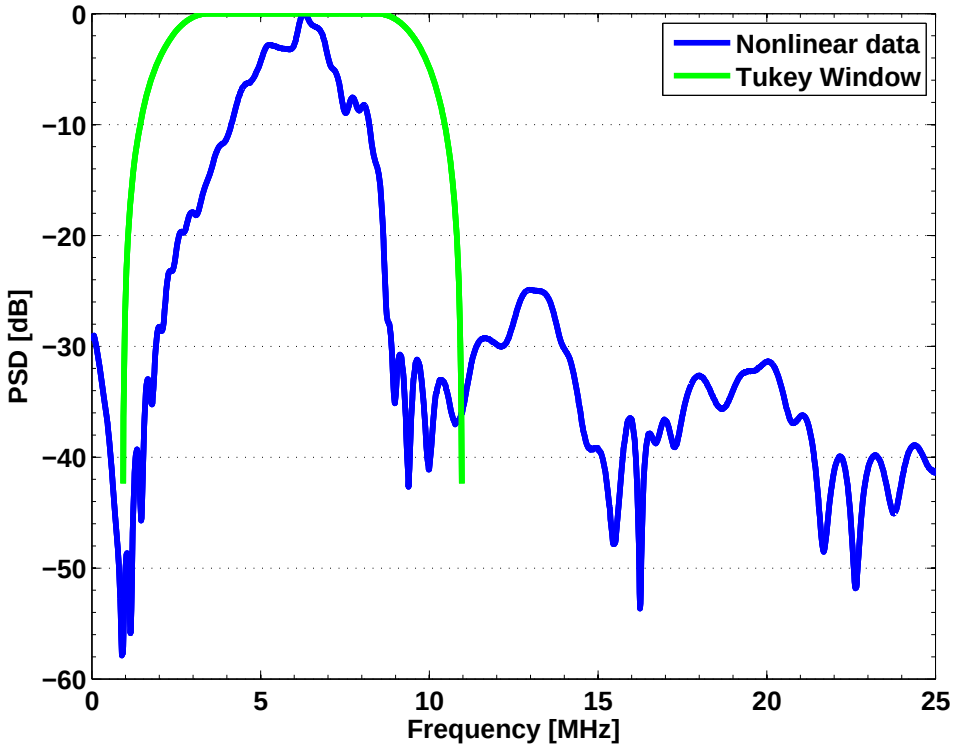

Figure 2.3: Application of a Tukey window on a pre-compressed echo to remove the higher harmonics caused by nonlinear propagation.

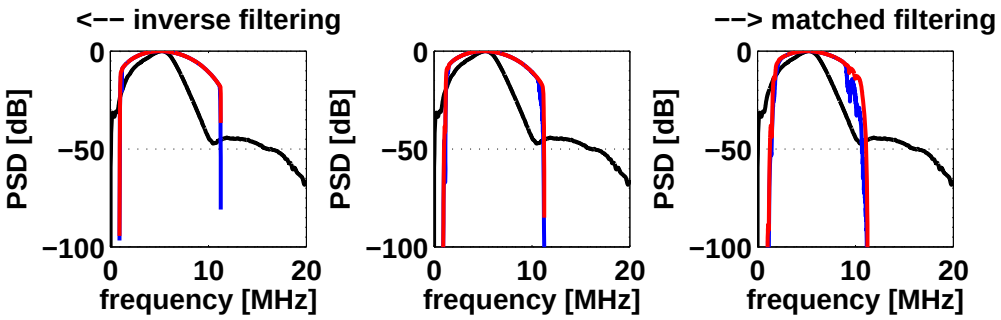

(a)

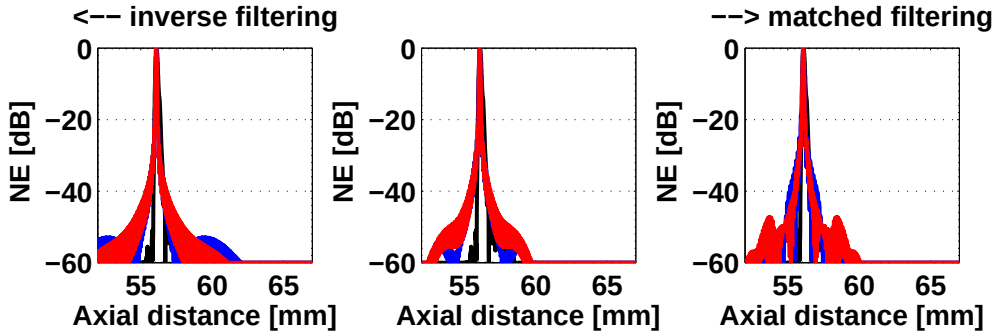

(b)

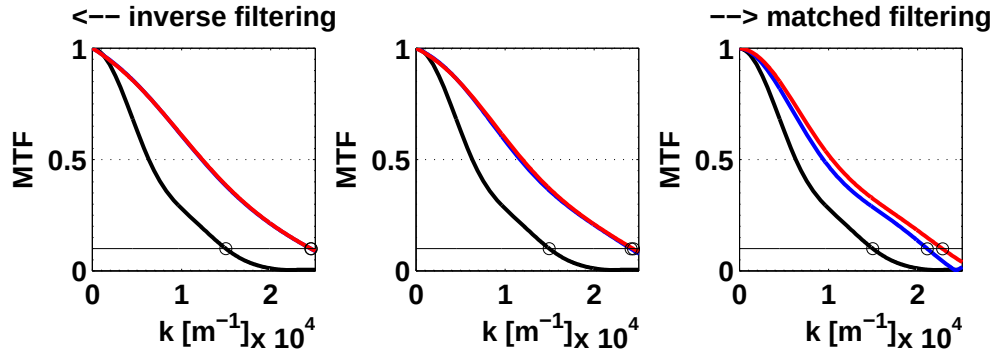

(c)

Figure 2.4: (a) PSD as a function of frequency, (b) normalized envelope as a function of axial distance, and (c) MTF as a function of wave number for the case that includes a post-filter to remove harmonics introduced due to distortion. From left to right shows the effects of changing the Wiener filter gamma parameter. CP is shown in black while REC values are shown in blue (1.3 MPa), and red (4 MPa). Note CP result is only shown as a reference and does not undergo distortion due to nonlinear propagation.

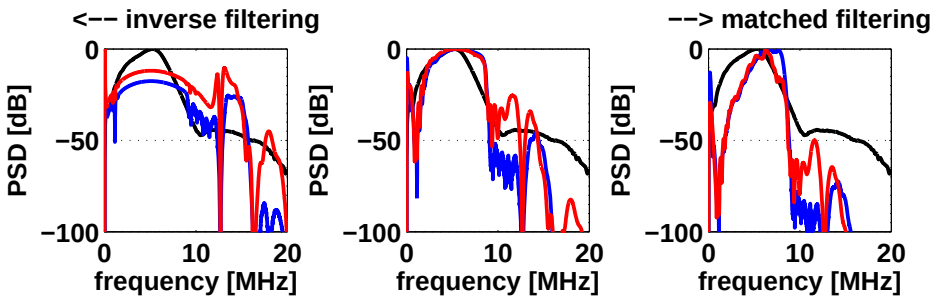

(a)

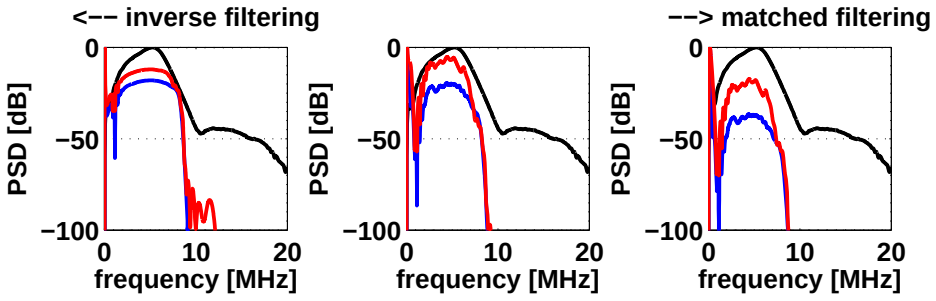

(b)

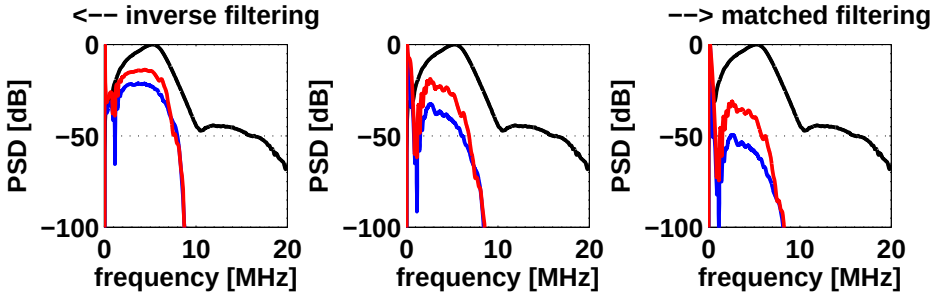

(c)

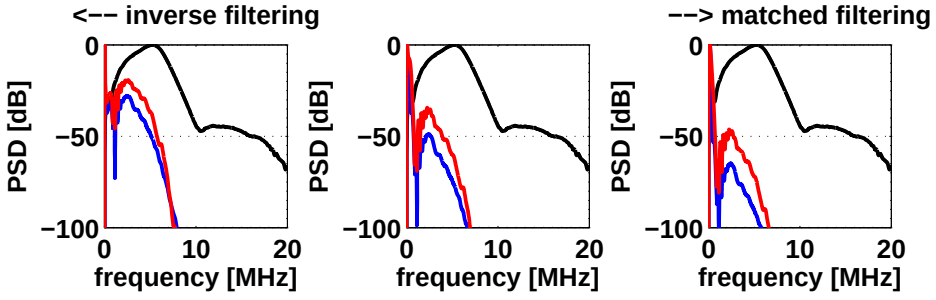

(d)

Figure 2.5: PSD as a function of frequency for different attenuation coefficients: (a) 0.1, (b) 0.5, (c) 0.7 and (d) 1.0 dB $\mathrm{MHz}^{-1}\mathrm{cm}^{-1}$.

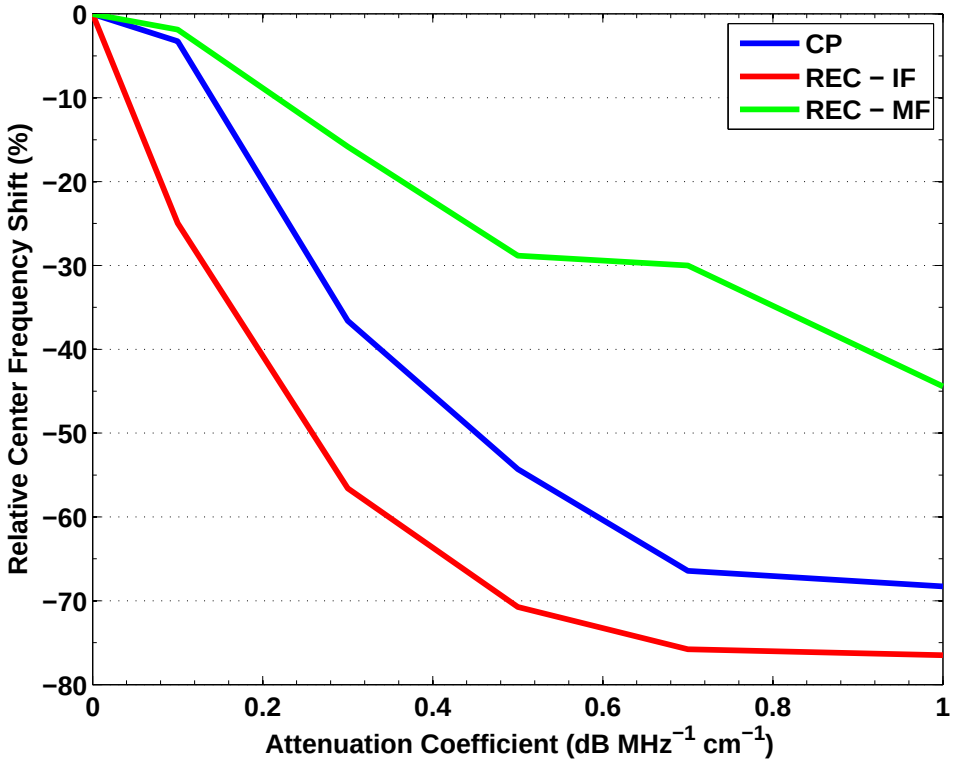

Figure 2.6: Relative frequency shift as a function of attenuation coefficient for CP and REC. REC was evaluated under two compression scenarios: a Wiener filter approaching an inverse filter (REC-IF) and a Wiener filter approaching a matched filter (REC-MF).

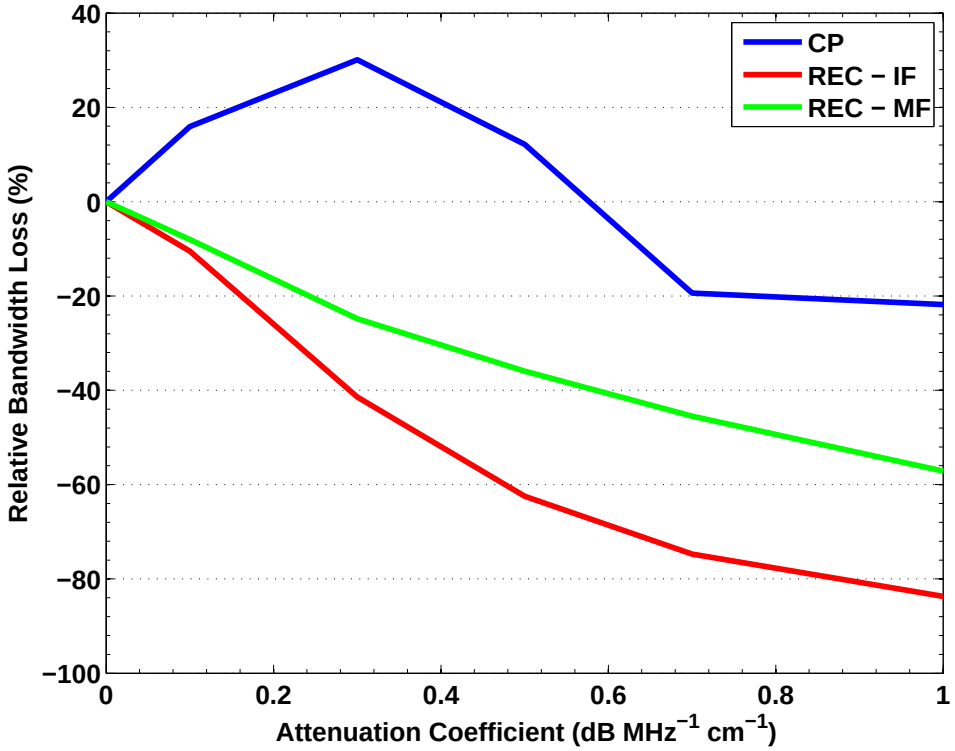

Figure 2.7: Relative bandwidth loss as a function of attenuation coefficient for CP and REC. REC was evaluated under two compression scenarios: a Wiener filter approaching an inverse filter (REC-IF) and a Wiener filter approaching a matched filter (REC-MF).

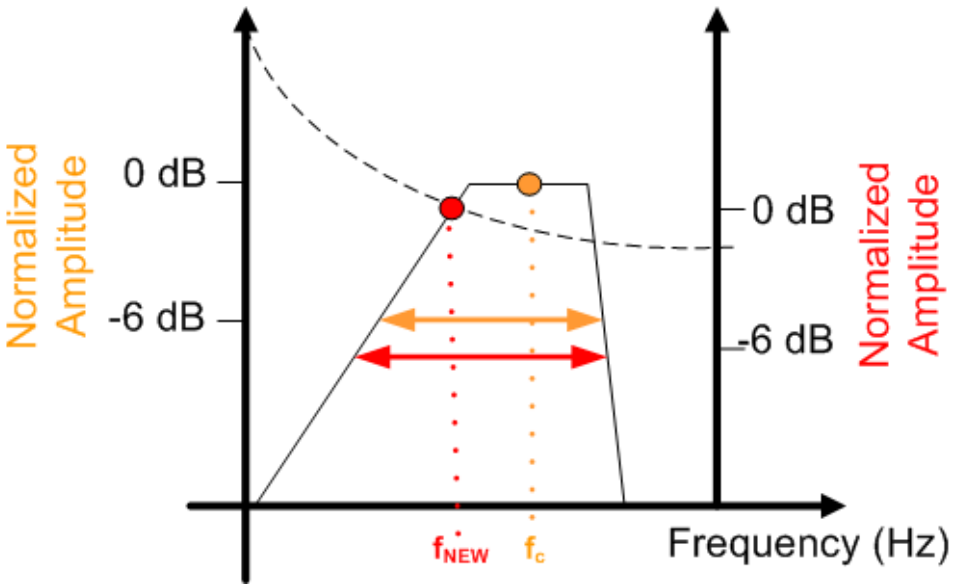

Figure 2.8: Example showing how a nonsymmetrical system function can become larger by an attenuating function. Items in orange show the original system function with the smaller bandwidth and the items in red show the system function with the larger bandwidth. Note that the ordinate is normalized amplitude and that in the scenario where the system function was attenuated the scale shifts due to normalization. f_c represents the center frequency while f_{NEW} represent the shift in center frequency.

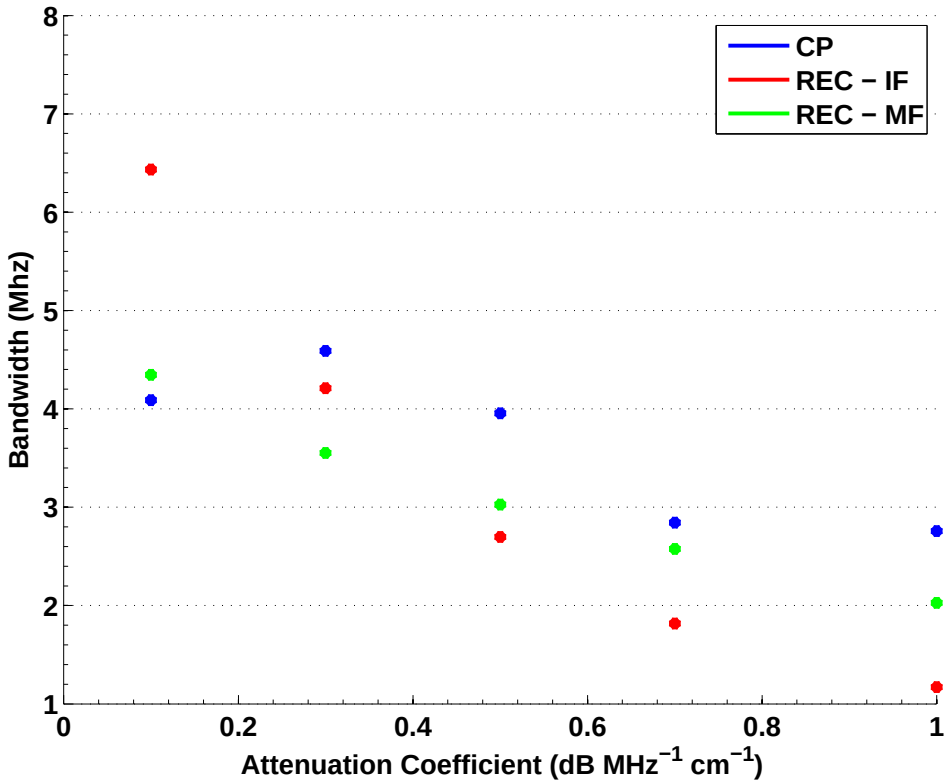

Figure 2.9: Bandwidth as a function of attenuation coefficient for CP and REC. REC was evaluated under two compression scenarios: a Wiener filter approaching an inverse filter (REC-IF) an a Wiener filter approaching a matched filter (REC-MF).

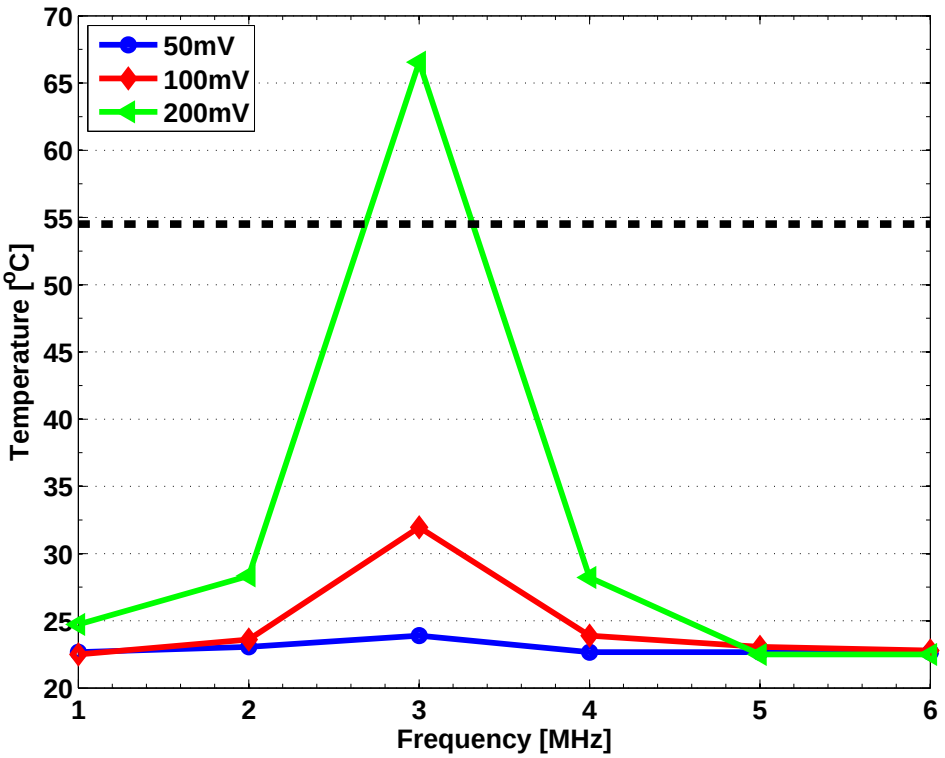

Figure 2.10: Thermal measurements of a 3 MHz transducer as a function of frequency for a continuous sinusoid excitation. Dashed line indicates the temperature at which skin starts to burn.

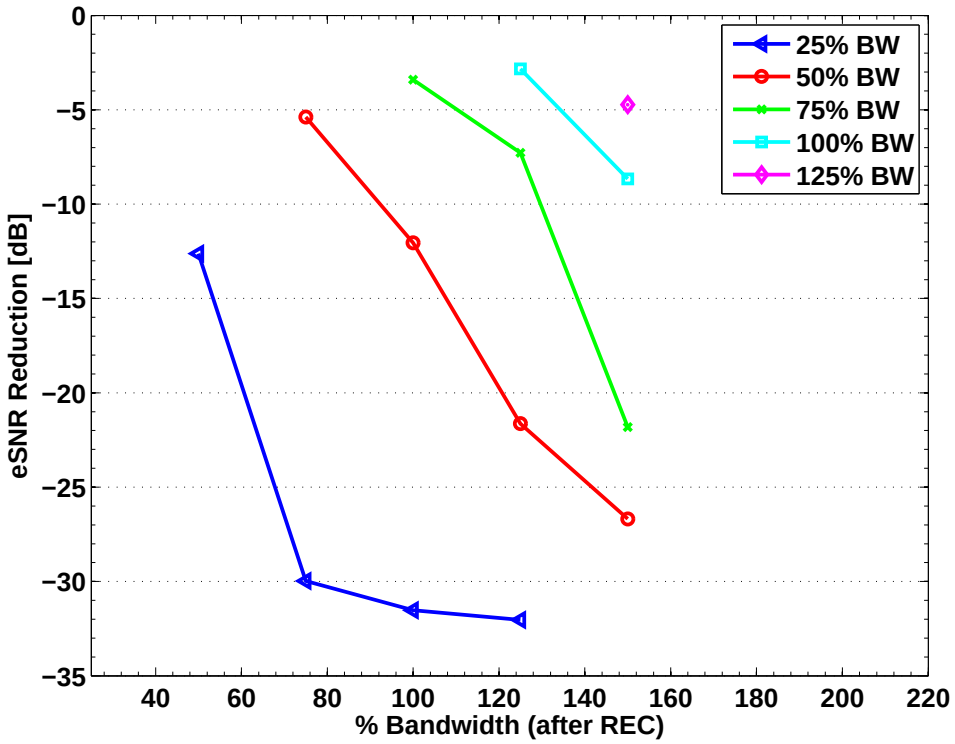

Figure 2.11: Reduction of eSNR as a function of the fractional bandwidth. The legend represents the original transducer bandwidth while the x-axis represents the bandwidth value achieved using REC. These results were obtained for a TBP of 40.

Table 2.1: A summary of SHFR, SMR (long-range (LR) and short-range (SR)), and MTF for the nonlinear effects study. The operating point of the Wiener filter was adjusted to obtain an inverse filter (IF), a matched filter (MF) and a middle approach between these extremes (MA).

Parameter	Pressure	IF	MA	MF
SHFR	1.3 MPa	0 dB	-31 dB	-70 dB
	4.0 MPa	0 dB	-17 dB	-36 dB
SMR-LR	1.3 MPa	-30 dB	-30 dB	-37 dB
	4.0 MPa	-20 dB	-34 dB	-32 dB
SMR-SR	1.3 MPa	-14 dB	-30 dB	-25 dB
	4.0 MPa	-10 dB	-32 dB	-20 dB
MTF	1.3 MPa	138 μm	166 μm	300 μm
	4.0 MPa	269 μm	151 μm	298 μm

Table 2.2: Attenuation coefficients of some common human soft tissues.

Tissue Type	α_{dB} (dB MHz^{-1}cm^{-1})
Blood	0.20
Breast	0.75
Fat	0.48
Kidney	1.0
Liver	0.5
Muscle	1.09
Skin	0.35

Table 2.3: SHFR results when applying attenuation to the distorted signals due to nonlinear propagation at the focal depth (55 mm) of a 5 MHz (f/3) source.

Attenuation Coefficient	Inverse Filter		Matched Filter	
	1.3 MPa	4 MPa	1.3 MPa	4 MPa
(dB $MHz^{-1}cm^{-1}$)	(unitless)	(unitless)	(unitless)	(unitless)
0.0	-0	-0	-70	-36
0.1	-0	-8	-72	-50
0.3	-26	-50	$\leq$-100	-75
0.5	$\leq$-100	-71	$\leq$-100	$\leq$-100
1.0	$\leq$-100	$\leq$-100	$\leq$-100	$\leq$-100

Table 2.4: Center frequency shift after synthetically adding attenuation to the pre-compressed echoes. CP center frequency shift shown as reference.

Attenuation Coefficient	CP	REC	
		Inverse Filter	Matched Filter
(dB $MHz^{-1}cm^{-1}$)	(MHz)	(MHz)	(MHz)
0.0	0.00	0.00	0.00
0.1	-0.17	-1.27	-0.10
0.3	-1.91	-2.88	-0.83
0.5	-2.84	-3.60	-1.51
0.7	-3.47	-3.85	-1.58
1.0	-3.57	-3.89	-2.33

Table 2.5: Bandwidth after synthetically adding attenuation to the pre-compressed echoes. CP bandwidths shown as reference.

Attenuation Coefficient (dB $MHz^{-1}cm^{-1}$)	CP (MHz)	REC	
		Inverse Filter (MHz)	Matched Filter (MHz)
0.0	3.52	7.19	4.72
0.1	4.09	6.43	4.34
0.3	4.59	4.21	3.55
0.5	3.96	2.70	3.02
0.7	2.84	1.81	2.57
1.0	2.75	1.17	2.02

CHAPTER 3

APPLICATIONS FOR THE REC TECHNIQUE

In this chapter, potential applications where REC could be beneficial are explored. Specifically, three applications were evaluated where the improved axial resolution and increased bandwidth available from REC could be beneficial. First, REC was used to enhance the contrast of B-mode images using frequency compounding. Second, REC was used to improve contrast and spatial resolution of quantitative ultrasound (QUS) images.

3.1 Speckle Reduction and Contrast Resolution Enhancement of B-mode Images using REC

3.1.1 Introduction

Speckle, the granular structure in ultrasonic images, reduces the ability to detect low-contrast targets. Speckle is formed by subresolution scatterers that cause constructive and destructive interference of backscattered ultrasonic signals within the resolution cell volume of an ultrasonic source [32]. Furthermore, speckle is considered to be a deterministic process because when an object is imaged under the same operating conditions no changes in the speckle pattern occur. For these reasons, speckle is not reduced by signal averaging over time. Therefore, considerable effort has been spent over the last few decades in developing techniques to reduce speckle in ultrasonic images.

Why speckle reduction?

In imaging, small structures or an object can be identified if the contrast between the target and the surrounding area are different [33]. Figure 3.1 shows a 1-D example of the effects that speckle can have on the detectability of low contrast targets. In ultrasonic imaging, the difference in contrast between different soft tissues can be very small. Therefore, with the use of speckle reduction techniques, image contrast can be improved by removing the interference pattern created by speckle. This intereference pattern created by speckle is also known as speckle noise and reduction of speckle noise can enhance the detectability of structures having low contrast with the background [34]. Consequently, speckle reduction techniques have been used clinically and applied to commercial systems in order to improve the detection of small structures and lesions [35].

Speckle reduction techniques

Speckle reduction techniques can be classified into two categories: post-processing techniques and compounding methods. Examples of post-processing techniques are adaptive filtering (linear and nonlinear) [36–40], deconvolution [41, 42], and wavelet despeckling [43, 44]. The compounding speckle reduction methods include spatial and frequency compounding. These schemes rely on making separate images that have uncorrelated or partially correlated speckle patterns. The separate images are then averaged to reduce the speckle while maintaining the mean intensity of the image but at the expense of spatial resolution. Originally for spatial compounding, the source aperture was translated laterally or at different angles to make images from different orientations [45, 46]. The main drawbacks of these techniques are loss in lateral resolution, and image misalignment due to motion which causes image artifacts. In addition, the need for multiple images would mean a decrease in the frame rate. Recently, manufacturers have employed receive-aperture-only spatial compounding which is not subject to frame rate losses or motion-based image registration errors because all processing is performed after the data is collected. Other advances in spatial-compounding [47, 48] use electronic beam-steering to obtain images at different angles to overcome some of these tradeoffs by using advanced image registration.

Frequency compounding

Another method, known as frequency compounding (FC), can be applied on transmit mode by using multiple sources at different frequencies or on receive mode as a post-processing speckle reduction technique by dividing the spectrum of the radio-frequency (RF) echoes into subbands to make separate and partially uncorrelated images [49–55]. The latter instance is also known as frequency diversity [50, 55], or split spectrum processing [53]. Compounding is performed by averaging the images generated from each subband. As a result of compounding, a reduction in the speckle variance is obtained while maintaining the mean intensity of the signal. As the width of the subband becomes smaller, the effective bandwidth used to create individual images decreases, which translates into a decrease in axial resolution. Therefore, the main disadvantage introduced by using frequency compounding is the inherent tradeoff between axial and contrast resolution. In fact, if a lesion is too small, loss of axial resolution may actually decrease contrast because signals from the lesion and background can smear together. Consequently, if the axial resolution and the bandwidth of an ultrasonic imaging system could be increased, these tradeoffs between axial and contrast resolution could be extended.

The first researchers that applied FC to medical ultrasound were Abbott and Thurstone [49]. In the study, they compared laser speckle to ultrasound speckle and suggested several techniques to generate independent speckle patterns including FC. Magnin et al. [51] observed that decorrelation of speckle patterns is dependent upon the excitation bandwidth and obtained increases in speckle signal-to-noise ratio (sSNR) of 26% in B-mode images using a phased array system. The sSNR is defined as the ratio of the mean to the standard deviation of the echo amplitude [32]. Melton et al. [52] developed a model to predict the amount of speckle reduction in A-mode scans based upon correlation coefficients. Trahey et al. [46] discussed a method for optimal speckle reduction based on the number of images that should be acquired within the available system bandwidth. Gehlbach et al. [50] studied frequency diversity using digital filtering techniques to determine a method to maximize sSNR and increase the ability to detect low-contrast targets. In addition, it was observed that a 10 to 15 percent increase in sSNR could be achieved by increasing the number of filters and filter overlap. Stetson et al. [56] used frequency diversity techniques with the combination of gray level mapping

to improve the contrast-to-noise ratio (CNR) of low-contrast targets. CNR assess image quality and describe the ability to perceive a target from the background region [34]. Overall, these studies suggested that FC is an effective tool for image contrast improvement. Therefore, by combining FC techniques with REC, it is hypothesized that further reductions in the variance caused by speckle could be obtained because of the larger bandwidth available.

3.1.2 Methods and procedure

The objective of using FC was to reduce the speckle noise and enhance the contrast in ultrasonic B-mode images. In the FC study, the received wideband RF spectrum was partitioned into N subbands by using Gaussian band-pass filters of smaller bandwidth than the original spectrum. These narrowband subbands were used to create separate images that had partially uncorrelated speckle patterns,i.e., up to 60% decorrelation [51]. Typically, improvements in sSNR and CNR are proportional to $\sqrt{N}$; however, because these separate images were partially correlated, the improvements should be proportional to a factor less than the square root of the sum of uncorrelated images [32]. These separate images were first normalized and then added together to reduce the speckle by reducing the image intensity variance. However, the axial resolution deteriorates because the compounded image was generated by averaging smaller subband images. The block diagram in Fig. 3.2 depicts the operation of FC for a system of N = 3. An example of FC for a system with N = 4 is shown in Fig. 3.3.

By using REC, a larger bandwidth was available, which allowed larger subbands to be used, or more importantly, an increase in the number of subbands that could be applied for a particular desired axial resolution. For this application the goal was to combine the REC technique with FC, which will be described as REC-FC, to extend the tradeoff of loss in axial resolution versus improvements in contrast. Accordingly, a parameter of interest was the bandwidth of these subbands. Therefore, in simulations and experiments, four cases were evaluated in terms of the subband width when applying FC to the REC technique. The first case consisted of using subbands that were the same width of the true impulse response bandwidth, designated as full width. The resolution of the compounded image in the full width case would be the same as that using CP

but the contrast resolution should improve due to FC. Other cases consisted of using subbands smaller than the full width, specifically, half-, third- and fourth-width of the original impulse response bandwidth. A plot showcasing the sizes of the subbands for all cases in addition to the original bandwidths of CP and REC is shown in Fig. 3.4. The cases of genuine interest are full and half width as the intention of this work was to improve the contrast without suffering a large amount of axial resolution loss. However, for study completion the later two cases, third- and fourth-width, were also evaluated. Other filter bank parameters that were considered and evaluated through simulations and experiments when applying FC to the RF spectrum were subband center frequency separation, first subband center frequency starting point, and the number of subbands. The values of these parameters were chosen so that they optimized the image quality metrics, which are defined in the following section.

Image quality metrics

To evaluate the performance of the REC-FC technique compared to CP and CP-FC the following image quality metrics were used:

1. Contrast-to-noise ratio (CNR): CNR [34], also known as contrast-to-speckle ratio, is a common quantitative measure that can assess image quality and describe the ability to perceive a target from the background region. CNR is defined as

$$CNR = \left| \frac{\mu_B - \mu_T}{\sqrt{\sigma_B + \sigma_T}} \right|, \tag{3.1}$$

   where μ_B and μ_T are the mean intensity of the background and the target lesion, and σ_B^2 and σ_T^2 are the variance of the background and target, respectively. To avoid possible errors in the calculations due to attenuation, the evaluated regions of interest in the background and the target lesion were the same size and were located at the same depth.

2. Speckle signal-to-noise ratio (sSNR): sSNR [57] is a measure of the fluctuations in the speckle of a particular region of interest and is defined as

$$sSNR = \frac{\mu}{\sigma}, \tag{3.2}$$

where μ and σ are the mean and the standard deviation of the amplitude in the region of interest, respectively. Specifically, sSNR was evaluated for same-sized regions (900 x 20 samples, axially and laterally) in the target lesion and the background that were located at the same depth. For Rayleigh statistics, sSNR approaches 1.91 [32].

3. Histogram pixel intensity (HPI): HPI is the mean of the frequency distribution of grayscale pixel intensities and is described by

$$HPI = E\{B\}. \tag{3.3}$$

B is the histogram being evaluated and is described by

$$B(i) = c_i, \tag{3.4}$$

where c_i represents the number of pixels in the image within a particular intensity level, i, which is an integer between 0 and 255 that represents the grayscale levels used in B-mode images. Histograms were made for same-sized regions (900 x 20 samples, axially and laterally) for the target lesion and the background and located at the same depth. Ideally, for superior target detectability, there is no overlap present between the target histogram and the background histogram. Therefore, histogram overlap (HO), which is the percentage of overlapping pixels between these two regions, was also considered.

4. Lesion signal-to-noise ratio (lSNR): lSNR [57] is a ratio of contrast-detail and resolution, and therefore considers both contrast and spatial resolution for target detection. Contrast detail is an analytical measurement of image quality that quantifies the ability of the ideal observer/imaging device to detect an isolated object of minimum size at a fixed contrast, at a given level of observer confidence and for a given noise level [58]. The metric relates to the ideal observer in that it yields the dependence of lesion contrast on lesion diameter at the observer's threshold for detection [57]. The lSNR relation is defined as:

$$lSNR = \frac{C \cdot d \cdot \sqrt{N}}{\sqrt{S_{cx} \cdot S_{cz}}}, \tag{3.5}$$

where d is the diameter of the target lesion, N is the number of uncorrelated images generated with FC (N = 1 otherwise), S_{cx} and S_{cz} are the average resolution cell size in the lateral and axial direction, respectively, and C [58] is the contrast of the target and is defined by

$$C = \frac{\psi_1 - \psi_2}{\sqrt{\psi_1 + \psi_2}}, \tag{3.6}$$

where ψ_1 and ψ_2 are the mean-square scattering strength (backscatter intensity) of the background and the target lesion, respectively. The average cell size is obtained using the normalized autocovariance function [59]. It is noteworthy to state that although the correlation function can be evaluated for the compounded image, the results generated are inaccurate because the uncorrelated speckle patterns are averaged, which would morph the speckle size. As a result, the average correlation function was evaluated by using one of the subband images generated. lSNR is a valuable metric in that it allows quantification of the tradeoffs between axial resolution, lesion size, and contrast between different imaging systems.

Computer simulations

Computer simulations were carried out in MATLAB (Mathworks, Natick, MA) to characterize the performance of the REC-FC technique. The simulations used a received pulse-echo pressure field model [60] described as

$$g'(x, y, t) = h_1(t) * f(x, y) * h_{pe}(y, t), \tag{3.7}$$

where x represents the axial spatial coordinate, y represents the lateral spatial coordinate, $h_1(t)$ is the pulse-echo impulse response of the transducer, $f(x, y)$ is the scattering function, and $h_{pe}(y, t)$ is the modified pulse-echo spatial impulse response that takes into consideration the geometry of the transducer and the spatial extent of the scattered field (beam diffraction). The pulse-echo impulse response, $h_1(t)$, for CP was generated by gating a sinusoid of four cycles with a Hanning window

$$w(n) = \begin{cases} 0.5 \cdot (1 - cos(\frac{2\pi n}{L_H - 1})), & 0 \leq n \leq L_H - 1 \\ 0, & \text{otherwise,} \end{cases} \tag{3.8}$$

where n is an integer and L_H is the number of samples in the window. The window and sinusoid parameters where chosen such that they matched the transducer used in experiments. As a result, the generated pulse-echo impulse response was located at the focus of a 2.25 MHz single-element transducer (f/2.66) with a fractional bandwidth of 50% at -3 dB, which would correspond to a window length of N = 128. For REC, the desired impulse response function, $h_2(t)$, was constructed to have double the fractional bandwidth, or 100% at -3 dB, compared to the CP method. Therefore, a Hanning window of half the length, N = 64, was used to construct the REC impulse response. The spatial response for a circular focused piston source can be approximated as a circular Gaussian beam [61] which is defined as

$$h_{pe}(y,t) = \delta(t - \frac{2R_d}{c}) e^{\frac{-y^2}{\sigma_y^2}}, \tag{3.9}$$

where R_d is the distance from the source to target in space, c is the speed of sound of the medium and σ_y, which was set to be equal to 1.28 mm, is the nominal lateral beamwidth of the source at -6 dB, which is the full width at half maximum.

The object being imaged was a simulated phantom that was 20 mm in length, 30 mm in width and 1.92 mm in height. The received RF backscatter data were sampled at a rate of 100 MHz. The transducer was translated laterally across the surface of the phantom in increments of 0.1 mm. A cylindrical target with a radius of 7.5 mm was located at the center of the phantom. To generate a hyperechoic target with a contrast of approximately +6 dB, the amplitude of the scattering strength from scatterers in the target lesion region was twice the amplitude of the scattering strength from scatterers in the background. To achieve fully developed speckle, the phantom contained an average of 20 point scatterers per resolution cell volume. In this dissertation, a resolution cell volume for a circular transducer is defined as a pulse length times the area of a cylinder, where the cylinder width is the lateral beamwidth. The scatterers were uniformly distributed throughout the phantom and spatially at random.

A total of 50 phantoms were simulated and evaluated with the image quality metrics discussed in Section 3.1.2. Attenuation and noise were not modeled in the simulations in order to examine the relationship of FC to the speckle reduction only. In simulations, no optimization of the γ parameter in the Wiener filter (Eq. (1.2)) was used. However,

in this study the γ parameter (Eq. (1.2)) was set to unity and then slightly adjusted until it forced the Wiener filter towards an inverse filter in order to increase the axial resolution.

Experimental setup

Experiments were performed to validate the simulations. A single-element, weakly focused (f/2.66) transducer (Panametrics, Waltham, MA) with a nominal center frequency of 2.25 MHz and a 50% (at -3 dB) fractional bandwidth (measured) was used to image a phantom by translating the transducer laterally across the phantom. There were two different experimental setups utilized: one for CP methods and another one for REC experiments. These setups would contain different noise levels due to the use of different excitation systems. Therefore, to avoid errors in the comparisons, the noise levels were normalized to an eSNR of 28 dB. Normalization of eSNR was accomplished by adding zero-mean Gaussian white noise to the CP RF echo waveform. The two experimental setups are described as follows:

1. Conventional pulsing experimental setup: The transducer was excited by a pulser-receiver (Panametrics 5800, Waltham, MA) and the receive waveform was displayed on an oscilloscope (Lecroy 9354 TM, Chester Ridge, NY) for visual verification. The echo signal was recorded at a rate of 100 MHz by a 12-bit A/D (Strategic Test Digitizing Board UF3025, Cambridge, MA) for further processing by a PC. A diagram of the experimental setup for CP is shown in Fig. 3.5(a).

2. REC experimental setup: The pre-enhanced chirp was generated in MATLAB (The Mathworks Inc., Natick, MA) and downloaded to an arbitrary waveform generator (Tabor Electronics W1281A, Tel Hanan, Israel). The excitation signal was sampled at a rate of 100 MHz and amplified by an RF power amplifier (ENI 3251, Rochester, NY). The amplified signal (50 dB) was connected to the transducer through a diplexer (Ritec RDX-6, Warwick, RI). The echo signal was received by a pulser-receiver (Panametrics 5800, Waltham, MA), which was displayed on an oscilloscope (Lecroy 9354 TM, Chester Ridge, NY) for visual verification. The echo signal was recorded at a rate of 100 MHz by a 12-bit A/D (Strategic Test

Digitizing Board UF3025, Cambridge, MA) for further processing by a PC.

A tissue-mimicking phantom (ATS Laboratories Model 539, Bridgeport, CT) and a hydrogel cone phantom were used to assess the performance of REC-FC with the image quality metrics described in Section 3.1.2. The material from the ATS tissue-mimicking phantom consisted of urethane rubber with a speed of sound of 1450 m/s $\pm$ 1.0% at 23 °C and an attenuation coefficient of 0.5 dB MHz^{-1} cm^{-1} $\pm$ 5.0%. A 15 mm diameter echogenic grayscale target structure with a constrast of +6 dB located at a depth of 4 cm into the phantom was imaged and the four FC cases were applied. Therefore, the goal of imaging with the ATS phantom was to evaluate and quantify the contrast improvements versus changes in spatial resolution for lesions of the same size but with different contrasts.

A hydrogel cone phantom was designed and fabricated at the Ultrasonic Imaging Laboratory at the Beckman Institute at the University of Illinois at Urbana-Champaign. The phantom contained a cone inclusion with a 15 mm diameter at the top. By imaging cross-sectional planes of the cone at different heights of the cone, lesions of different sizes could be imaged and evaluated. The materials (and relative amounts by weight) for the cone inclusion were type-A gelatin (Fisher Scientific, Pittsburgh, PA) (5.5%), n-propanol (9.0%), distilled and deionized water (83.4%), formaldehyde (0.1%), and powdered graphite (2.0%). The materials (and relative amounts by weight) for the surrounding medium around the cone were type-A gelatin (5.5%), n-propanol (9.0%), distilled and deionized water (84.8%), formaldehyde (0.1%), and powdered graphite (0.5%). The powdered graphite scatterers were positioned at random locations throughout the phantom by rotating the phantom before the gel congealed. In addition, the concentration difference of the powdered graphite between the cone lesion and the background provided cone-to-background contrast of +6 dB. The speed of sound and the attenuation coefficient slope of the phantom were measured to be approximately equal to 1540 m/s and 0.49 dB MHz^{-1} cm^{-1}, respectively, when using a 2.25 MHz source. The goal of imaging with the hydrogel cone phantom was to evaluate and quantify the contrast improvements by varying the size of the lesion while maintaining the same lesion-to-background contrast.

All measurements of phantoms were conducted at room temperature (approx. 23 °C) in a tank of degassed water. Furthermore, in experimental measurements, no optimization of the γ parameter in the Wiener filter (1.2) was used. Moreover, the same technique to determine the γ as described in Section 3.1.2 was used for the experimental measurements.

3.1.3 Results

Computer simulations

Descriptions of the filter banks designed for the computer simulations are given in Table 3.1. The resulting axial and lateral resolutions are given in Table 3.2. The axial resolution should deteriorate as the subband width decreases. Moreover, the values obtained for CNR and sSNR for all four cases (full-, half-, third-, and fourth-width) in addition to the reference scans (CP and REC with no compounding) are listed in Table 3.3. The values for HPI, HO, and lSNR are summarized in Table 3.4. From Table 3.3 it can be observed that both CNR and sSNR improved as the number of subbands increased and the subband width became smaller. These improvements in terms of CNR, sSNR_B, and sSNR_T are also illustrated in Fig. 3.6(a,b,c). These graphs indicate that as the number of subbands increased the contrast as quantified by these metrics also increased.

The B-mode images representing the results are displayed in Fig. 3.7. Examination of the reference scans in Figs. 3.7(a) reveals that by using the REC technique without any compounding the speckle size was finer than when compared to CP. The smaller speckle size (i.e., better spatial resolution) resulted in the object boundaries being more well-defined because there was more detail compared to CP images. The spatial resolution boost was then traded away to improve contrast resolution by applying FC with subbands that had the same bandwidth as CP (full width) as shown in Fig. 3.7(b). For the full-width case, the CNR, sSNR_B, and sSNR_T improved by 71%, 53%, and 51% over CP. Essentially, a gain of CNR and sSNR was achieved while maintaining the same spatial resolution that would be obtained by using CP methods. Through examination of Fig. 3.6(d), the lSNR values were higher for REC than for CP. Therefore, the increasing

lSNR suggests that the target detectability was increased with REC-FC compared to CP. The lSNR for REC without compounding was 15% better than that for CP without compounding. This implies that the same lSNR value would be obtained for both CP and REC, if a target of approximately 13 mm in diameter was imaged with REC compared to 15 mm imaged using CP. In other words, according to the lSNR metric,a smaller lesion would be more detectable with REC than with CP because of the spatial resolution boost.

In addition to improvements in contrast, the boundaries of the target were more defined with REC-FC when compared to CP. This edge enhancement was due to the resolution enhancement in the REC reference image which led to increased detail as shown in Fig. 3.8b. The images in Fig. 3.8 were generated by applying a -6 dB threshold on the envelopes of CP, REC, and REC-FC (full width) and then estimating the margin strength [62]. The difference in contrast between the background and the target was 6 dB; therefore, a threshold of -6 dB was considered. A threshold was applied to segment the target from the background, i.e., pixel values greater than -6 dB were considered part of the target and were assigned a value of one while all other pixel values were assigned a value of zero. Margin strength was then estimated to detect the strength of the distinct boundaries generated by applying the -6 dB threshold. Margin strength [62] is defined by the following equation:

$$MS = E\left\{\sqrt{\left(\frac{dROI}{dx}\right)^2 + \left(\frac{dROI}{dy}\right)^2}\right\}, \tag{3.10}$$

where ROI is a two-dimensional region-of-interest within the envelope. From images of the margin strength, shown in Fig. 3.8, the targets' edges were more clearly defined and outlined for REC-FC when compared to CP. For REC this was not the case. However, when carefully examining REC versus CP, it was evident that REC had less background content around the target edges when compared to CP, allowing the boundaries to be traced.

The other cases evaluated were half-, third-, and fourth-width of CP impulse response, which would translate into a reduction by a factor of two, three and four in terms of axial resolution, respectively. The half-, third-, and fourth-width case FC filter banks were applied to both CP and REC as shown in Fig. 3.7(c-e). In simulations it

was observed that the lSNR values decreased with smaller subbands in the FC. Therefore, the decreasing lSNR values suggest that the corresponding loss in axial resolution outweighed the increase in contrast obtained. In the REC-FC simulations, the lSNR for the fourth-width case suffered a significant drop, which was attributed to the deterioration of axial resolution. However, REC-FC was still better than CP-FC in terms of lSNR. A slight decrease in lSNR of 2% was encountered when comparing CP to REC-FC (fourth-width). In terms of lSNR, the improvements obtained up to the third-width case quantified significant benefits of REC-FC over CP and CP-FC.

Histograms of the background and target regions for all four cases are shown in Fig. 3.9. From examination of the reference scans in Fig. 3.9(a), a large overlap in the distribution of grayscale pixel intensities between the background and the target existed. The overlap was due to the large spread in the standard deviation about the mean pixel value of these regions. In fact, the overlap of these regions for the CP and REC reference scans was 28%. A large overlap between these two regions was undesirable because it would decrease the ability to detect the target against the background. By using FC, the overlap was reduced to 18% for the full width case as shown in Fig. 3.9(b). This decrease in overlap can be attributed to a reduction of 11.6 and 11.7 in the standard deviation of pixel intensities about the mean for the background and the target regions, respectively. Moreover, as expected (Figs. 3.9(c-e)), the percent overlap for the half-, third-, and fourth-width for CP-FC cases decreased. However, the overlap obtained with CP-FC was higher than than with REC-FC.

Experimental results: ATS phantom +6 dB contrast lesion

Descriptions of the filter banks designed for the experimental implementation are given in Table 3.5. The filter banks deviated slightly from the values obtained for the computer simulation as the bandwidth of the source was slightly different. The resulting axial and lateral resolutions are given in Table 3.6. Again, as the subband width became smaller, a decrease in axial resolution was observed. Moreover, values of CNR and sSNR obtained for all four cases (full-, half-, third-, and fourth-width) in addition to the reference scans (CP and REC with no compounding) are provided in Table 3.7. Values for HPI, HO, and lSNR are summarized in Table 3.8. A trend similar to that observed in simulations

was observed in experiments in that the CNR and sSNR improved as the subband width became smaller. Furthermore, the improvements in terms of CNR, sSNR_B, and sSNR_T are shown in Fig. 3.6(a,b,c). The B-mode images representing these results are displayed in Fig. 3.10.

Examination of the reference scans in Fig. 3.10(a) revealed that by using the REC technique the speckle size was finer when compared to CP, which was also evident in the simulations. Next, FC was applied with subbands corresponding to the bandwidth of the original impulse response of the source under CP methods (full width) to improve contrast as shown in Fig. 3.10(b). For the full width case, the CNR, sSNR_B, and sSNR_T using REC-FC improved by 121%, 41%, and 57% over CP. Increases in CNR and sSNR were obtained while maintaining the same axial resolution that would be obtained by using CP methods. Similar to the simulations, the definition of object boundaries was enhanced in the experimental results because the REC B-mode image contained more detail when compared to CP. Therefore, when applying REC-FC this extra information could enhance the image boundaries obtained when compared to CP. Evaluating lSNR results shown in Fig. 3.6 suggests that by using REC the lSNR improved by 48% over CP, indicating improved target detectability. This would imply that the same lSNR value would be obtained for both CP and REC if a target of approximately 7.8 mm in diameter was imaged with REC rather than 15 mm as in CP. Use of the REC technique on an ultrasound imaging system significantly improved the detectability of small targets.

A comparison of experimental results with simulations revealed the improvement for the full width case in terms of sSNR_B and sSNR_T remained approximately the same, while the improvement in terms of CNR was larger in the experiment (121%) than in simulations (71%). The next case evaluated was half-width of CP impulse response. The half-width case was applied to both CP and REC as shown in Fig. 3.10(c). In comparing experimental results to simulations it was observed that the improvements for the half-width case in terms of sSNR_B and sSNR_T were quite similar, while the improvement in terms of CNR were larger in the experiment (231%) than in simulations (137%). There were two other cases evaluated, shown in Figs. 3.10(d) and 3.10(e). For the third- and fourth-width REC-FC cases, the lSNR dropped, but maintained higher values than

CP, with increases of 139% and 130%, respectively. This decrease was related to the visible effects of target edge blurring due to the resolution decrease in B-mode images. Although the lesion is still detectible for the third- and fourth-width REC-FC cases, it is not recommended to drive REC-FC beyond the half-width case if the best performance criteria for detecting a lesion is desired. This performance criteria is associated to the decision theoretic lSNR [57].

Histograms of the background and target regions for all four cases are shown in Fig. 3.11. Examination of the reference scans shown in Fig. 3.11(a) revealed that there was a large overlap in the distribution of grayscale pixel intensities between the background and the target. This overlap was due to the large spread in the standard deviation about the mean pixel intensity of these regions. In fact, the overlap of both these regions for the CP and REC reference scans was 35%. By using REC-FC, the overlap was reduced to 33% for the full width case as shown in Fig. 3.11(b). A 2% drop is significant in that it was achieved with no cost in axial resolution because the axial resolutions for CP and REC were the same. A major difference between simulations and experiments was that the mean pixel intensity value for the background region increased during simulations while the value decreased for experimental measurements. The mean pixel intensity values for the target increased for both simulation results and experimental measurements. This change in the mean pixel value may help explain how the CNR results improved drastically during experiments compared to simulations. Another factor that may have led to the greater improvement in CNR for experimental measurements versus simulations was the fact that the simulations did not contain noise. In using a coding technique and FC, noise may be further reduced leading to enhanced CNR over just the compounding effect alone. Furthermore, the overlap for the half-, third-, and fourth-width for CP-FC cases (Fig 3.11(c,d,e)) decreased; however, the overlap obtained with CP-FC was higher when compared to REC-FC. Moreover, the simulations only considered the position of the scatterers laterally. In other words, the amplitude did not vary throughout the axial extent of the image. Consquently, the mean of the pixels in the background did not drop because the amplitude was relatively constant. Nonetheless, it should be noted that although the overlap in pixel intensities between these two regions was reduced, the reduction in axial resolution was deteriorat-

ing image quality for the third- and fourth-width cases. This reduction in image quality could reduce the ability to detect small targets. This effect was not as noticeable in the simulation results except for the fourth-width case.

Experimental results: hyrdrogel phantom with lesions of different sizes

The B-mode images obtained for the hydrogel cone phantom for various target lesion diameters are displayed as follows: 8 mm in Fig. 3.12, 5 mm in Fig. 3.13, and 3 mm in Fig. 3.14. The values of CNR, sSNR_T and sSNR_B for the hydrogel phantom for various lesion sizes and using various FC cases are shown in Tables 3.9, 3.10, and 3.11. The filter banks applied in this particular study were consistent with the parameters shown in Table 3.5.

The results for the 5 mm and 3 mm diameter cases can be characterized by large variability in the CNR and sSNR values. The variability in the results occurred because the regions of interest used to obtain the statistical measures of CNR and equivalently sSNR became smaller as the lesion diameter became smaller. Evaluation of the statistical measures in smaller regions of interest when using FC was problematic because of the widening of the speckle patterns as the subband widths became smaller. A MATLAB simulation was performed to evaluate the relationship between the number of pixels used in the calculation of CNR and the variance of the CNR estimates. The simulation consisted of a phantom with two regions: one representing the background and one the lesion as shown in Fig. 3.15(a). A total of 25 phantoms were imaged using CP methods and the properties of the background and lesion regions were represented by the parameters of the experimental study (i.e., the contrast between them was +6 dB). From the simulations it was estimated that around 10,000 pixels were needed to obtain a CNR with a standard deviation of 0.10 as shown in Fig. 3.15(b). The regions of interest contained 15,000, 4000, and 2250 pixels for the 8 mm, 5 mm, and 3 mm cases, respectively. The results in Fig. 3.15(b) suggests that the sample sizes were too small to obtain a precise estimate of the statistical estimates of CNR and sSNR for the 5 mm and 3 mm cases. Similar conclusions can be established regarding the sample size for the lSNR metric as it is heavily dependent on contrast. Therefore, values listed for the CNR and lSNR for the smaller lesion sizes are not as reliable as those listed for larger

lesions where more samples are available.

Combination of REC-FC images: Enhanced REC-FC

Although improvements in contrast are obtained, a detriment of REC-FC is that the smaller the subband width the more the axial resolution is degraded. As a result, the REC-FC images appeared blurry as the subband width became smaller. A method was proposed that could provide the improvements in contrast obtained with REC-FC without sacrificing as much axial resolution. The proposed method was to sum a collection of compounded images constructed from different subband widths. For the purpose of this document, this study shall be known as enhanced REC-FC, or eREC-FC. In this study, eREC-FC utilized the sum of the following images: REC reference image, REC-FC (full width), REC-FC (half width), REC-FC (third-width), REC-FC (fourth-width), and REC-FC (eighth-width) to form an enhanced final REC-FC image. Theoretically, by summing all the compounded images along with the reference, the final enhanced image hawould have an axial resolution that appeared similar to the full width or equivalently the original resolution obtained with CP. The results of summing the envelope of the reference and subbands is shown in Fig. 3.16. Evaluation of the pulse-width of the eREC-FC envelope at -10 dB in Fig. 3.16 indicated that the axial resolution was slightly better than the REC-FC full width case and the CP reference but worse than the REC reference.

The B-mode images for the various ATS phantom targets when applying eREC-FC are displayed as follows: +6 dB in Fig. 3.17, +3 dB in Fig. 3.18, -3 dB in Fig. 3.19, and -6 dB in Fig. 3.20. The CNR results obtained with eREC-FC are listed in Table 3.12. Examination of the eREC-FC and the reference B-mode images in Fig. 3.17-3.20 suggests that the spatial resolutions of the two images were quite similar; however, the eREC-FC image had improved image contrast (CNR) by an average of 133%. The CNR results obtained with eREC-FC were similar to the results obtained for the REC-FC third-width case regardless of the reference CNR value. These results were expected because averaging the images obtained for the full-, half-, third-, fourth-, and eight-width along with reference would provide a middle point between the third and fourth-width cases.

The B-mode images for the various hydrogel targets when applying eREC-FC are

displayed as follows: 8 mm in Fig. 3.21, 5 mm in Fig. 3.22, and 3 mm in Fig. 3.23. The CNR results obtained with eREC-FC are also listed in Table 3.12. Examination of the eREC-FC and the reference B-mode images in Figs. 3.21- 3.23 also suggested that the spatial resolutions of the two images were quite similar; however, the eREC-FC image had improved image contrast (CNR) by an average of 132%. The CNR for the hydrogel cone phantom obtained with eREC-FC were similar to the results obtained for the REC-FC third-width case regardless of the diameter of the lesion.

Therefore, with eREC-FC the B-mode images were drastically improved by increasing the CNR, which was between the CNR values estimated for the third-width and fourth-width REC-FC cases. Furthermore, these contrast improvements were achieved without sacrificing the axial resolution by a significant amount, which would occur under normal FC procedures.

3.1.4 Conclusion

A pulse compression and coded excitation technique, REC, was used to double the axial resolution, which translated into an increase in system bandwidth. The speckle reduction technique known as FC utilized this larger available bandwidth to improve image contrast in ultrasonic B-mode images. FC partitions the useable bandwidth by using subbands that are smaller than the system bandwidth to improve image contrast and reduce speckle noise but at the expense of axial resolution. Therefore, the major objective of this study was to establish the benefits of applying FC to REC to take advantage of the larger useable bandwidth to increase the number of subbands.

Simulations and experimental measurements were used to establish the usefulness of the REC-FC technique in enhancing image contrast and reducing speckle noise for various targets with different contrasts and diameters. The results from simulations and experiments suggested that REC-FC was a useful tool to obtain substantial improvements in image contrast and to enhance the boundaries between the target and the background. CNR, SSNR_B, and SSNR_T were increased in both simulations and experiments for all cases. Furthermore, in simulations and experiments, the overlap between the background and the target regions in the histograms of image intensity values was significantly reduced as the subbands decreased in width. lSNR increased in simulations

for all cases except the fourth-width case. However, lSNR from experiments suggested that pushing REC-FC to the third- and fourth-width cases may be unfavorable. In general, it was observed that REC-FC was always a step ahead of CP/CP-FC in terms of contrast improvement. This was due to the doubling of the axial resolution of the ultrasonic imaging system by using REC which allowed an increase in the number of subbands.

The REC-FC technique would require certain hardware infrastructure for an ultrasonic imaging system. The main component required would be an arbitrary waveform generator that can output the pre-enhanced chirp excitation signals. In addition, a digital signal processor is required in order to compress the received echoes. However, most ultrasonic imaging systems already contain digital signal processors, and versions capable of producing arbitrary waveforms on excitation are possible now. An additional experimental cost to using REC-FC in an ultrasonic imaging system is the requirement of acquiring the pulse-echo impulse response of the imaging system. Nonetheless, the approximate pulse-echo impulse response can be easily obtained by placing a known reflector at the focus of the source and exciting with a pulse.

3.2 Improving Quantitative Ultrasound using Coded Excitation Techniques

3.2.1 Introduction

In ultrasound a two-dimensional brightness image, known as a B-mode image, yields mostly qualitative information from a cross-section of the tissue being interrogated. These B-mode images are generated by digitally sampling radio-frequency signals backscattered from tissue which are then converted into a grayscale image by detecting the en-

Portions of Section 3.2 have been reprinted, with permission, from J. R. Sanchez, D. Pocci, and M. L. Oelze, "Use of a novel coded excitation scheme to improve spatial and contrast resolution of quantitative ultrasound imaging," *IEEE Trans. Ultrason. Ferroelect. Freq. Contr.*, vol. 56, 10, pp. 2111-2123, Oct. 2009, ©2009 IEEE, from J. R. Sanchez, D. Pocci and M. L. Oelze, "Using resolution enhancement compression to reduce variance of scatterer size estimates from ultrasonic backscattered signals," *Proceedings of the 2008 IEEE Ultrasonics Symposium*, pp. 36-39, 2008, ©2008 IEEE, and from D. P. Hruska, J. R.Sanchez, and M. L. Oelze, "Improved diagnostics through quantitative ultrasound imaging," *Proceedings of the 2009 IEEE Engineering in Medicine and Biology Society*, pp. 1956-1959, 2009, ©2009 IEEE.

velope. This process removes the frequency-dependent information contained in the backscattered radio frequency signal. However, additional quantitative information about the underlying tissue microstructure, structures that are smaller than the ultrasound wavelength, can be extracted from the frequency dependence of the backscattered radio frequency signals [63].

Quantitative ultrasound (QUS) imaging techniques based on ultrasonic backscatter have been used to characterize tissue and to successfully diagnose and monitor disease. Much of the theoretical foundation for tissue characterization using ultrasound spectral analysis was laid out by Lizzi et al. [63]. Applications where the frequency-dependent backscatter information was used to quantify tissues include ocular tumors [64–71], liver and kidney tissue characterization [71–75], prostate tumors [76, 77], breast tumors [78–84], and vascular abnormalities [85, 86]. These applications have established the potential importance of QUS in the ultrasonics community.

To model the scattering process for tissue characterization it is assumed that tissues conduct sound as an inhomogeneous fluid [87]. Furthermore, the model assumes scatterers of finite sizes that can be approximated by simple geometric shapes and therefore characterized by a size and concentration [82]. Moreover, the size and shape of the scatterers determine the magnitude at which a specific frequency of sound will be scattered [82]. Therefore, with QUS, the normalized backscattered power spectrum from a region of interest (ROI) can be parameterized and related to tissue microstructure [82]. For example, the effective scatterer diameter (ESD) and effective acoustic concentration of underlying scatterers can be estimated from the normalized backscattered power spectrum [82]. Parametric images can be constructed by associating the estimated scatterer properties with ROIs at different spatial locations. These ROIs correspond to pixels in the parametric image whose color or intensity corresponds to a particular parameter value. The size of the ROI corresponds to the spatial resolution of the parametric image and is dictated by the number of independent scan lines in the lateral extent and axially by the spatial distance delineated by a range gating function. By decreasing the sizes of the ROIs, the spatial resolution of the parametric image is improved. Unfortunately, a tradeoff exists between the accuracy and precision of the scatterer property estimates and the sizes of the ROIs [88]. Furthermore, one of the

most important factors reducing the effectiveness of QUS imaging techniques is the low contrast resolution between diseased tissues and normal tissues or between benign and malignant tumors. The contrast resolution of QUS images depends on the variance of QUS estimates. The variance of QUS estimates decreases with increasing bandwidth of the imaging system [82]. Therefore, an imaging system with larger bandwidth would yield lower variance in spectral estimates. A decrease in estimate variance will result in an increase of contrast resolution for QUS images.

The usefulness of parametric imaging for characterization and diagnosis of diseased tissue has improved due to the advancement of signal processing techniques that improve the accuracy of the estimates from backscatter. Recently, Kanzler and Oelze [89] improved QUS estimates of ESD in tissue-mimicking phantoms by using coded excitation and pulse compression. In that study, the increase in echo signal-to-noise ratio (eSNR) achieved through coded excitation resulted in increased depths (50%) at which accurate ESD estimates could be obtained versus conventional pulsing (CP) techniques. Kanzler and Oelze also observed that the coded excitation and pulse compression scheme had a minimal effect on the estimate variance because it reduced the estimate variance at a majority of depths by only a few percent.

The REC technique [18] was explored for improving both the bias and variance of QUS estimates, i.e., ESD estimates. The REC technique can increase the bandwidth of the ultrasonic imaging system by a factor of two without the presence of large sidelobes often observed with other coding and pulse compression techniques. In addition to the bandwidth enhancement, the REC technique has the typical coded excitation benefits, such as deeper penetration which is due to increases in the eSNR. Furthermore, a larger eSNR translates into a larger useable bandwidth of the imaging system. Usable bandwidth in this study of QUS imaging was defined as the segment of the backscattered power spectrum that is 6 dB above the noise floor. Chaturvedi and Insana [90] observed that the standard deviation in ESD estimates was inversely proportional to the bandwidth of the imaging system when using a spherical Gaussian model for scattering. Therefore, the goal of this study was to combine the REC technique with QUS, which will be described as REC-QUS, and evaluate the improvements in standard deviation of ESD estimates due to the enhanced bandwidth and gain in eSNR. Another goal was to

extend the tradeoff of estimate standard deviation and the spatial resolution of the parametric image (ROI size). Both a broadening of the bandwidth and gain in eSNR should yield improved QUS estimates, which in turn would improve the diagnostic capabilities of QUS imaging techniques for clinical applications.

3.2.2 Methods and procedures

QUS

The ESD can be estimated from the frequency dependence of the normalized backscattered power spectrum. To estimate the ESD from the normalized backscattered power spectrum, the following assumptions were made: multiple scattering was negligible, the scatterers were uniformly and randomly located spatially, and the distribution of scatterer sizes was small relative to the mean size. In soft tissues, the frequency dependence of the normalized backscattered power spectrum has been modeled by the acoustic intensity form factor, F, which is related to a 3D spatial autocorrelation function that describes the material properties of the scatterers [63,91]. For soft tissues, the theoretical power spectrum [91] is formulated by

$$P_{theor}(f) = B(L,q)C(a_{eff},n_z)f^4F(f,a_{eff}), \tag{3.11}$$

where f is the frequency; B is a constant that depends on L, which is the axial length of the range gate, and on q, which is the ratio of the source radius to distance from the ROI; C is a constant depending on the average effective radius a_{eff} of the scatterers; and n_z is the effective acoustic concentration (product of the number density of scatterers times square of the relative impedance difference between the scatterers and surrounding tissues) [82].

The normalized power spectrum is calculated through [92]

$$P_{norm}(f) = \frac{A(f,L)}{N}\left(\frac{R}{2}\right)^2 \sum_{n=1}^{N} \frac{P_m(f)}{P_{ref}}, \tag{3.12}$$

where A is an attenuation compensation function, N is the number of gated scan lines in the ROI to be averaged, P_{ref} is a reference power spectrum, R is the reflectivity of

a planar surface used to obtain the reference power spectrum, and $P_m(f)$ is the power spectrum calculated from a range gated signal. The reference power spectrum, P_{ref}, was obtained by measuring the output of the transducer when a Plexiglas surface was positioned at the focus of the source [63].

QUS: Attenuation compensation

Frequency-dependent attenuation alters the shape of the power spectrum as attenuation increases with frequency. Hence, if the attenuation is not compensated for, the ESD will be overestimated. In simulations and experiments, a point compensation scheme was used. Point compensation [91] is described by

$$A_{pc}(f, x) = e^{4\alpha(f)R_1}, \tag{3.13}$$

where $\alpha(f)$ is the frequency-dependent attenuation and R_1 is the distance between the front-end of the object and the front-end of the the gated region.

QUS: Bandwidth

As previously stated, QUS techniques that make use of spectral information would be greatly improved by larger bandwidth imaging systems. Larger bandwidth leads to smaller variance in spectral estimates in QUS. Smaller variance in spectral estimates means that tissues will be more differentiable with QUS imaging techniques. The variance of ESD estimates when assuming a Gaussian form factor is inversely proportional to the bandwidth squared of the imaging system and is described by the following equation [82, 90]:

$$var\widehat{D} = \frac{2.09 \times 10^{-2}}{D^2}\left[\sum_{j=1}^{M} f_j^4 - M \cdot E\{f^2\}^2\right]^{-1}, \tag{3.14}$$

where $\widehat{D}$ is the estimated ESD, D is the actual ESD in the ROI, f is frequency, f_j are frequency points in the analysis bandwidth that are uncorrelated, and M is the total number of data points used in the analysis bandwidth. Furthermore, (3.14) indicates that the variance in scatterer property estimates is inversely proportional to the ESD

squared. Note that although the expression in (3.14) is only true for monodisperse scattering ensembles, the bandwidth-variance relationship still holds for a distribution of scatterer sizes.

Computer simulations

Computer simulations were carried out in MATLAB (Mathworks, Natick, MA) to characterize the performance of the REC-QUS technique. The simulations used a received pulse-echo pressure field model [93] described as

$$g'[x, y, t] = h_1(t) * f(x, y) * h_{pe}(y, t), \tag{3.15}$$

where x represents the axial spatial coordinate, y represents the lateral spatial coordinate, $f(x, y)$ is the scattering function, and $h_{pe}(y, t)$ is the modified pulse-echo spatial impulse response that takes into consideration the geometry of the transducer to the spatial extent of the scattered field (beam diffraction).

The pulse-echo impulse response, $h_1(nT, x)$, for CP was approximated by

$$h_1(t) = e^{-\frac{t^2-\tau}{\sigma_t^2}} \cos(\omega t), \tag{3.16}$$

where σ_t^2 is the second central moment of the Gaussian pulse which dictates the bandwidth of the pulse. A shift, τ, was added to $h_1(t)$ to make the pulse causal. The generated pulse-echo impulse response was located at the focus of a 10 MHz single-element transducer (f/4) with a -6 dB fractional bandwidth of 80%.

For REC, the impulse response function, $h_2(t)$, was constructed to have a -6 dB fractional bandwidth of 150% by gating a sinusoid of four cycles with a Hanning window

$$w(n) = \begin{cases} 0.5(1 - \cos(\frac{2\pi n}{L_H - 1})), & 0 \leq n \leq L_H - 1 \\ 0, & \text{otherwise,} \end{cases} \tag{3.17}$$

where n is an integer and L_H is the number of samples in the window. A Hanning window of length $L_H = 24$ was used.

The spatial response for a circular focused piston source was simulated as a circular

Gaussian beam which is defined as

$$h_{pe}(y,t) = \delta(t - \frac{2R_d}{c}) e^{\frac{-y^2}{\sigma_y^2}}, \tag{3.18}$$

where R_d is the distance from the source to target in space, c is the speed of sound of the medium which was set to 1540 m/s, and σ_y is the -6 dB lateral beamwidth which is equal to 0.62 mm.

Three different phantom types, S1, S2, and S3 were simulated. Ten simulations were performed for the first two types of phantoms, S1 and S2, while one simulation of the third type, S3, was performed. Descriptions of the first two simulated phantoms are shown in Table 3.13. Descriptions of the third phantom are shown in Table 3.14. Phantoms S1, S2, and S3 contained an average of 15 point scatterers per resolution cell volume. These scatterers had an f^4 dependence on the backscattered power spectrum. However, to model soft tissue scattering and to obtain ESD estimates, the simulated phantoms were modified by the spherical Gaussian form factor [91]. The spherical Gaussian form factor was used to model soft tissue scattering which is described by

$$F_{Gauss}(f) = e^{-12.159 f^2 a_{eff}^2}. \tag{3.19}$$

The spherical Gaussian form factor has been used by various researchers to model the scattering of soft tissues [66, 82, 91, 94–96]. In addition, the backscattered data was reduced by the frequency-dependent attenuation corresponding to the distance of the scatterer from the source. The attenuation was set to 0.5 dB MHz^{-1} cm^{-1}. Phantom S1 was used to evaluate the effects that REC had on the spatial resolution of QUS images due to the increase in bandwidth. Phantom S2 consisted of the same parameters of phantom S1 except that it contained a cylindrical lesion of 6 mm radius that was centered in a background region. Phantom S2 was used to evaluate the effects of REC on the contrast resolution of QUS images due to the improvements in standard deviation of ESD estimates. Phantom S3 consisted of the same parameters of phantom S2 except that it contained three cylindrical lesions of 6 mm radius. Phantom S3 was used to evaluate the contrast resolution achievable from lesions with different scatterer diameters that were imaged with the same source. Phantoms S1, S2, and S3 were placed

40 mm from the simulated source which had a focal depth of 50 mm.

The backscatter coefficient estimates [92] were obtained by

$$\sigma_b(f) = \frac{3.87(R_0 + R_1)^2}{A_o L} P_{norm}(f), \tag{3.20}$$

where A_o is the surface area of the transducer, R_0 is the on-axis distance between the transducer and the front-end of the object being imaged, and R_1 is the distance between the front-end of the object and the front-end of the the gated region. From the frequency dependence of the backscatter coefficient the parametric images of ESD can be obtained.

The received simulated radio frequency backscatter data were sampled at a rate of 100 MHz and the transducer was translated laterally in increments of 0.31 mm (50% beam overlap). For phantom S2 and S3, the sizes of ROIs were selected based on recommendations from previous analysis of ROI versus estimate bias and variance [88]. Axially, individual scan lines were gated with a rectangular window of a length corresponding to 5.5 CP axial pulse lengths. Laterally, a distance of five lateral beamwidths was used, corresponding to 10 scan lines because data were acquired with a 50% beamwidth overlap between scan lines. Therefore, each ROI was a rectangle 1.52 mm x 4.15 mm. However, ROIs were overlapped both laterally and axially by 66%; therefore, the effective ROI size after averaging was 0.50 mm x 1.38 mm. For phantom S1, the size of the ROI was varied in the axial extent as the goal of this study was to evaluate the estimate bias and standard deviation as a function of gate length.

Estimates of ESD were obtained by approximating the measured power spectrum by a best-fit line technique [82]. Specifically, estimates were obtained by comparing the logarithm of the measured backscattered power spectrum (3.12) with the logarithm of the theoretical power spectrum (3.11) through the equation,

$$10 \log_{10} P_{norm}(f) - 10 \log_{10} f^4 \approx m(a_{eff}) f^2 + b(n_z, a_{eff}, L, q). \tag{3.21}$$

Equation (3.21) describes a straight line, $y = mx + b$ where $x = f^2$, m is the slope and is a function of a_{eff}, and b is the intercept and is a function of a_{eff}, n_z, q, and L. Finally, estimates were obtained by using least-squares analysis to find the best-fit line to the

measured and processed data from (3.21) using an analysis bandwidth corresponding to the -6 dB bandwidth of the simulated source.

Experimental Setup

Scatterer property estimates from experiments were obtained to validate the improvements afforded by the REC-QUS technique in an experimental setting. A single-element weakly-focused (f/4) transducer with a center frequency of 10 MHz was used to image phantoms by translating the transducer laterally across the phantom. The transducer had a -6 dB pulse-echo bandwidth of 80% along with a -6 dB pulse-echo beamwidth of 0.67 mm. These parameters were estimated using the wire technique [97] for transducer characterization. Using REC the -6 dB pulse-echo bandwidth was enhanced to 155%. There were two different experimental setups utilized; one for CP and another one for REC experiments. These setups would contain different noise levels due to the use of different excitation systems. Therefore, to avoid errors in the comparisons, the noise levels were normalized so that they contained the same eSNR before compression. Normalization of eSNR was accomplished by adding zero-mean white Gaussian noise to the CP radio frequency echo waveforms because REC had the lower eSNR before compression. The two experimental setups are described by Fig. 3.24.

1. Conventional pulsing experimental setup: The transducer was excited by a pulser-receiver (Panametrics 5900, Waltham, MA) which was connected to a Ritec diplexer (Warwick, RI). The echo waveform was received by a different pulser-receiver (Panametrics 5800, Waltham, MA) which then was displayed on an oscilloscope (Lecroy 9354 TM, Chester Ridge, NY) for visual verification. The echo signal was recorded at a rate of 100 MHz by a 12-bit A/D (Strategic Test Digitizing Board UF3025, Cambridge, MA) for further processing by a PC. A diagram of the experimental setup for CP is shown in Fig. 3.24.

2. REC experimental setup: The pre-enhanced chirp was generated in MATLAB and downloaded to an arbitrary waveform generator (Tabor Electronics W1281A, Tel Hanan, Israel). The excitation signal was amplified by a radio frequency power amplifier (ENI 2100L, Rochester, NY). The amplified signal (50 dB) was

connected to the transducer through a diplexer (Ritec RDX-6, Warwick, RI). The echo signal was received by a pulser-receiver (Panametrics 5800, Waltham, MA), which was displayed on an oscilloscope (Lecroy 9354 TM, Chester Ridge, NY) for visual verification. The echo signal was recorded at a rate of 100 MHz by a 12-bit A/D (Strategic Test Digitizing Board UF3025, Cambridge, MA) for further processing by a PC. A diagram of the experimental setup for REC is shown in Fig. 3.24.

Measurements from four physical phantoms were obtained to evaluate the performance of REC-QUS versus conventional QUS methods. Descriptions of the four physical phantoms used in the experiments are shown in Table 3.15 and Table 3.16. The phantoms were cylindrical samples bounded within an acrylic housing that contained a 25 μm Saran Wrap plastic film (Dow Chemical, Midland, MI) [98] on the parallel flat surfaces. The Saran Wrap layer served as a window for transmission of the ultrasound waves between water and the tissue-mimicking phantom. Therefore, to obtain correct estimates of phantom parameters the frequency-dependent transmission coefficients of the Saran Wrap layers need to be compensated. The transmission coefficient for a single layer of Saran Wrap is given by [98]

$$T(k) = \frac{2Z_f}{(Z_i + Z_f)\cos(k_{saran}l) + j(Z_{saran} + \frac{Z_i Z_f}{Z_{saran}})\sin(k_{saran}l)}, \tag{3.22}$$

where Z_i is the acoustic impedance of the incident material (Z_i = 1.49 MRayls), Z_f is the acoustic impedance of the final material (Z_f = 1.49 MRayls), and Z_{saran} is the acoustic impedance of the Saran Wrap layer of length l. k_{saran} is the wave number in the layer and is described by

$$k_{saran} = \frac{2\pi f}{c_{saran}} - j\alpha(f), \tag{3.23}$$

where c_{saran} is the speed of sound and α the frequency-dependent attenuation coefficient of the Saran Wrap layer. More information about phantoms A and B can be found in [98]; likewise, more information about phantoms C and D can be found in [99].

The received radio frequency backscatter data were sampled at a rate of 100 MHz and the transducer was translated laterally in increments of 0.33 mm (50% beam overlap).

The sizes of ROIs were again selected from recommendations of appropriate ROI size versus estimate bias and variance [88]. Axially, individual scan lines were gated with a rectangular window of a length that would correspond to 15 CP axial pulse lengths. Laterally, five lateral beamwidths were used, which corresponds to 10 scan lines because data were acquired with a 50% beamwidth overlap between scan lines. Therefore, each ROI was a rectangle 3.3 mm x 3 mm. However, ROIs were overlapped both laterally and axially by 66%; therefore, the effective ROI size after averaging was 1.1 mm x 1 mm.

Estimates of ESD were obtained by minimizing the average squared deviation (MASD) as a function of ESD,

$$\widehat{D} = \min_{ASD}(E\{(X(f, ESD) - E\{X(f, ESD)\})^2\}), \tag{3.24}$$

where $X(f, ESD)$ is $10\log_{10}(\sigma_b/\sigma_0)$. σ_0 is the theoretical backscatter coefficient obtained from Faran's theory [100, 101] and σ_b is the backscatter coefficient from the phantom. σ_b was estimated by using a broadband substitution method for weakly focused transducers [92]. Estimates of the backscatter coefficient were obtained using Eq. (3.20). The mean of $X(f, ASD)$ was subtracted from $X(f, ASD)$ because the ESD estimate depends only on the frequency dependence of the backscatter coefficient and not the magnitude.

During experiments, large echoes from the front surface of the phantoms were clipped because the A/D card had a voltage limitation of ± 0.5 V. This was an engineering tradeoff because gain was applied so that the backscatter behind the front surface fully spanned the dynamic range of the A/D card. However, a consequence of clipping AM and FM modulated signals is that after compression large sidelobes are introduced. As a result, the portion of the signal that was being clipped was replaced with zero-mean white Gaussian noise that contained the same variance introduced by the system [89].

In measurements, the phantoms were placed in a tank of 20 °C degassed water such that the fronts of the phantoms were perpendicular to the beam axis of the transducer as shown in Fig. 3.25. Measurements of backscatter for all phantoms were obtained for three distances of R_1: 10 mm, 15 mm, and 20 mm. Each distance represents a shift in the placement of the focus within the phantom. R_0 was decreased by the same amount R_1 was increased in order to maintain the sum of R_0 and R_1 constant. QUS parametric

images for experimental measurements were generated by compounding the estimates for all three distances listed above. Reference pulses were obtained by reflecting an incident pulse off a Plexiglas surface for both CP and REC. Because estimates require a normalization with a reference spectrum that is located at the center of the gate, reference pulses were obtained in increments of 500 μm that spanned the entire depth-of-focus.

Quality metrics

To assess the REC-QUS technique, numerical simulations were implemented, and experimental measurements were acquired. The simulations and experiments used REC to increase the -6 dB bandwidth of the imaging system for QUS analysis and results were compared to CP methods. Therefore, to evaluate the performance of the REC-QUS technique against CP the following quality metrics were used:

1. Standard deviation: Estimate standard deviation quantifies the estimation precision and is arguably the most important metric of QUS imaging. The main limitation of QUS imaging techniques when differentiating and characterizing tissues is the overlapping of estimate values due to the size of estimate standard deviation. By reducing estimate standard deviation, QUS imaging techniques will be more sensitive to tissue differences and improve diagnostic capability.

2. Bias: Estimate bias is the deviation of the simulated or measured QUS parameter from a reference scatterer diameter. The accuracy of the underlying structure was quantified by the bias of the scatterer property estimates. However, when evaluating the experiments with physical phantoms, estimate mean was used over estimate bias because the phantoms contained scatterers with varying diameters. In these cases, the out of range, i.e., the percentage of size estimates that were not bounded between the maximum and minimum scatterer diameter, were tallied to obtain a measure of correctness of estimation (estimates that do not deviate from the range).

3. Contrast-to-noise ratio (CNR): CNR is a quantitative measure that was used to assess image quality and describe the ability to perceive a lesion from the

background region or lesion-free region. CNR [34] is defined as

$$CNR = \left| \frac{\mu_B - \mu_L}{\sqrt{\sigma_B^2 + \sigma_L^2}} \right| \tag{3.25}$$

where μ_B and μ_L are the mean brightness of the background and the target lesion and σ_B^2 and σ_L^2 are the variance of the background and target, respectively. To avoid possible errors in the calculations due to attenuation, the evaluated ROIs in the background and the target lesion were of the same size and located at the same depth. CNR is a unitless quantity.

4. Histogram overlap: Histogram overlap is the percentage of pixels in the background and target lesion histograms that share the same pixel intensity. Histograms were made for same-sized regions for the target lesion and the background adjacent to the target. Like CNR, the histogram overlap is a measure of the detectability of the lesion from the background. Note that the number of points in the histograms varied based on the sizes of the ROIs.

3.2.3 Results

Simulations

The results form simulations of phantom S1 consisted of estimates obtained with varying sizes of the axial gate. The axial gate lengths evaluated for CP and REC were dictated by the pulse length at -15 dB. One CP pulse length corresponded to 0.277 mm while for REC one pulse length corresponded to 0.169 mm. The bias and standard deviation of ESD estimates for phantom S1 are shown in Fig. 3.26.

Simulations of phantom S2 consisted of obtaining ESD estimates for the target lesion and the background region. The purpose of this simulation was to evaluate the quality of REC-QUS parametric images when two simulated tissues have a small difference in ESD values. Changes in standard deviation of ESD estimates were obtained by varying the size of the axial gate with the simulations of phantom S2. For this study, the image quality metrics were the CNR and the histogram overlap, which were generated by assessing the lesion and background regions of the QUS parametric images. For a gate

length corresponding to the 15 REC pulse lengths (2.54 mm), the CNR was 1.28 ± 0.52 for CP and 2.47 ± 0.42 for REC. Comparisons of CNR as a function of CP pulse lengths for phantom S2 are shown in Fig. 3.27.

Histogram analysis further highlighted the improvements obtained by using REC-QUS over conventional QUS. CNR allowed quantification of the improvement in contrast while histogram overlap was used to evaluate the overlap in intensity between QUS pixels in the lesion and background regions. In addition, histogram overlap allowed quantification of the optimal gate length when examining the tradeoff between axial resolution and contrast resolution. Note that analysis of the overlap regions did not contain ROIs that were near the perimeter of the lesion. Histogram overlap as a function of pulse length for phantom S2 is shown in Fig. 3.27.

Conventional B-mode images for phantom S2 are shown in Fig. 3.28. The CNR values for the B-mode images of CP and REC shown in Fig. 3.28 were both 0.14. The parametric images for the QUS estimates of ESD for the following axial gate lengths: 0.61 CP pulse lengths (1 REC pulse length), 3.05 CP pulse lengths (5 REC pulse lengths), 6.10 CP pulse lengths (10 REC pulse lengths), and 9.15 CP pulse lengths (15 REC pulse lengths), are shown in Figs. 3.29. Histograms corresponding to these are shown in Figs. 3.30. Bias, standard deviation, histogram overlap and CNR for the parametric images shown in Figs. 3.29 and the values versus CP pulse length are listed in Table 3.17-3.18.

Simulations of phantom S3 consisted of obtaining ESD estimates for the target lesions and the background region. The purpose of this simulation was to evaluate the quality of REC-QUS parametric images when using one source for imaging simulated tissues with different ESDs (30, 60 and 90 μm) with respect to a background medium (50 μm). For this study, the image quality metric utilized was CNR. CNR values were generated by assessing the lesion and background regions of the QUS parametric images. Conventional B-mode images for phantom S3 are shown in Fig. 3.31. The parametric images for the QUS estimates of ESD are shown in Fig. 3.32. CNR results for the axial length [88] of 15 REC pulse lengths (2.54 mm) along with the standard deviation of the ESD estimates are shown in Table 3.19.

Experiments

B-mode images for CP and REC along with a parametric image overlay for all phantoms are shown in Fig. 3.33. Furthermore, the ESD and standard deviation of ESD estimates as a function of depth for all phantoms are shown in Fig. 3.34. The results for out of range and standard deviation of ESD estimates for all depths combined are shown in Table 3.20.

The ESD results in Fig. 3.34 demonstrate that REC-QUS obtained improved estimates when compared to conventional QUS methods using CP. Moreover, the standard deviation of ESD estimates in Fig. 3.34 corroborate that improvements in standard deviation were obtained by increasing the useable bandwidth through REC. Furthermore, by using REC over CP a decrease in the standard deviation of ESD estimates of 34%, 75%, and 71% were obtained for phantoms A, C, and D, respectively.

3.2.4 Discussion and conclusions

Simulations

For phantom S1, the bias results in Fig. 3.26a demonstrated that REC-QUS obtained improved estimates when compared to conventional QUS methods using CP. Additionally, the standard deviation results in Fig. 3.26b provided evidence that the bandwidth enhancement generated by using REC resulted in significant improvements in estimation error. For ROIs of CP axial pulse lengths of one through four, a mean decrease of 52% in standard deviation was obtained by using REC. Furthermore, by using REC over CP an approximate 43% decrease in the standard deviation of ESD estimates was obtained for ROIs with axial pulse lengths greater than four. More importantly, standard deviation when obtaining estimates with an axial length of 15 CP pulse lengths was 7.09 for CP. For REC the same standard deviation was achieved with an axial length of 1.33 CP pulse lengths. These results suggest that the same standard deviation obtained with conventional QUS can be achieved by using REC-QUS but with a smaller axial pixel size for the parametric image. In fact, the axial pixel in the parametric image would be approximately less than twice the size of the axial pixel length in a conventional B-mode image.

For phantom S2, fitting the CNR data of Fig. 3.27 with a line in the least-squares sense provided a slope of 0.09 and an intercept of 0.41 for CP, while a slope of 0.20 and an intercept of 0.64 was obtained for REC. These results suggested that a greater increase in contrast occurred using REC, in addition to an improvement in axial resolution. In fact, REC-QUS parametric images achieved an average of 38% increase in contrast when compared to the conventional QUS parametric images generated using CP. Furthermore, observation from Fig. 3.27 indicates that for REC-QUS, histogram overlap reached approximately 0% for a gate length of 9.5 CP pulse lengths, while for conventional QUS 0% was achieved at 17.3 CP pulse lengths. These results indicate that the optimal axial gate length, where the parametric image using REC yielded optimal contrast, was around 10 CP pulse lengths. By using REC-QUS with a gate length of 10 CP pulse lengths as opposed to conventional QUS with a gate length of 17 CP pulse lengths, a gain of 70% in axial resolution in the parametric image was achieved.

Examination of the REC parametric images in Figs. 3.29 reveals that by using REC-QUS the lesion was more clearly observed in all cases when compared to conventional QUS methods for the same gate length. The contrast increased as the gate length increased. Furthermore, histogram analysis extended the notion of improved contrast and target detectability by illustrating the increased separation between the target and background as the gate length increased. These observations were supported by the improvements in contrast and reduction of histogram overlap as shown in Fig. 3.27. CNR results indicated that with both REC-QUS and conventional QUS an improvement in contrast can be achieved when compared to the conventional B-mode images shown in Fig. 3.28. Moreover, the decrease in histogram overlap using REC-QUS led to improved detection and differentiation of the lesion from the background when compared to CP.

A further benefit of REC-QUS is observed by comparison of the bias and standard deviation for the background regions in REC and CP as shown in Table 3.17 and Table 3.18. For example, for ROIs of 15 REC pulse lengths (9.15 CP pulse lengths) [88], the bias for CP was -3.76 μm for the background and -2.01 μm for the lesion while the bias for REC was 2.71 μm for the background and -7.28 μm for the lesion. Similarly, the standard deviation for ROIs of 15 REC pulse lengths (9.15 CP pulse lengths) for CP was 6.89 μm for the background and 5.41 μm for the lesion while for REC the standard

deviation was 2.66 μm for the background and 2.08 μm for the lesion. These results suggest that for conventional QUS the standard deviation of ESD deteriorated as the diameter of the scatterer decreased. Conversely, using REC the performance of QUS was increased because it resulted in accurate estimates for a smaller scatterer diameter due to the large ka range obtained by increasing the useable bandwidth. This larger ka range suggests that by using REC-QUS, scatterers with different diameters could be quantified by using the same transducer as opposed to conventional QUS where multiple source may be needed.

Recall that the difference in scatterer diameter between the lesion and the background was 10 μm for phantom S2. The small difference in scatterer diameter was evaluated to establish the tradeoff between axial length and standard deviation. Figure 3.29(a) has poor contrast when compared to Fig. 3.29(d); however, the axial pixel length was the same as the B-mode image in Fig. 3.28, which would allow smaller targets to be detected. Conversely, Fig. 3.29(d) has good contrast when compared to Fig. 3.29(a). However, the axial pixel length was 15 times the axial pixel length of the B-mode image in Fig. 3.28. As a result, this axial pixel length provided a smooth high contrast image but at the expense of potentially not detecting smaller targets. Naturally, targets could be easily detected if the difference in scatterer diameter were larger. In summary, the studies with phantom S2 suggested that REC-QUS could be used to extend the tradeoff between axial length and contrast to improve target detectability.

For phantom S3, the results in Table 3.19 indicate that REC-QUS obtained improved results over CP in terms of CNR. Specifically, for the 30 μm scatterer diameter lesion, the CNR improved by 45%. For the 60 μm and the 90 μm scatterer diamter lesions, the improvements increased to 152%. In terms of estimate standard deviation, REC obtianed improved results over conventional QUS by 77%, 90%, and 62% for the 30, 60, and 90 μm scatterer diameter lesions, respectively. A lateral profile of the parametric image in Fig. 3.32 is shown in Fig. 3.35. This profile illustrates how closely REC-QUS tracks the actual scatterer diameter and how CP failed to obtain accurate estimates as the scatterer diameter became smaller. The significance of these results lies in the fact that contrast improvements and reduction of estimated standard deviation were achieved by using one source instead of multiple sources. Multiple sources with different

center frequencies could be used to obtain ka ranges that might be optimal to the ESD estimates in phantoms. However, by using REC the ka range increased significantly to the point that targets with various scatterer diameters could still be evaluated with minimum estimation error.

Experiments

The ESD results in Figs. 3.34 demonstrated that REC-QUS had a better ability to obtain improved estimates when compared to conventional QUS methods using CP. Moreover, the standard deviation of ESD estimates in Figs. 3.34 corroborates that improvements in standard deviation were obtained by increasing the useable bandwidth through REC. Furthermore, by using REC decreases in the standard deviation of ESD estimates of 34%, 75%, and 71% were obtained for phantoms A, C, and D, respectively, compared to CP.

The standard deviations from combining all QUS ESD estimates for phantom B (Table 3.20) were 9.6 for CP and 10.9 for REC. At first glance, for this particular phantom these results suggest that conventional QUS was preferable over REC-QUS. Evaluating the results in Fig. 3.34(b), the standard deviation of REC-QUS was always lower than conventional QUS by using CP at any particular depth. However, analysis using Fig. 3.33(b) along with Fig. 3.34(b) helps explain why the standard deviation of QUS ESD estimates using all depths combined was larger for REC than for CP. In REC-QUS the ESD decreased as the depth increased, causing a large standard deviation when calculating the standard deviation from all depths combined. As a consequence, conventional QUS had a better overall standard deviation but a poor predictive ability because the majority of estimated values were out of the range of scatterers in the phantom.

Overall, as the penetration depth increased, the improvements in the standard deviation of ESD estimates using REC increased. This improvement was due to the increase in eSNR by using coded excitation and the increase in the bandwidth. REC-QUS resulted in more accurate ESD estimates because REC-QUS obtained a larger percentage of estimates that were within the true range of scatterer diameters.

REC-QUS extended the results by Kanzler and Oelze [89]. In [89], improved es-

timation bias versus penetration depth was obtained because of the increase in eSNR by using coded excitation. REC can achieve similar results as it produces an increase in eSNR by exciting the source with a pre-enhanced chirp. Moreover, the extension to their work comes from using the pre-enhanced chirp, which also increased the useable bandwidth by a factor of two. Therefore, the results were extended by combining REC with QUS techniques as the larger useable bandwidth resulted in a reduction in the standard deviation of ESD estimates. Smaller standard deviations aid in the classification of tumors and tissue typing.

Previous studies have indicated that simple QUS techniques can differentiate between different kinds of tumors in animal models of cancer [83,84]. Specifically, a study by Oelze and Zachary [83, 84] evaluated conventional QUS techniques *in vivo* on mice with transplanted 4T1 mammary carcinomas and EHS sarcomas. The objective of the study was to classify the two types of tumors. However, estimates of ESD and effective acoustic concentration contained a significant amount of overlap. Furthermore, in that study statistical differences were only observed when the bandwidth was limited to certain regions of the power spectra. By having more available bandwidth for estimates, it is more likely that with REC-QUS regions of bandwidth could be chosen that would yield estimates that produce statistically significant differences. Therefore, in pre-clinical and clinical settings, REC-QUS has a greater potential to markedly improve the differentiation between these different types of tumors because of the reduced estimate variance, lesion-to-background contrast, larger ka range, and smaller axial pixel length. A significant advantage that REC-QUS has over conventional techniques is that because of the increased available bandwidth, different scales of structure may be observed because of different scales of structure dominate the scattering at different frequencies. In other words, REC-QUS has the potential to assess tissues using multiple scales with one source as opposed to conventional QUS techniques where multiple sources with different center frequencies may be needed.

A potential limitation of REC-QUS is the fact that sources with larger bandwidth tend to have a large center frequency shift due to the frequency-dependent attenuation. Besides the center frequency shift, a decrease in the -6 dB bandwidth is encountered which would effectively reduce the variance improvements obtained with REC-QUS.

However, if bandwidth is defined as the 6 dB level above the noise, REC-QUS will still provide a larger bandwidth for analysis. Furthermore, it should be noted that Phantom C and Phantom D contained scatterers in the range of 45 to 53 μm diameter but with different attenuation coefficients 0.5 and 0.8 dB $MHz^{-1}cm^{-1}$, respectively. Therefore, because of the higher attenuation coefficient in Phantom D, the standard deviation of the ESD estimates increased by 18% when using REC-QUS. As a comparison, with conventional QUS a 1% increase in the standard deviation of the ESD was observed. Nonetheless, a 70% decrease in the standard deviation of ESD was obtained when using REC-QUS over conventional QUS.

3.3 Figures and Tables

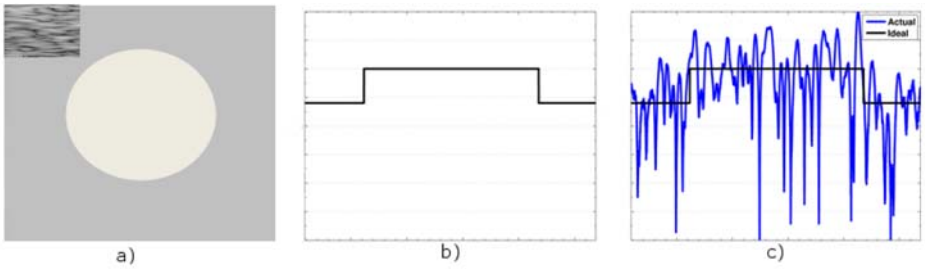

Figure 3.1: Example showing what speckle does to an ultrasound image. (a) An ideal image of a lesion (except the upper left corner which shows a region full of speckle), (b) the axial profile of the ideal lesion (the ideal scan line), (c) the resulting scan line after the lesion is scanned with ultrasound.

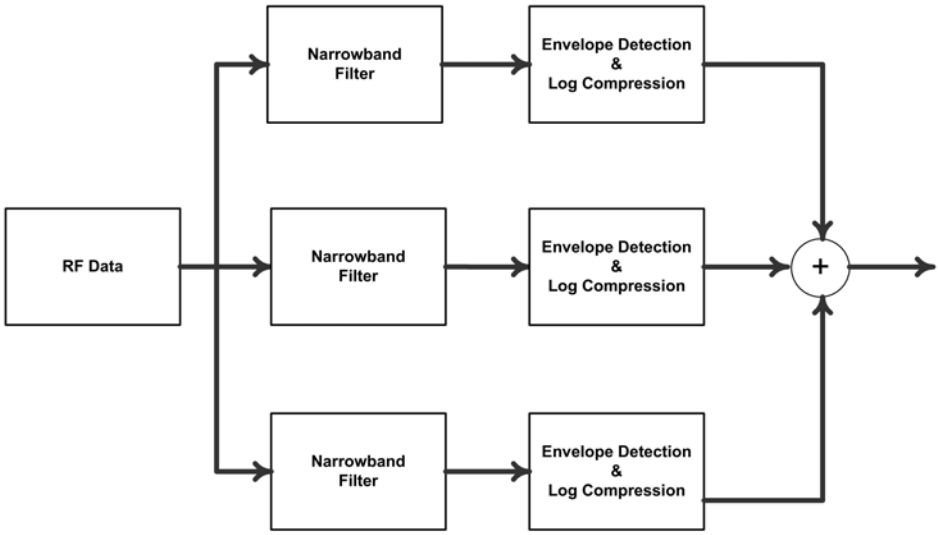

Figure 3.2: Block diagram of an FC scenario with three subbands. Each subband consists of a narrowband filter that contains a different center frequency when compared to other subbands.

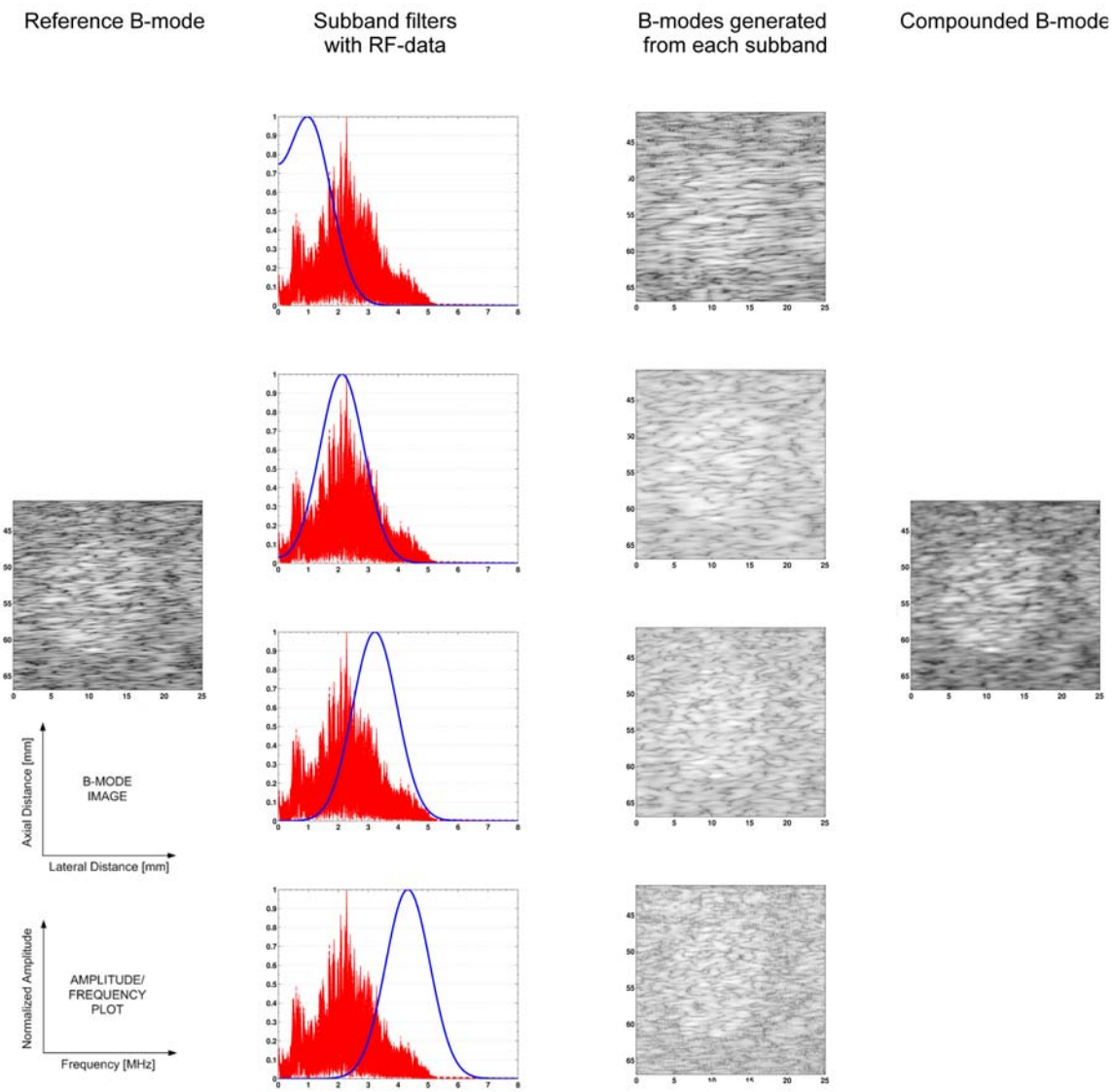

Figure 3.3: The first column shows the B-mode image from the REC reference. The second column shows the partitioning of RF-data with Gaussian subbands. The third column shows the B-mode images with partially uncorrelated speckle patterns. These B-mode images were generated by taking the envelope and log-compressing the RF output from each subband. The final column shows the compounded B-mode image with improved contrast.

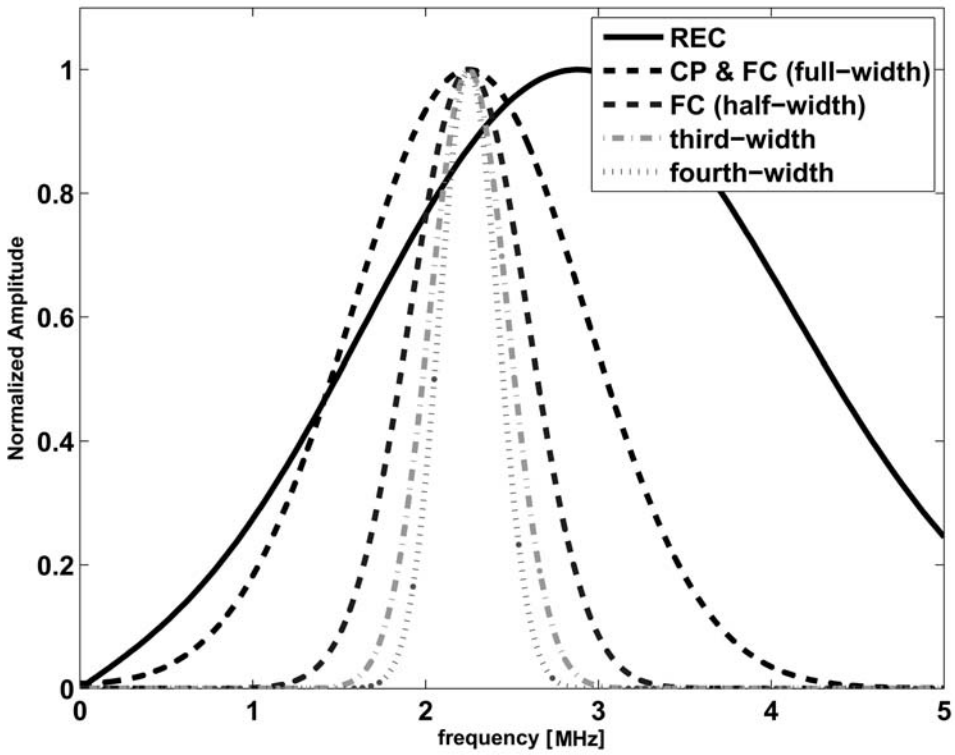

Figure 3.4: Illustration of the bandwidth for all four FC cases applied in conjunction with the bandwidth of the reference signals for CP and REC. Note: REC center frequency was shifted to eliminate any dc-component in the spectrum.

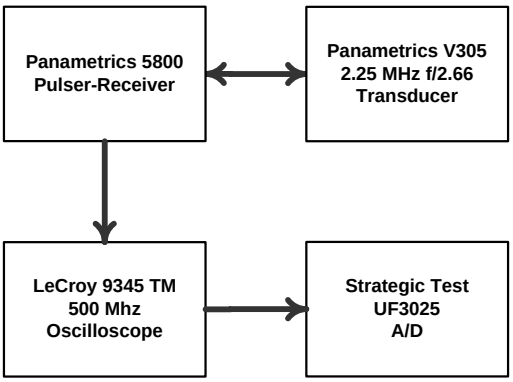

(a)

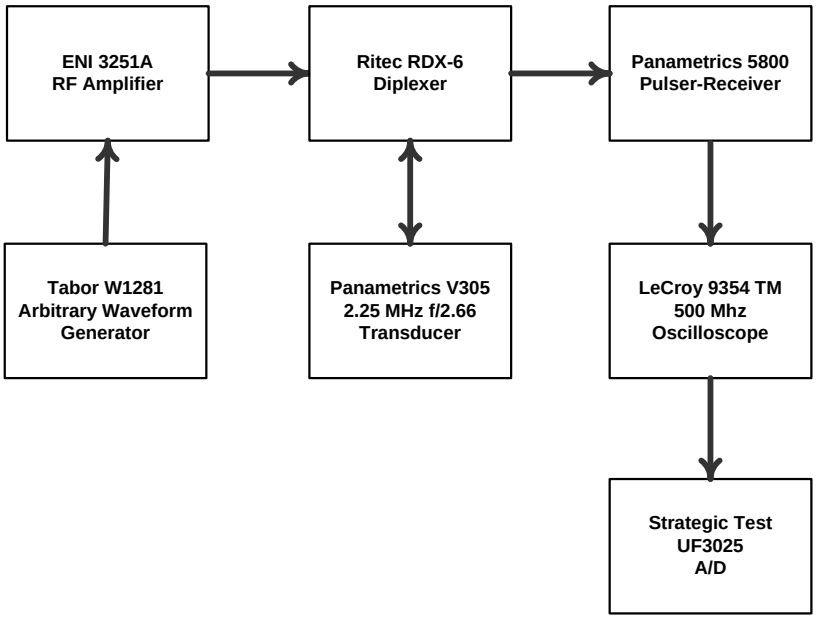

(b)

Figure 3.5: (a) Block diagram of experimental setup for CP, and (b) block diagram of experimental setup for REC.

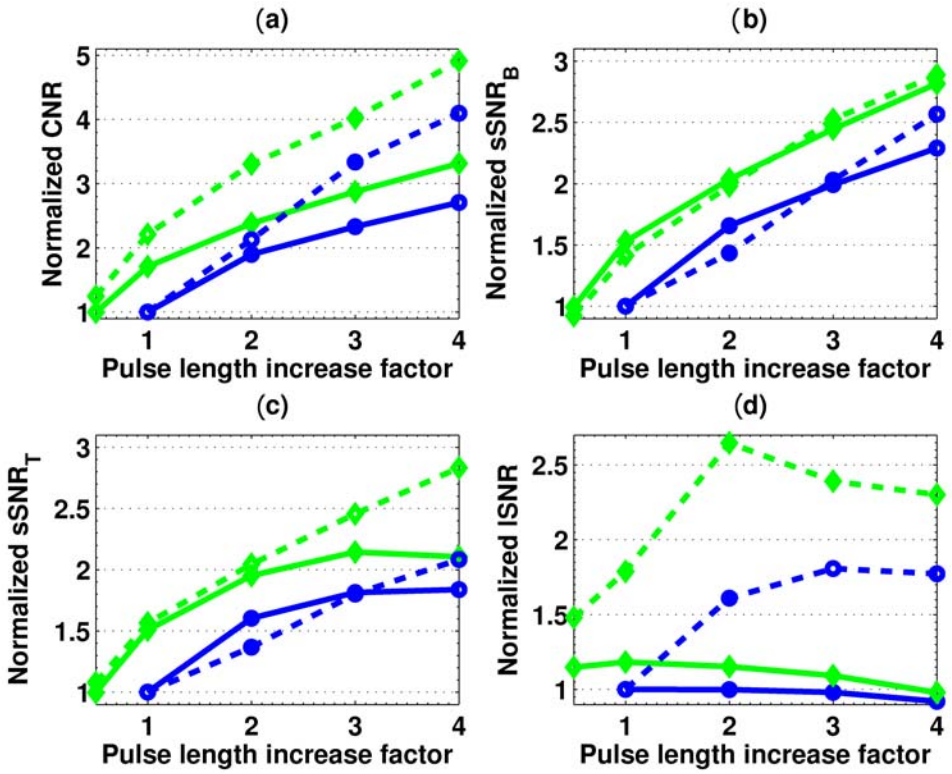

Figure 3.6: (a) Normalized CNR vs. pulse length increase factor, (b) normalized sSNR_B vs. pulse length increase factor, (c) normalized sSNR_T vs. pulse length increase factor, (d) normalized lSNR vs. pulse length increase factor. For simulations and experiments, the quality metric values were normalized to the data corresponding to conventional pulsing with a pulse length increase factor of one. (Simulated results are depicted by a solid line, experimental measurements are shown in a dashed line, REC results are marked by diamonds, and CP results are marked by circles.)

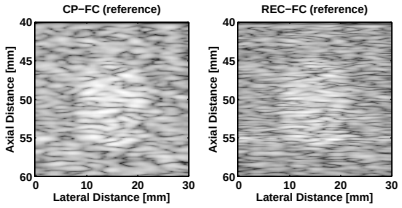

(a)

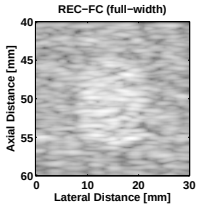

(b)

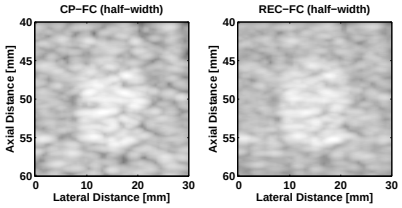

(c)

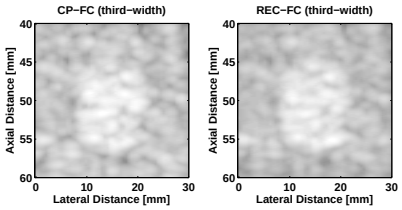

(d)

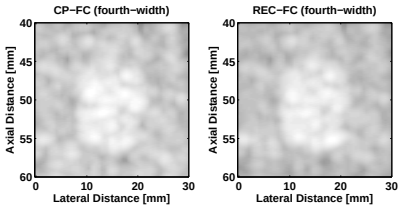

(e)

Figure 3.7: B-mode images of simulated results for: (a) CP and REC reference scans, (b) REC-FC full width case, (c) CP-FC and REC-FC half-width cases, (d) CP-FC and REC-FC third-width cases, and (e) CP-FC and REC-FC fourth-width cases. Image dynamic range = -50 dB.

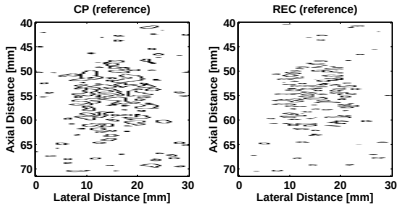

(a)

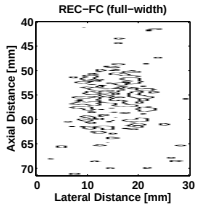

(b)

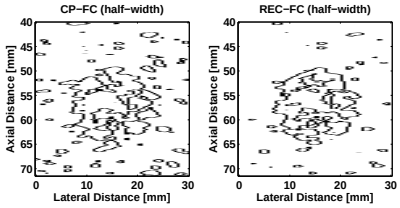

(c)

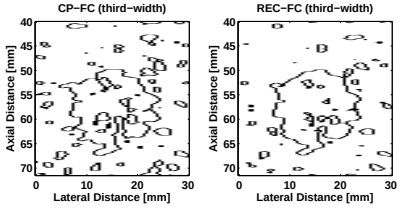

(d)

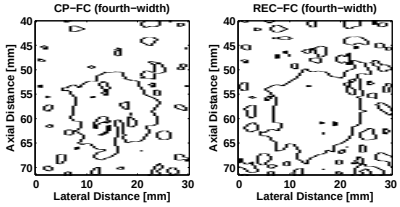

(e)

Figure 3.8: Edge detection images of simulated results using thresholding and margin strength for: (a) CP and REC reference scans, (b) REC-FC full width case, (c) CP-FC and REC-FC half-width cases, (d) CP-FC and REC-FC third-width cases, and (e) CP-FC and REC-FC fourth-width cases.

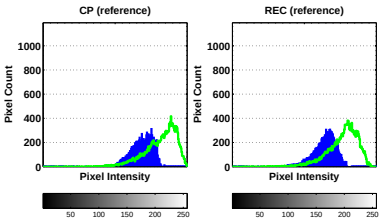

(a)

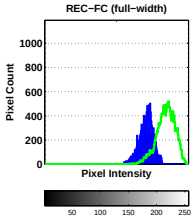

(b)

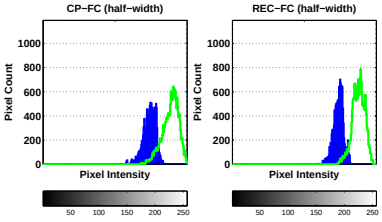

(c)

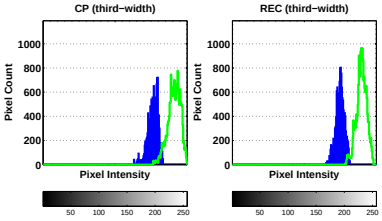

(d)

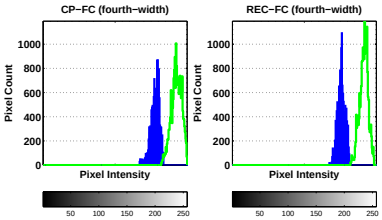

(e)

Figure 3.9: Histograms of simulated results for: (a) CP and REC reference scans, (b) REC-FC full width case, (c) CP-FC and REC-FC half-width cases, (d) CP-FC and REC-FC third-width cases, and (e) CP-FC and REC-FC fourth-width cases. The pixel intensity is represented by the grayscale bar shown underneath the plot. (Color: background region is blue, and target region is green. Grayscale: background region is dark, and target region is light.)

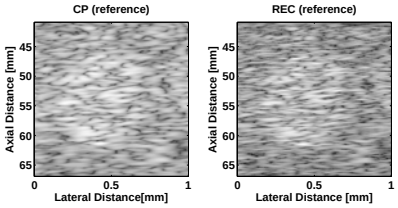

(a)

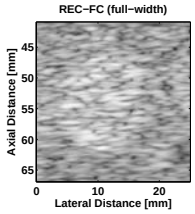

(b)

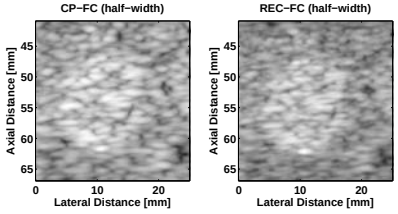

(c)

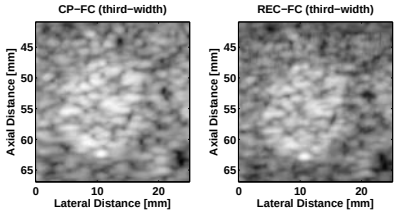

(d)

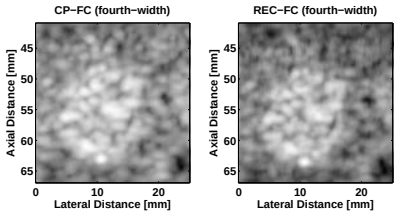

(e)

Figure 3.10: B-mode images of experimental measurements for the ATS +6 dB contrast target: (a) CP and REC reference scans, (b) REC-FC full width case, (c) CP-FC and REC-FC half-width cases, (d) CP-FC and REC-FC third-width cases, and (e) CP-FC and REC-FC fourth-width cases. Image dynamic range = -50 dB.

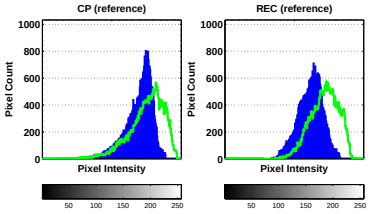

(a)

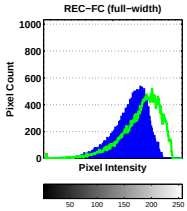

(b)

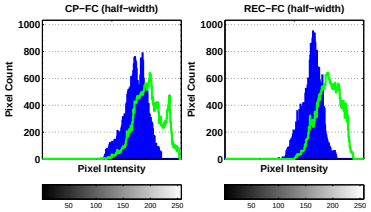

(c)

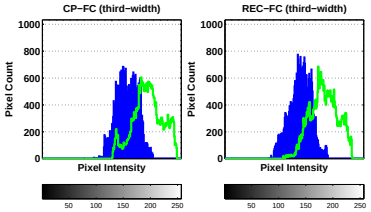

(d)

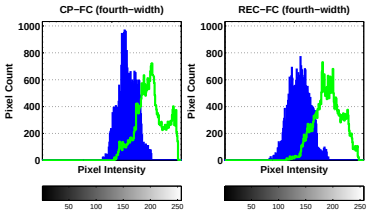

(e)

Figure 3.11: Histograms of experimental measurements for the ATS +6 dB contrast target: (a) CP and REC reference scans, (b) REC-FC full width case, (c) CP-FC and REC-FC half-width cases, (d) CP-FC and REC-FC third-width cases, and (e) CP-FC and REC-FC fourth-width cases. The pixel intensity is represented by the grayscale bar shown underneath the plot. (Color: background region is blue, and target region is green. Grayscale: background region is dark, and target region is light.)

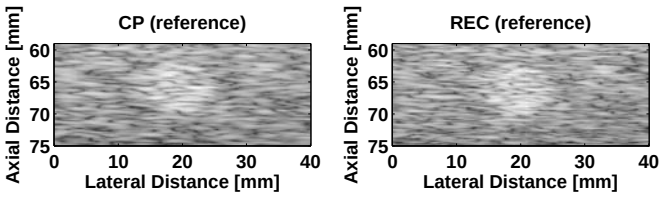

(a)

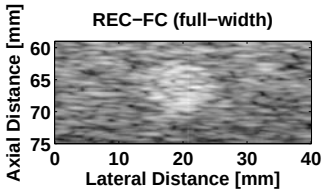

(b)

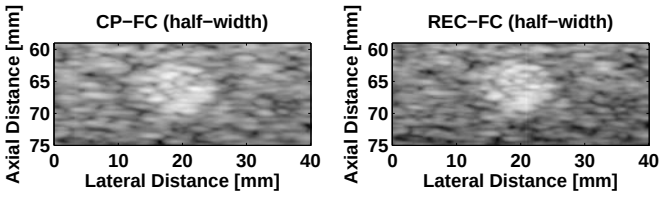

(c)

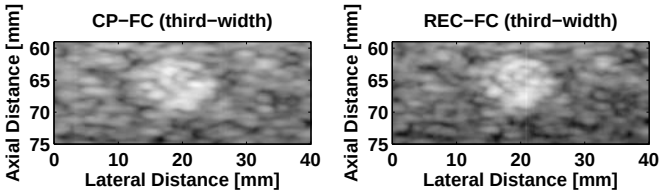

(d)

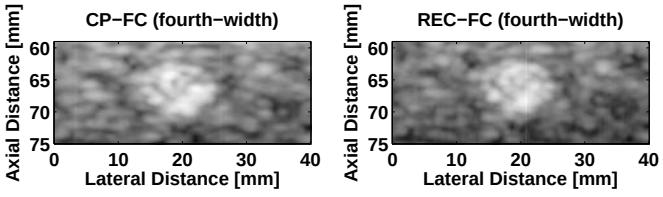

(e)

Figure 3.12: B-mode images of experimental measurements of the hydrogel phantom for a lesion diameter of 8 mm: (a) CP and REC reference scans, (b) REC-FC full width case, (c) CP-FC and REC-FC half-width cases, (d) CP-FC and REC-FC third-width cases, and (e) CP-FC and REC-FC fourth-width cases. Image dynamic range = -50 dB.

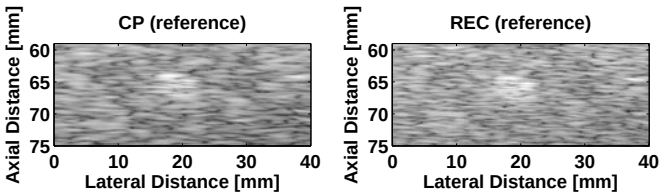

(a)

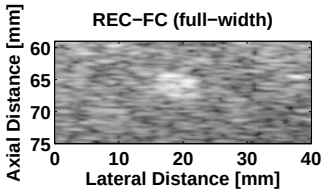

(b)

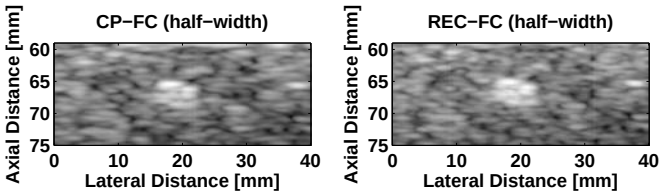

(c)

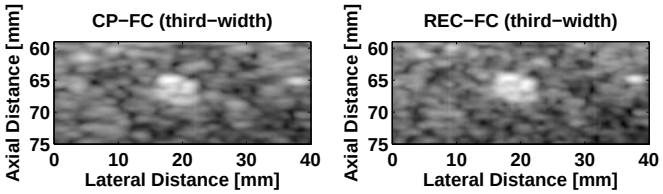

(d)

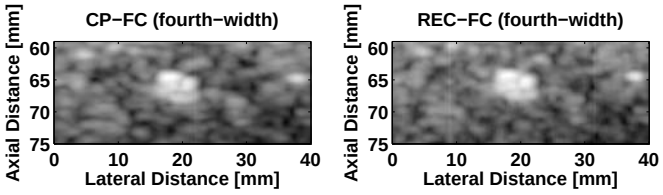

(e)

Figure 3.13: B-mode images of experimental measurements of the hydrogel phantom for a lesion diameter of 5 mm: (a) CP and REC reference scans, (b) REC-FC full width case, (c) CP-FC and REC-FC half-width cases, (d) CP-FC and REC-FC third-width cases, and (e) CP-FC and REC-FC fourth-width cases. Image dynamic range = -50 dB.

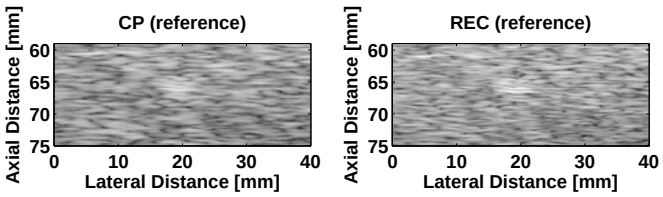

(a)

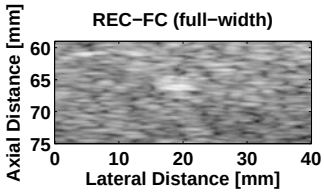

(b)

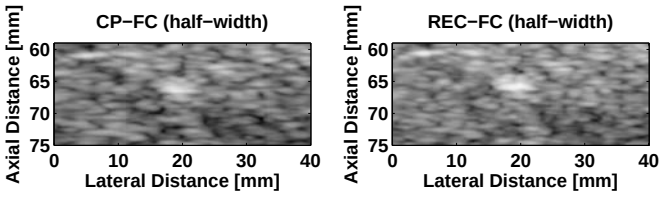

(c)

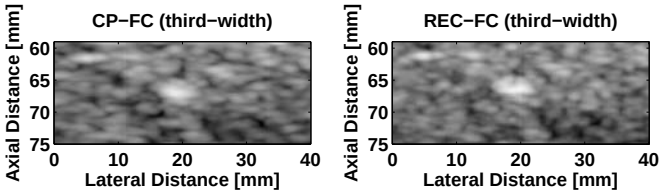

(d)

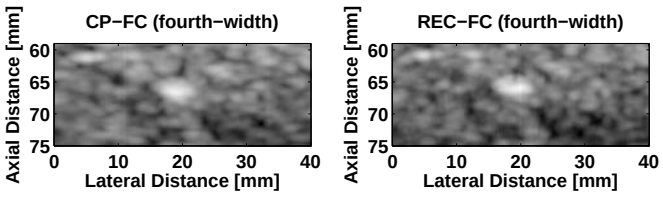

(e)

Figure 3.14: B-mode images of experimental measurements of the hydrogel phantom for a lesion diameter of 3 mm: (a) CP and REC reference scans, (b) REC-FC full width case, (c) CP-FC and REC-FC half-width cases, (d) CP-FC and REC-FC third-width cases, and (e) CP-FC and REC-FC fourth-width cases. Image dynamic range = -50 dB.

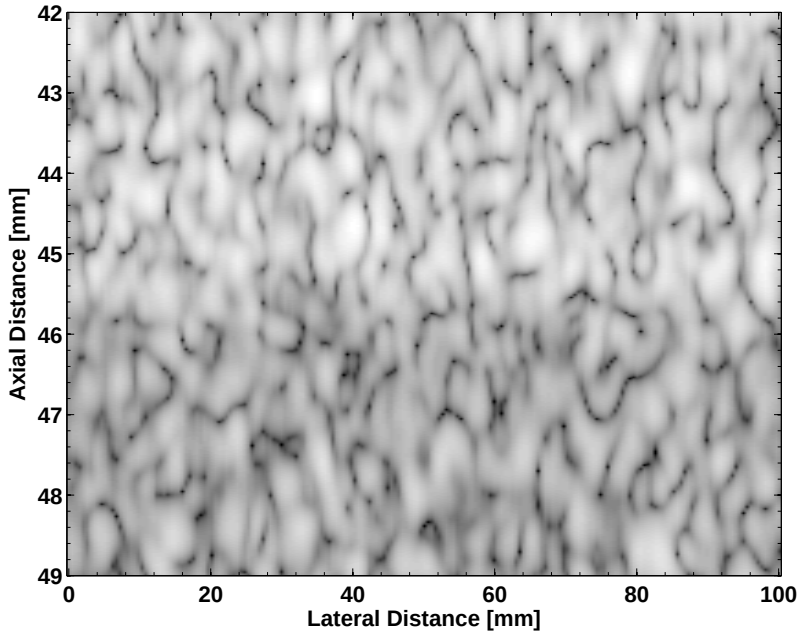

(a)

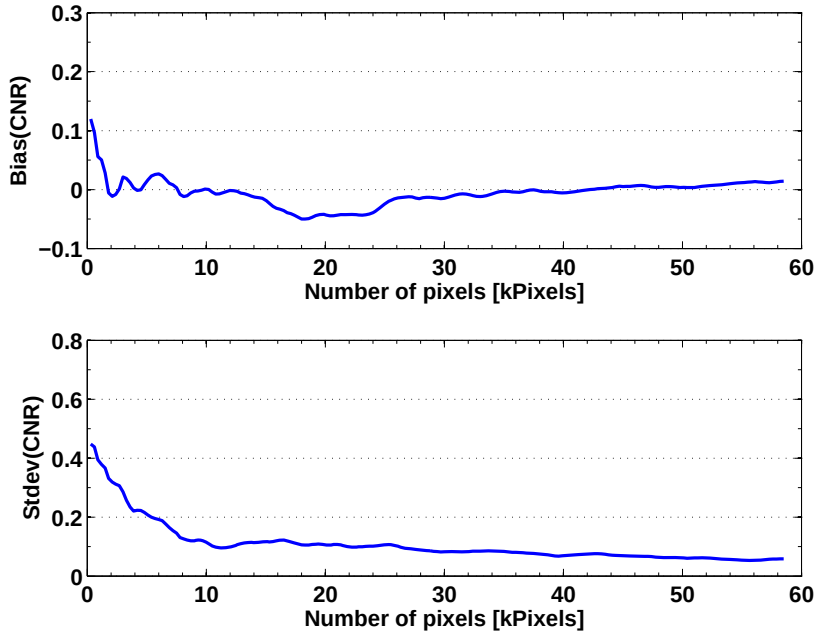

(b)

Figure 3.15: (a) One of 25 phantoms used to evaluate CNR as a function of number of pixels. (b) Bias and standard deviation of CNR as function of number of pixels. Note that the bias was obtained by using the mean of the values in the range of 40 to 58 kilopixels.

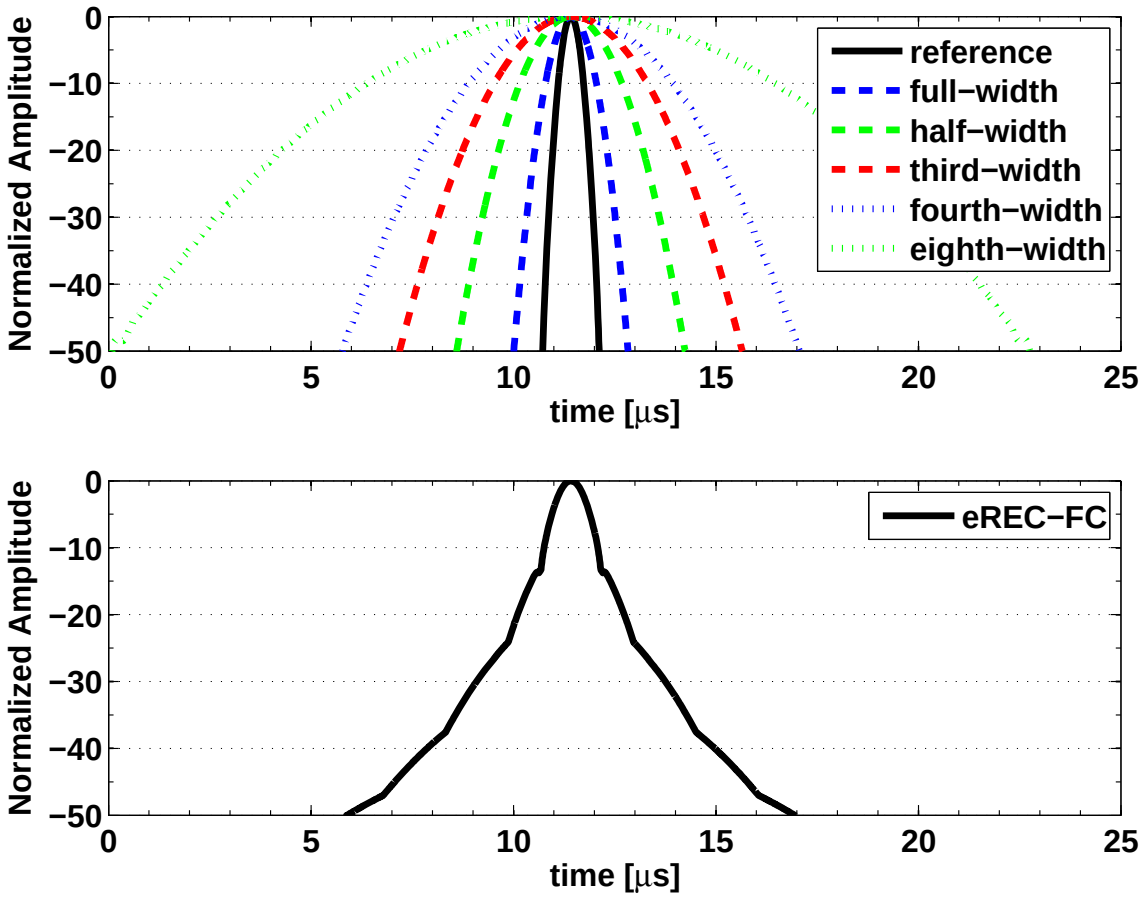

Figure 3.16: (a) Individual envelopes of the different frequency compounded images, and (b) resulting envelope from summing the individual envelopes.

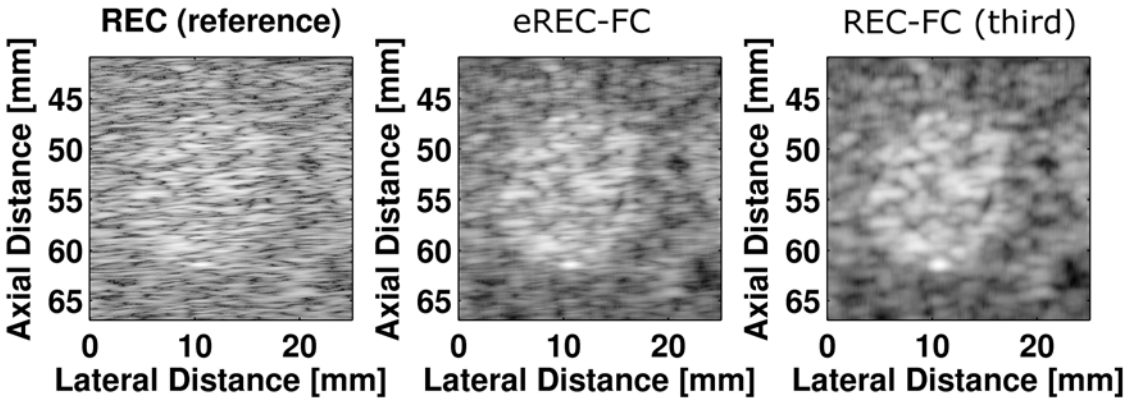

Figure 3.17: B-mode images of experimental measurements of the ATS phantom for a contrast of +6 dB. The left panel represents the reference REC-FC image, the center panel represents the eREC-FC image, and the right panel corresponds to the REC-FC third-width case because it contains similar contrast. Image dynamic range = -50 dB.

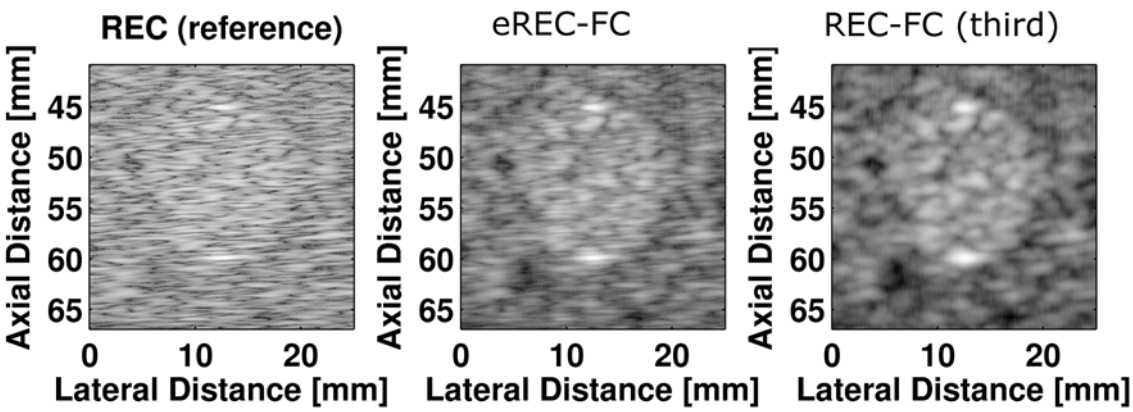

Figure 3.18: B-mode images of experimental measurements of the ATS phantom for a contrast of +3 dB. The left panel represents the reference REC-FC image, the center panel represents the eREC-FC image, and the right panel corresponds to the REC-FC third-width case because it contains similar contrast. Image dynamic range = -50 dB.

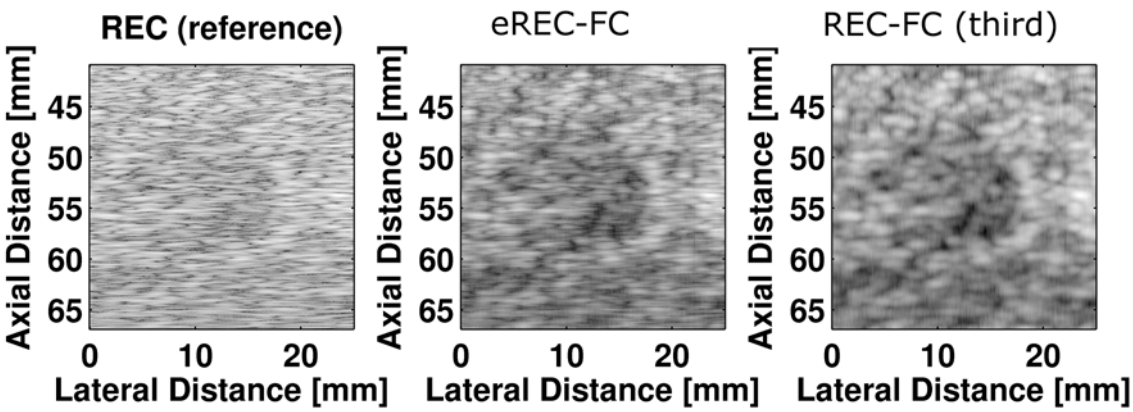

Figure 3.19: B-mode images of experimental measurements of the ATS phantom for a contrast of -3 dB. The left panel represents the reference REC-FC image, the center panel represents the eREC-FC image, and the right panel corresponds to the REC-FC third-width case because it contains similar contrast. Image dynamic range = -50 dB.

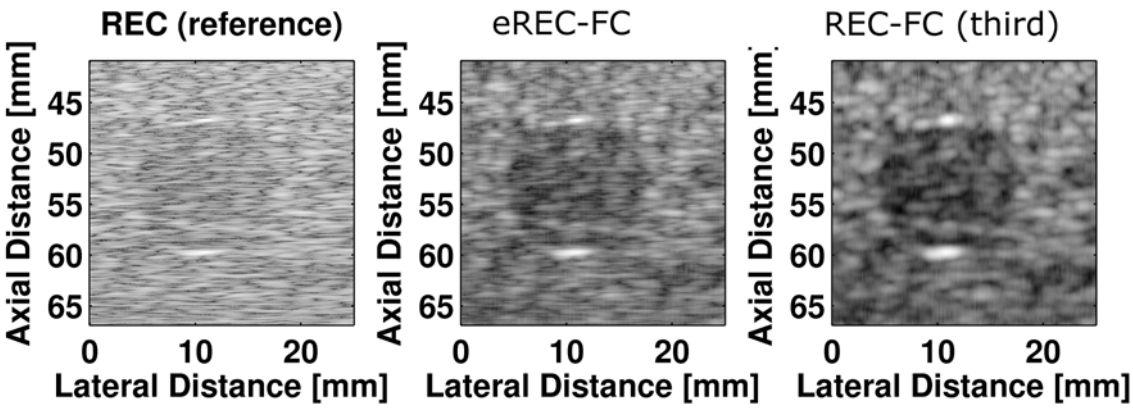

Figure 3.20: B-mode images of experimental measurements of the ATS phantom for a contrast of -6 dB. The left panel represents the reference REC-FC image, the center panel represents the eREC-FC image, and the right panel corresponds to the REC-FC third-width case because it contains similar contrast. Image dynamic range = -50 dB.

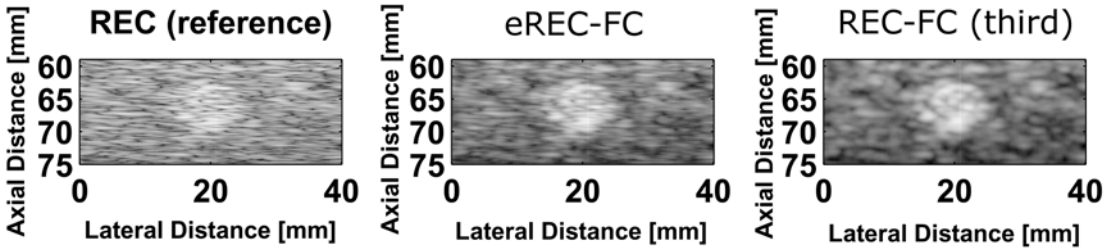

Figure 3.21: B-mode images of experimental measurements of the hydrogel cone phantom for a contrast of +6 dB and a lesion diameter of 8 mm. The left panel represents the reference REC-FC image, the center panel represents the eREC-FC image, and the right panel corresponds to the REC-FC third-width case because it contains similar contrast. Image dynamic range = -50 dB.

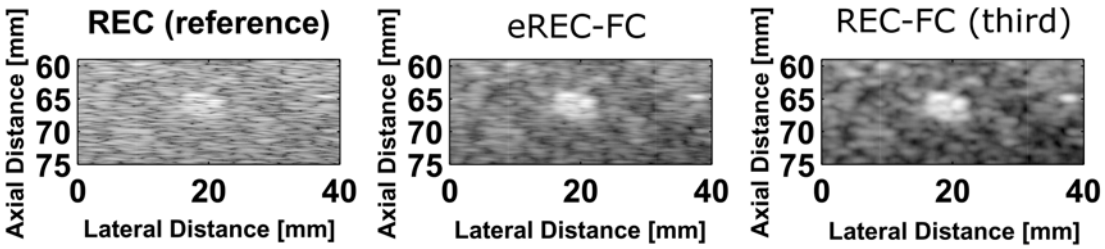

Figure 3.22: B-mode images of experimental measurements of the hydrogel cone phantom for a contrast of +6 dB and a lesion diameter of 5 mm. The left panel represents the reference REC-FC image, the center panel represents the eREC-FC image, and the right panel corresponds to the REC-FC third-width case because it contains similar contrast. Image dynamic range = -50 dB.

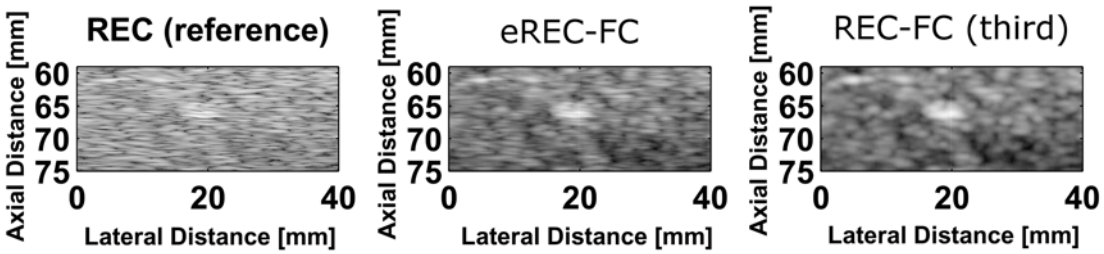

Figure 3.23: B-mode images of experimental measurements of the hydrogel cone phantom for a contrast of +6 dB and a lesion diameter of 3 mm. The left panel represents the reference REC-FC image, the center panel represents the eREC-FC image, and the right panel corresponds to the REC-FC third-width case because it contains similar contrast. Image dynamic range = -50 dB.

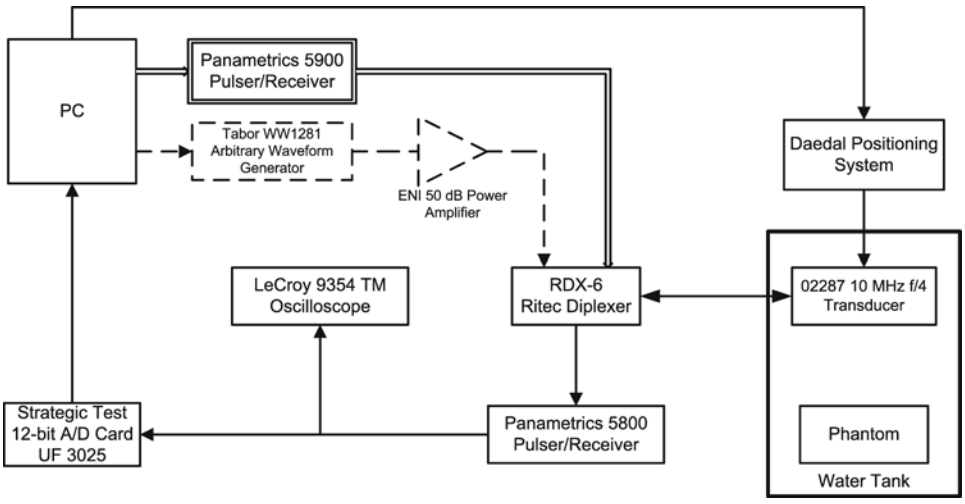

Figure 3.24: Experimental setup used for CP and REC. Note that solid lines indicate components used in both CP and REC experiments, while $\Rightarrow$ indicates a path only taken during CP experiments whereas $\dashrightarrow$ indicates a path only taken during REC experiments.

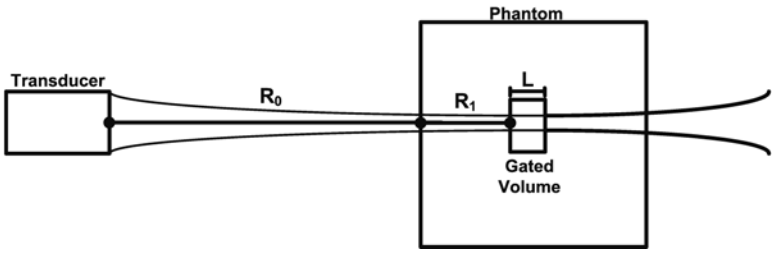

Figure 3.25: Distance relationship between the transducer and phantoms used to obtain measurements. R_0 is the distance from transducer surface to phantom surface, while R_1 is the distance from phantom surface to the start of the gated region of length L. The focal depth is at R0 + R1.

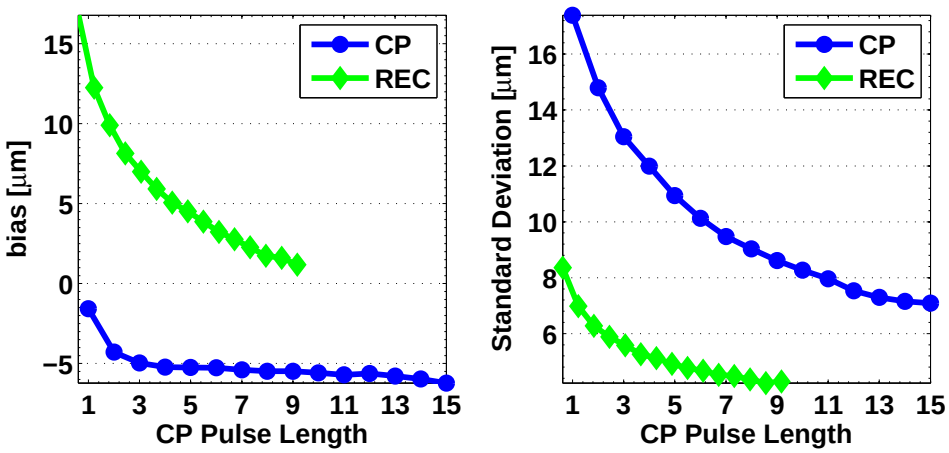

Figure 3.26: (a) Bias and (b) standard deviation of effective scatterer diameter estimates as a function of pulse length for 10 simulations of Phantom S1. Each tick mark on the abscissa is normalized to a CP pulse length of one (0.277 mm). Therefore, one REC pulse length (0.169 mm) would correspond to 0.610 CP pulse length.

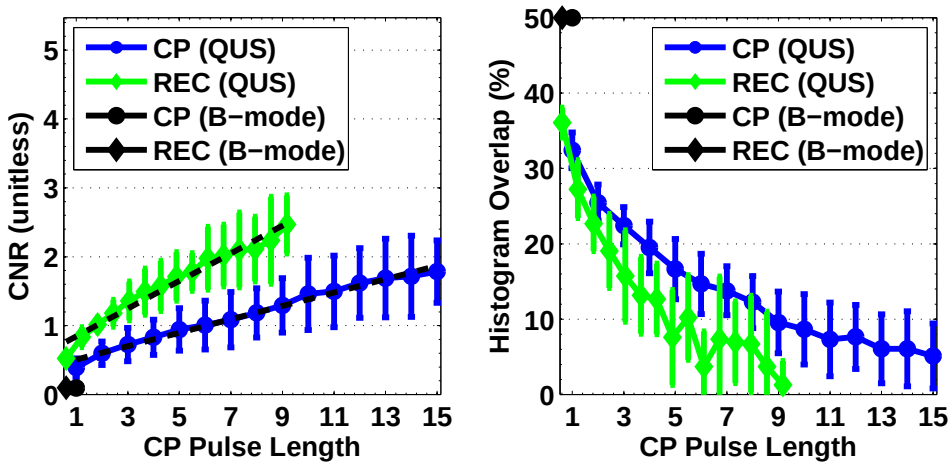

Figure 3.27: CNR and histogram overlap as a function of pulse length from 10 simulations of Phantom S2. Each tick mark on the abscissa is normalized to a CP pulse length of one (0.277 mm). Therefore, one REC pulse length (0.169 mm) would correspond to 0.610 CP pulse length.

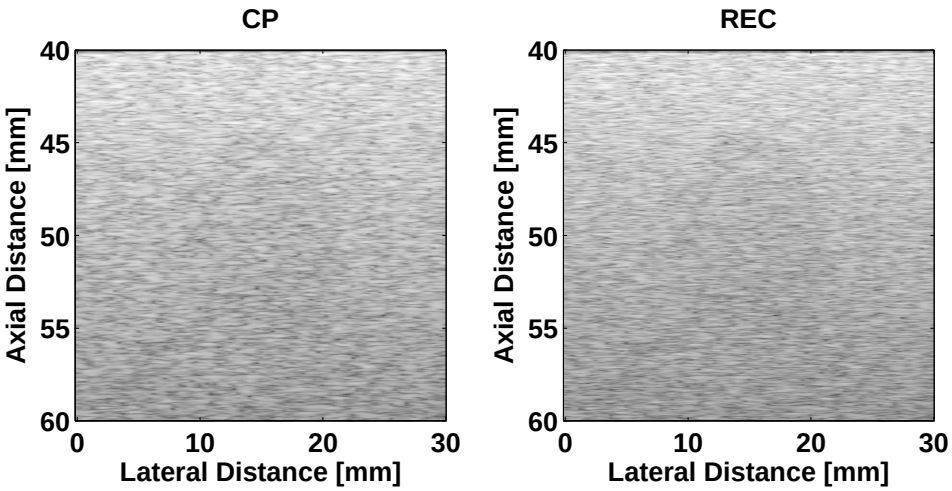

Figure 3.28: B-mode images of phantom S2 for CP and REC.

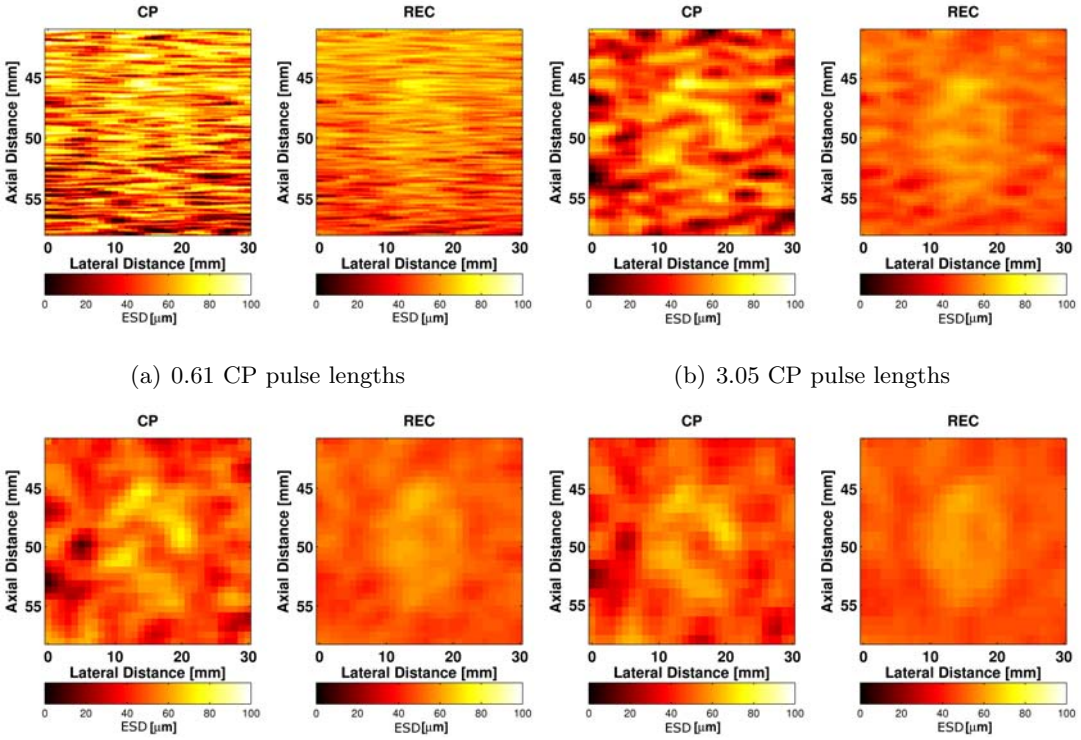

(a) 0.61 CP pulse lengths

(b) 3.05 CP pulse lengths

(c) 6.10 CP pulse lengths

(d) 9.15 CP pulse lengths

Figure 3.29: Parametric images of effective scatterer diameter for phantom S2 for CP and REC for various axial lengths. Actual scatterer diameters for lesion and background region were 60 μm and 50 μm, respectively.

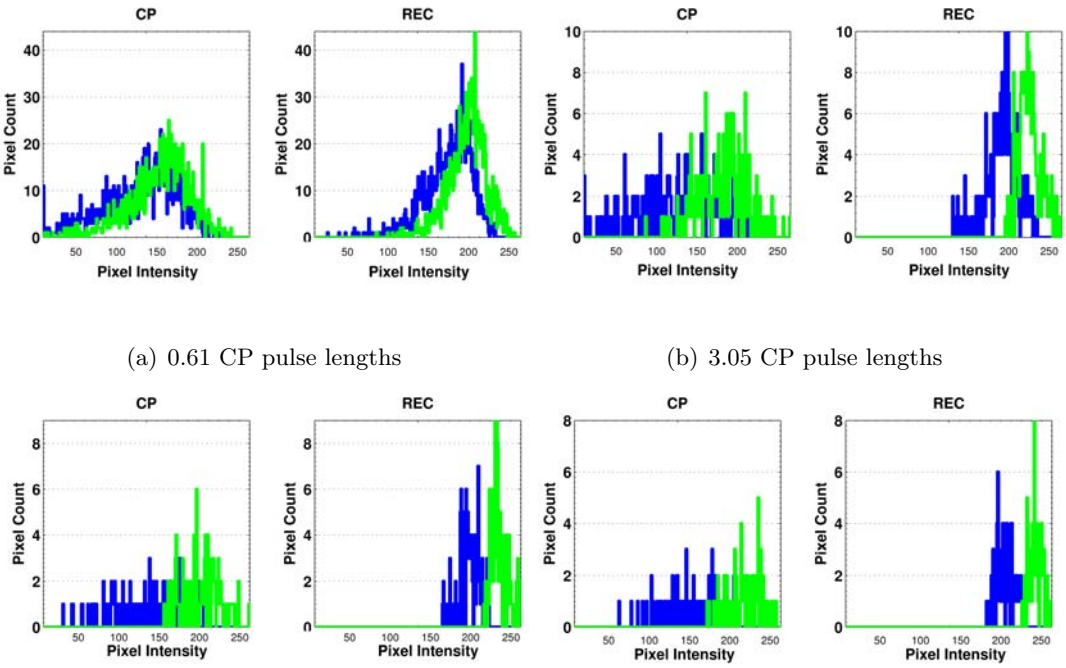

(a) 0.61 CP pulse lengths

(b) 3.05 CP pulse lengths

(c) 6.10 CP pulse lengths

(d) 9.15 CP pulse lengths

Figure 3.30: Histograms of pixel intensity for the background and target regions for phantom S2 for various axial lengths. The pixel intensity is represented by the grayscale colorbar shown underneath the plot. (Color: background region is blue, and target region is green. Grayscale: background region is dark, and target region is light.)

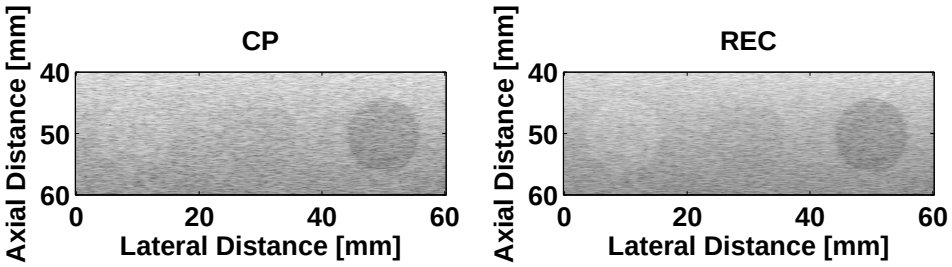

Figure 3.31: B-mode images of phantom S3 for CP and REC.

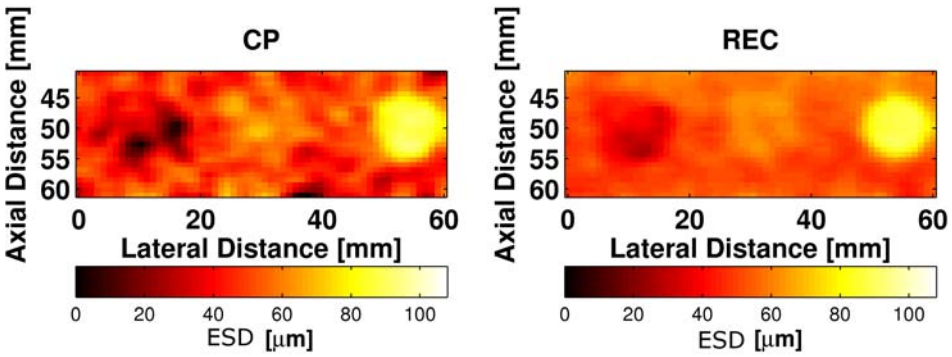

Figure 3.32: Parametric images of ESD for phantom S3 for CP and REC for the recommended axial length of 15 REC pulse lengths. Actual scatterer diameters for the three lesions (in order from left to right) and background region were 30 μm, 60 μm, 90 μm, and 50 μm, respectively.

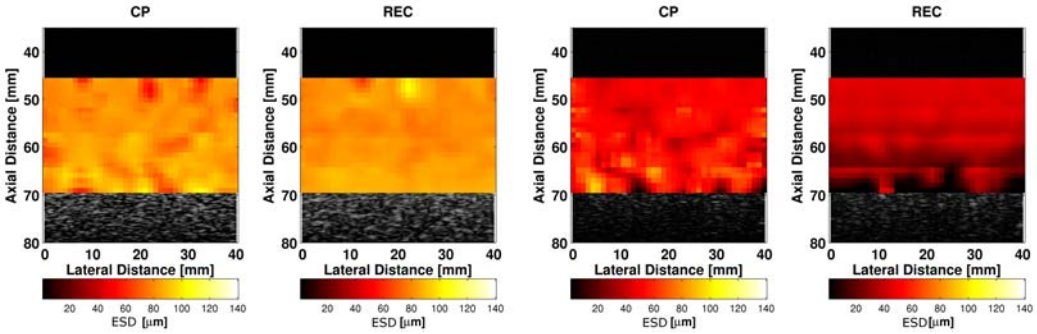

(a) Phantom A

(b) Phantom B

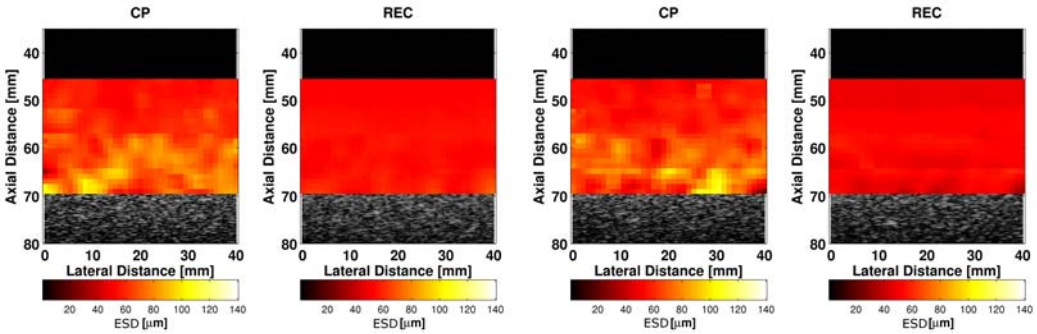

(c) Phantom C

(d) Phantom D

Figure 3.33: B-mode images for CP and REC with a parametric image overlay of ESD.

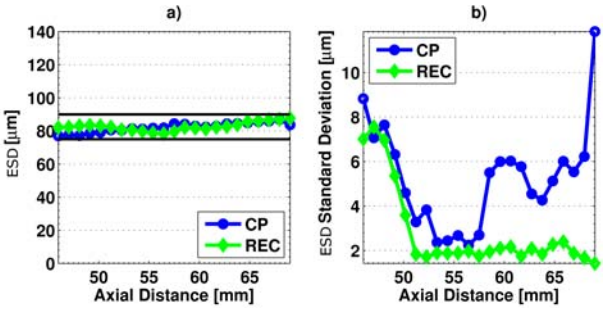

(a) Phantom A

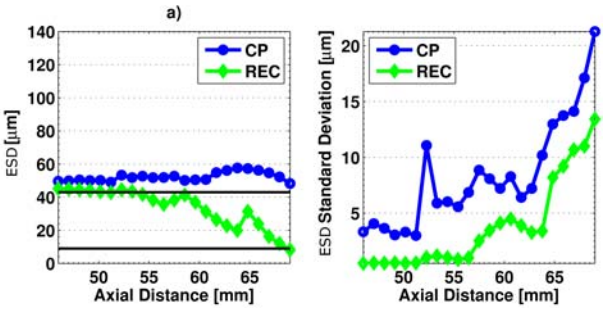

(b) Phantom B

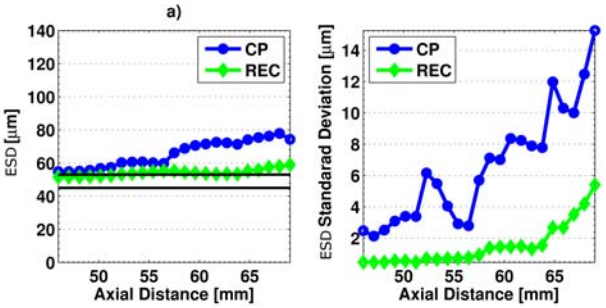

(c) Phantom C

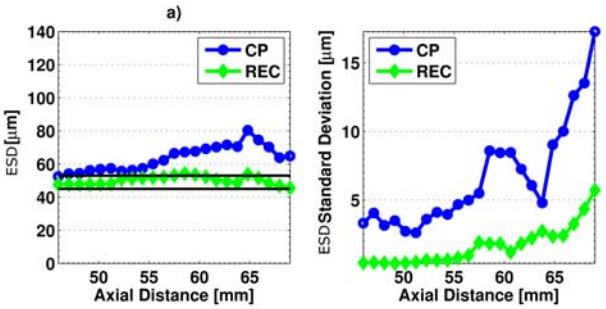

(d) Phantom D

Figure 3.34: ESD and standard deviation of ESD estimates as a function of axial distance. The range of scatterers is indicated by solid lines across as a function of depth.

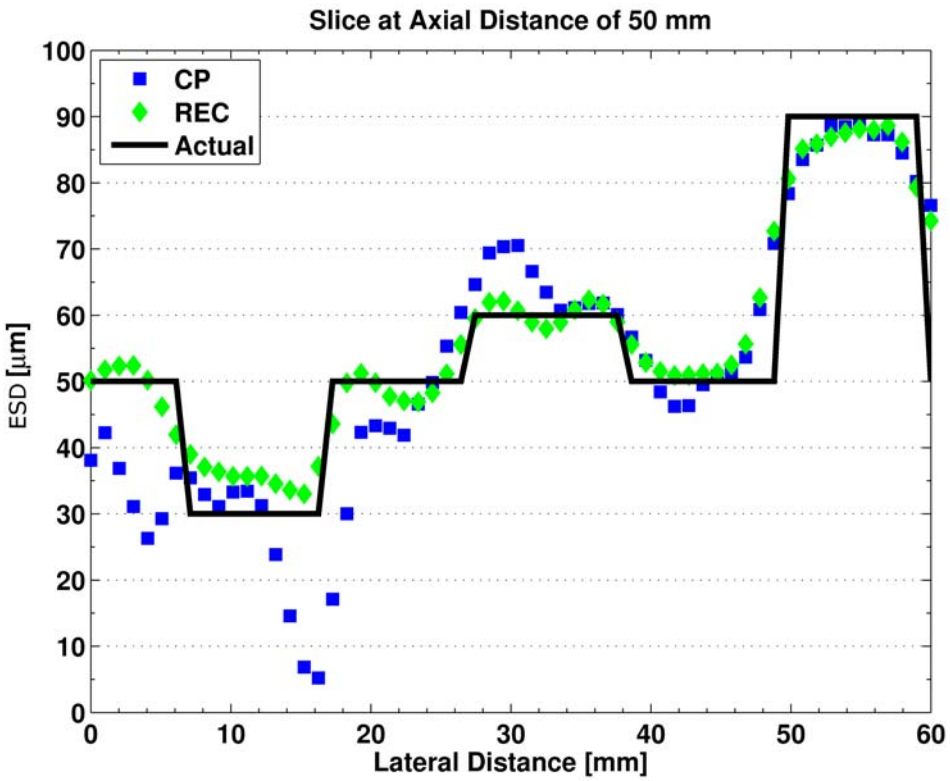

Figure 3.35: A lateral slice of the parametric image of Phantom S3 at an axial distance of 50 mm.

Table 3.1: Filter bank descriptions for the 50 cases of simulated RF data for a 15 mm target.

Technique[a]	Description[b]	Filter Banks		
		Bandwidth (MHz)	Separation (MHz)	Quantity
CP	reference scan	1.1	–	0
REC	reference scan	2.2	–	0
REC-FC	full width of CP BW	1.1	1.3	3
CP-FC	1/2 width of CP BW	0.6	0.6	4
REC-FC	1/2 width of CP BW	0.6	0.6	7
CP-FC	1/3 width of CP BW	0.4	0.4	6
REC-FC	1/3 width of CP BW	0.4	0.4	10
CP-FC	1/4 width of CP BW	0.3	0.3	8
REC-FC	1/4 width of CP BW	0.3	0.3	13

[a] CP = conventional pulsing, REC = resolution enhancement compression, FC = frequency compounding

[b] BW = bandwidth

Table 3.2: Axial and lateral correlation length for the 50 cases of simulated RF data for a 15 mm target.

Technique[a]	Description[b]	Resolution[c] Axial (mm)	Resolution[c] Lateral (mm)
CP	reference scan	0.30 ± 0.03	1.27 ± 0.44
REC	reference scan	0.20 ± 0.01 (33%)	1.37 ± 0.49 (8%)
REC-FC	full width of CP BW	0.44 ± 0.05 (47%)	1.70 ± 0.57 (34%)
CP-FC	1/2 width of CP BW	0.82 ± 0.13 (169%)	1.66 ± 0.65 (31%)
REC-FC	1/2 width of CP BW	0.89 ± 0.16 (194%)	1.78 ± 0.54 (40%)
CP-FC	1/3 width of CP BW	1.17 ± 0.23 (285%)	1.70 ± 0.49 (34%)
REC-FC	1/3 width of CP BW	1.37 ± 0.32 (351%)	1.76 ± 0.50 (39%)
CP-FC	1/4 width of CP BW	1.48 ± 0.29 (386%)	1.70 ± 0.53 (34%)
REC-FC	1/4 width of CP BW	1.77 ± 0.39 (485%)	1.74 ± 0.51 (37%)

[a] CP = conventional pulsing, REC = resolution enhancement compression, FC = frequency compounding

[b] BW = bandwidth

[c] The resolution values in the table are described in terms of the mean plus/minus one standard deviation. Values in parentheses represent the absolute percent change of REC-FC vs. CP reference.

Table 3.3: CNR and sSNR for the 50 cases of simulated RF data for a 15 mm target.

Technique[a]	Description[b]	CNR[c]	$sSNR_B$[c]	$sSNR_T$[c]
CP	reference scan	0.74 ± 0.14	1.94 ± 0.11	1.90 ± 0.11
REC	reference scan	0.74 ± 0.10	1.94 ± 0.10	1.89 ± 0.08
		(0%)	(0%)	(0%)
REC	full width of CP BW	1.27 ± 0.17	2.98 ± 0.24	2.87 ± 0.19
		(71%)	(53%)	(51%)
CP	1/2 width of CP BW	1.41 ± 0.26	3.22 ± 0.33	3.05 ± 0.27
		(89%)	(65%)	(60%)
REC	1/2 width of CP BW	1.77 ± 0.23	3.97 ± 0.36	3.71 ± 0.32
		(137%-25%)	(103%-23%)	(95%-22%)
CP	1/3 width of CP BW	1.73 ± 0.31	3.88 ± 0.49	3.44 ± 0.35
		(133%)	(99%)	(81%)
REC	1/3 width of CP BW	2.14 ± 0.30	4.77 ± 0.60	4.08 ± 0.38
		(187%-24%)	(144%-23%)	(114%-18%)
CP	1/4 width of CP BW	2.01 ± 0.38	4.47 ± 0.64	3.49 ± 0.35
		(170%)	(129%)	(83%)
REC	1/4 width of CP BW	2.46 ± 0.37	5.49 ± 0.77	4.00 ± 0.40
		(231%-22%)	(181%-23%)	(110%-15%))

[a] CP = conventional pulsing, REC = resolution enhancement compression, FC = frequency compounding

[b] BW = bandwidth

[c] The values are described in terms of the mean plus/minus one standard deviation. In parentheses: the absolute percent change of REC-FC vs. CP reference - absolute percent change of REC-FC vs. CP-FC for the same case.

Table 3.4: HPI, HO and lSNR for the 50 cases of simulated RF data for a 15 mm target.

Technique[a]	Description[b]	HPI_B[c]	HPI_T[c]	HO	lSNR[c]
CP	reference scan	169.3 ± 28.1	199.0 ± 28.6	28	15.86 ± 2.80
REC	reference scan	165.3 ± 27.9	194.9 ± 28.4	28	18.21 ± 3.00
		(2%)	(2%)		(15%)
REC	full width of CP BW	181.5 ± 16.3	211.3 ± 16.7	18	18.77 ± 3.62
		(7%)	(6%)		(18%)
CP	1/2 width of CP BW	187.6 ± 14.9	217.7 ± 15.3	16	15.85 ± 3.32
		(11%)	(9%)		(0%)
REC	1/2 width of CP BW	192.1 ± 11.8	222.1 ± 12.1	10	18.29 ± 3.51
		(13%-2%)	(12%-2%)		(15%-15%)
CP	1/3 width of CP BW	194.4 ± 12.1	224.5 ± 12.6	11	15.55 ± 3.06
		(15%)	(13%)		(2%)
REC	1/3 width of CP BW	196.8 ± 10.0	227.6 ± 10.3	6	17.33 ± 3.37
		(16%-1%)	(14%-1%)		(9%-11%)
CP	1/4 width of CP BW	198.8 ± 10.4	228.9 ± 10.8	8	14.60 ± 3.22
		(17%)	(15%)		(8%)
REC	1/4 width of CP BW	198.8 ± 10.4	229.0 ± 18.8	4	15.52 ± 3.16
		(17%-0%)	(15%-0%)		(2%-6%)

[a] CP = conventional pulsing, REC = resolution enhancement compression, FC = frequency compounding

[b] BW = bandwidth

[c] The values are described in terms of the mean plus/minus one standard deviation. In parentheses: absolute percent change of REC-FC vs. CP reference - absolute percent change of REC-FC vs. CP-FC for the same case.

Table 3.5: Filter bank descriptions for the experimental results for the +6 dB, 15 mm diameter target from the ATS phantom and the hydrogel cone phantom.

		Filter Banks		
		Bandwidth	Separation	
Technique[a]	Description[b]	(MHz)	(MHz)	Quantity
CP	reference scan	1.2	–	0
REC	reference scan	2.4	–	0
REC-FC	full width of CP BW	1.2	1.1	4
CP-FC	1/2 width of CP BW	0.6	0.6	3
REC-FC	1/2 width of CP BW	0.6	0.6	6
CP-FC	1/3 width of CP BW	0.4	0.4	6
REC-FC	1/3 width of CP BW	0.4	0.4	10
CP-FC	1/4 width of CP BW	0.3	0.3	10
REC-FC	1/4 width of CP BW	0.3	0.3	15

[a] CP = conventional pulsing, REC = resolution enhancement compression, FC = frequency compounding

[b] BW = bandwidth

Table 3.6: Axial and lateral correlation length for the experimental results for the +6 dB, 15 mm diameter target from the ATS phantom.

Technique[a]	Description[b]	Resolution[c]	
		Axial	Lateral
		(mm)	(mm)
CP	reference scan	0.39	1.2
REC	reference scan	0.21	1.2
		(46%)	(0%)
REC-FC	full width of CP BW	0.37	1.2
		(5%)	(0%)
CP-FC	1/2 width of CP BW	0.68	1.2
		(74%)	(0%)
REC-FC	1/2 width of CP BW	0.45	1.0
		(15%)	(16%)
CP-FC	1/3 width of CP BW	0.80	1.2
		(105%)	(0%)
REC-FC	1/3 width of CP BW	0.65	1.4
		(67%)	(16%)
CP-FC	1/4 width of CP BW	1.25	1.2
		(221%)	(0%)
REC-FC	1/4 width of CP BW	1.34	1.2
		(244%)	(0%)

[a] CP = conventional pulsing, REC = resolution enhancement compression, FC = frequency compounding

[b] BW = bandwidth

[c] Values in parentheses represent the absolute percent change of REC-FC vs. CP reference.

Table 3.7: CNR, and sSNR for the experimental results for the +6 dB, 15 mm diameter target from the ATS phantom.

Technique[a]	Description[b]	CNR[c]	$sSNR_B$[c]	$sSNR_T$[c]
CP	reference scan	0.33	2.09	1.71
REC	reference scan	0.42	1.93	1.84
		(25%)	(7%)	(8%)
REC	full width of CP BW	0.74	2.95	2.68
		(121%)	(41%)	(57%))
CP	1/2 width of CP BW	0.71	2.99	2.34
		(112%)	(43%)	(37%)
REC	1/2 width of CP BW	1.11	4.13	3.49
		(231%-56%)	(98%-38%)	(104%-49%)
CP	1/3 width of CP BW	1.11	4.24	3.08
		(233%)	(102%)	(80%)
REC	1/3 width of CP BW	1.35	5.27	4.20
		(302%-21%)	(152%-24%)	(146%-36%)
CP	1/4 width of CP BW	1.37	5.36	3.56
		(309%)	(156%)	(108%)
REC	1/4 width of CP BW	1.65	6.03	4.84
		(391%-20%)	(189%-13%)	(183%-36%)

[a] CP = conventional pulsing, REC = resolution enhancement compression, FC = frequency compounding

[b] BW = bandwidth

[c] Values in parentheses represent the absolute percent change of REC-FC vs. CP reference.

Table 3.8: HPI, HO and lSNR for the experimental results for the +6 dB, 15 mm diameter target from the ATS phantom.

Technique[a]	Description[b]	HPI_B[c]	HPI_T[c]	HO	lSNR[c]
CP	reference scan	180.0 ± 26.4	193.8 ± 31.5	35	9.9
REC	reference scan	176.8 ± 27.1	193.5 ± 29.6	35	14.6
		(2%)	(0%)		(48%)
REC	full width of CP BW	158.0 ± 22.5	183.1 ± 25.4	33	17.6
		(12%)	(6%)		(78%)
CP	1/2 width of CP BW	174.9 ± 20.0	197.4 ± 24.5	33	15.0
		(3%)	(2%)		(52%)
REC	1/2 width of CP BW	159.8 ± 18.1	190.8 ± 21.3	28	26.1
		(11%-9%)	(2%-3%)		(164%-74%)
CP	1/3 width of CP BW	161.3 ± 18.8	197.0 ± 25.7	28	17.8
		(10%)	(2%)		(80%)
REC	1/3 width of CP BW	139.3 ± 20.0	182.4 ± 25.0	21	23.6
		(23%-14%)	(6%-7%)		(139%-33%)
CP	1/4 width of CP BW	157.6 ± 16.9	199.5 ± 25.5	25	17.5
		(12%)	(3%)		(78%)
REC	1/4 width of CP BW	138.5 ± 19.6	190.4 ± 24.8	19	22.7
		(23%-12%)	(2%-5%)		(130%-30%)

[a] CP = conventional pulsing, REC = resolution enhancement compression, FC = frequency compounding

[b] BW = bandwidth

[c] Values in parentheses represent the absolute percent change of REC-FC vs. CP reference.

Table 3.9: CNR experimental results for the +6 dB hydrogel phantom at various diameters.

Technique[a]	Description[b]	Lesion Diameter[c]		
		8 mm	5 mm	3 mm
CP	reference scan	0.82	1.22	1.40
REC	reference scan	0.95	1.23	1.66
		(16%)	(1%)	(19%)
REC	full width of CP BW	1.53	2.50	3.65
		(87%)	(105%)	(161%)
CP	1/2 width of CP BW	1.68	4.09	4.24
		(104%)	(235%)	(202%)
REC	1/2 width of CP BW	2.14	4.40	2.42
		(161%-27%)	(261%-8%)	(73%-42%)
CP	1/3 width of CP BW	1.99	3.90	3.56
		(142%)	(219%)	(154%)
REC	1/3 width of CP BW	2.58	5.56	5.41
		(283%-30%)	(355%-43%)	(301%-52%)
CP	1/4 width of CP BW	2.01	4.34	7.44
		(145%)	(255%)	(431%)
REC	1/4 width of CP BW	3.00	7.22	5.00
		(265%-50%)	(491%-66%)	(257%-48%)

[a] CP = conventional pulsing, REC = resolution enhancement compression, FC = frequency compounding

[b] BW = bandwidth

[c] In parentheses: absolute percent change of REC-FC vs. CP reference - absolute percent change of REC-FC vs. CP-FC for the same case.

Table 3.10: $sSNR_B$ experimental results for the +6 dB hydrogel phantom at various diameters.

Technique[a]	Description[b]	Lesion Diameter[c] 8 mm	5 mm	3 mm
CP	reference scan	1.56	1.79	2.01
REC	reference scan	1.66	2.31	2.06
		(6%)	(29%)	(3%)
REC	full width of CP BW	2.33	2.87	3.47
		(49%)	(60%)	(72%)
CP	1/2 width of CP BW	2.08	3.51	2.38
		(33%)	(96%)	(18%)
REC	1/2 width of CP BW	2.81	4.46	3.04
		(80%-27%)	(149%-27%)	(51%-27%)
CP	1/3 width of CP BW	2.78	5.73	2.85
		(78%)	(220%)	(41%)
REC	1/3 width of CP BW	3.81	2.07	4.82
		(144%-37%)	(15%-33%)	(139%-69%)
CP	1/4 width of CP BW	2.65	3.87	6.88
		(70%)	(48%)	(242%)
REC	1/4 width of CP BW	4.35	1.98	7.48
		(179%-64%)	(11%-48%)	(272%-8%)

[a] CP = conventional pulsing, REC = resolution enhancement compression, FC = frequency compounding

[b] BW = bandwidth

[c] In parentheses: absolute percent change of REC-FC vs. CP reference - absolute percent change of REC-FC vs. CP-FC for the same case.

Table 3.11: $sSNR_T$ experimental results for the +6 dB hydrogel phantom at various diameters.

Technique[a]	Description[b]	Lesion Diameter[c] 8 mm	5 mm	3 mm
CP	reference scan	2.10	2.05	2.36
REC	reference scan	2.16	2.86	1.77
		(3%)	(40%)	(25%)
REC	full width of CP BW	3.17	4.26	6.41
		(51%)	(108%)	(172%)
CP	1/2 width of CP BW	3.99	3.26	9.23
		(90%)	(59%)	(291%)
REC	1/2 width of CP BW	5.25	4.22	6.25
		(150%-17%)	(106%-1%)	(165%-32%)
CP	1/3 width of CP BW	4.50	4.28	3.33
		(114%)	(108%)	(41%)
REC	1/3 width of CP BW	6.71	3.99	7.79
		(220%-49%)	(95%-7%)	(230%-134%)
CP	1/4 width of CP BW	4.43	4.64	5.33
		(110%)	(126%)	(126%)
REC	1/4 width of CP BW	8.51	2.42	4.77
		(305%-92%)	(18%-47%)	(102%-11%)

[a] CP = conventional pulsing, REC = resolution enhancement compression, FC = frequency compounding

[b] BW = bandwidth

[c] In parentheses: absolute percent change of REC-FC vs. CP reference - absolute percent change of REC-FC vs. CP-FC for the same case.

Table 3.12: CNR results for the eREC-FC B-mode images and for the REC reference B-mode images.

	CNR	
Phantom Description	REC (reference)	eREC-FC
ATS +6 dB	0.42	1.01
ATS +3 dB	0.46	1.04
ATS -3 dB	0.74	1.36
ATS -6 dB	0.44	1.24
Hydrogel 8 mm	0.95	2.40
Hydrogel 5 mm	1.23	3.03
Hydrogel 3 mm	1.66	3.27

Table 3.13: Simulated Phantom (S1 and S2) properties.

Property	Phantom		
	S1	S2	
		lesion	background
Phantom Dimensions - length, width, height (mm)	20 x 30 x 1.2	20 x 30 x 1.2	
Scatterer Type	Gaussian	Gaussian	Gaussian
Scatterer Diameter (μm)	50	60	50
Lesion Diameter (mm)	-	12	-
Nominal sound speed (m/s)	1540	1540	1540
Nominal Attenuation (dB/(MHz cm))	0.5	0.5	0.5
CP: ka (10 MHz @ -6 dB)	0.61 - 1.42	0.73 - 1.71	0.61 - 1.42
REC: ka (10 MHz @ -6 dB)	0.26 - 1.79	0.30 - 2.14	0.26 - 1.79

Table 3.14: Simulated Phantoms (S3) properties.

Property	Phantom S3			
	lesion 1	lesion 2	lesion 3	background
Phantom Dimensions - l,w,h (mm)	20 x 30 x 1.2			
Scatterer Type	Gaussian	Gaussian	Gaussian	Gaussian
Scatterer Diameter (μm)	30	60	90	-
Lesion Diameter (mm)	12	12	12	-
Nominal sound speed (m/s)	1540	1540	1540	1540
Nominal Attenuation (dB/(MHz cm))	0.5	0.5	0.5	0.5
CP: ka (10 MHz @ -6 dB)	0.37 - 0.85	0.73 - 1.71	1.46 - 3.42	
REC: ka (10 MHz @ -6 dB)	0.15 - 1.07	0.30 - 2.14	0.60 - 4.28	

Table 3.15: Experimental Phantom properties: Part I.

	Phantom	
Property	A	B
Scatterer	Glass spheres	Glass spheres
Materials	Agarose/n-propanol/ milk/H_20	Agarose/n-propanol milk/H_20
Scatterer diameter (μm)	75 - 90	9 - 43
Nominal sound speed (m/s)	1540	1540
Nominal Attenuation (dB/(MHz cm))	0.5	0.7
CP: ka (10 MHz @ -6 dB)	1.70 - 4.37	0.20 - 2.19
REC: ka (10 MHz @ -6 dB)	0.97 - 6.04	0.12 - 3.02

Table 3.16: Experimental Phantom properties: Part II.

	Phantom	
Property	C	D
Scatterer	Glass spheres	Glass spheres
Materials	Agarose/n-propanol/ graphite/H_20	Agarose/n-propanol/ graphite/H_20
Scatterer diameter (μm)	45 - 53	45 - 53
Nominal sound speed (m/s)	1540	1540
Nominal Attenuation (dB/(MHz cm))	0.5	0.7
CP: ka (10 MHz @ -6 dB)	1.02 - 2.58	1.02 - 2.58
REC: ka (10 MHz @ -6 dB)	0.58 - 3.56	0.58 - 3.56

Table 3.17: Bias ± one standard deviation results for QUS images of 10 S2 phantoms using ROIs with different axial sizes in terms of CP pulse lengths.

CP Pulse Lengths	bias μm			
	CP		REC	
	lesion	background	lesion	background
0.61	-0.10 ± 15.59	2.46 ± 18.30	7.69 ± 5.85	17.69 ± 6.60
3.05	-2.23 ± 9.69	-3.78 ± 12.97	-2.11 ± 3.35	7.88 ± 4.08
6.10	-2.07 ± 6.78	-3.85 ± 9.52	-5.44 ± 2.56	4.55 ± 3.17
9.15	-2.01 ± 5.41	-3.77 ± 6.89	-7.28 ± 2.08	2.71 ± 2.66

Table 3.18: Histogram overlap, and CNR ± one standard deviation results for QUS images of 10 S2 phantoms uisng ROIs with different axial sizes in terms of CP pulse lengths.

	histogram overlap %		CNR unitless	
CP Pulse Lengths	CP lesion	REC background	CP lesion	REC background
0.61	36.70 ± 1.36	36.08 ± 1.99	0.31 ± 0.09	0.52 ± 0.07
3.05	21.70 ± 3.29	15.72 ± 6.08	0.72 ± 0.23	1.36 ± 0.28
6.10	13.75 ± 4.30	3.71 ± 4.66	1.02 ± 0.36	1.98 ± 0.45
9.15	9.14 ± 4.28	1.27 ± 3.18	1.36 ± 0.46	2.47 ± 0.42

Table 3.19: CNR and standard deviation results for Phantoms S3 at a recommended axial length of 15 REC pulse length.

	CNR		ESD Standard Deviation	
	unitless		μm	
Scatterer Diameter	CP	REC	CP	REC
30	2.28	3.31	8.56	4.04
60	1.45	3.66	4.78	1.51
90	6.67	16.80	1.71	1.05

Table 3.20: Experimental results of out of range, ESD, and standard deviation of ESD estimates for all depths (axial distance) combined for the physical phantoms.

	Out of range		ESD		Standard deviation(ESD)	
	%		μm		μm	
phantom	CP	REC	CP	REC	CP	REC
A	17.9	4.4	83.0	82.6	6.4	4.2
B	87.2	37.9	52.4	33.8	9.6	10.9
C	93.4	61.3	65.6	54.1	10.8	2.7
D	87.2	20.5	63.6	50.1	10.9	3.2

CHAPTER 4

EVALUATION OF THE COMPRESSION PERFORMANCE OF REC ECHOES USING A SPATIALLY VARYING WIENER FILTER

4.1 Introduction

The focus of the chapter is to evaluate techniques that improve the image quality using a coding and pulse compression technique by either reducing the sidelobe levels, improving spatial resolution, or increasing the signal-to-noise ratio beyond what is available when using a Wiener filter. The techniques evaluated in this chapter were applied directly to the REC technique but could also be applied to general techniques involving coded excitation and pulse compression. In previous chapters, compression was based on the simplification that the spatially varying nature of the echo signals was negligible. Under this simplification, the Wiener filter used for compression did not include a spatially varying response. However, it was hypothesized that a Wiener filter containing adaptive variables based on the spatial location of the region being evaluated would lead to improved image quality. Simulations and experiments were conducted to test the hypothesis.

This chapter is subdivided into two sections, with each section evaluating a different variable being adjusted in the Wiener filter. The first section will evaluate the effects on the compression when the adjustable parameter in the Wiener filter is the linear chirp that depends on the spatially varying pulse-echo impulse response. The second section will evaluate the effects on the compression when the adjustable parameter is the spatially varying echo-signal-to-noise ratio.

4.2 Spatially Varying Wiener Filter with a Spatially Varying Linear Chirp Parameter

In the original design of the pre-enhanced chirp, the overall system impulse response was approximated by the impulse response of the source measured at the focus. In other words, a non-spatially-varying impulse response of the transducer was assumed. When imaging targets that were not located at the focus, a mismatch between the transmitted signal that had been optimized for the focus and the received echo could occur. Therefore, because of the assumption that the impulse response did not vary spatially, the compression performance away from the focus was hindered because sidelobe levels were observed to increase and a loss of axial resolution occurred.

In this subsection, the effects of the spatially varying nature of the impulse response were evaluated. In addition, techniques to compensate for the spatial impulse response in the compression scheme (Wiener filter) were examined. The overall objective was to remove any system dependencies in order to make all compressed echoes throughout the depth of field behave as if they were imaged at the focus of the source.

4.2.1 Spatial impulse response

In ultrasound, the overall system response can be described symbolically as follows:

$$g(x,y,z,t) = e(t) * emir_t(t) * sir_t(x,y,z,t) * sir_r(x,y,z,t) * emir_r(t) \tag{4.1}$$

where t is the range time; x, y, and z are the spatial coordinates; $g(x,y,z,t)$ is the echo waveform; $e(t)$ is the excitation signal; $emir_t(t)$ and $emir_r(t)$ are the transmit and receive electromechanical impulse responses of the transducer; and $sir_t(x,y,z,t)$ and $sir_r(x,y,z,t)$ are the transmit and receive spatial impulse responses. The spatial impulse response is defined as the pressure wave radiated from a point at some location in space resulting from the velocity of the aperture [102–104]. The spatial impulse response [103] is described by the following expression:

$$sir(x,y,z,t) = \int_\sigma \frac{\delta(t - \frac{|\vec{r}-\vec{r_0}|}{c})}{2\pi|\vec{r}-\vec{r_0}|} dS, \tag{4.2}$$

where t is time, $\vec{r}_0$ is the position on the source (Fig. 4.1), $\vec{r}$ is the position of the field point of interest, σ is the area of the source, and S the surface of the source.

The expression in (4.2) uses the Rayleigh integral, which is valid for a piston source. However, for a weakly-focused source the Rayleigh integral is still valid and provides an excellent approximation [105–107]. Therefore, at the focal point of a focused transducer the pressure waves from all the points on the transducer surface arrive at approximately the same time and as a result the spatial impulse response is represented by a δ-function in time. This is shown in the Field II simulation [108, 109] in Fig.4.2. Field II is a software package that can be used in conjunction with MATLAB to simulate ultrasound transducer fields and to perform imaging of phantoms. Field II uses the concept of the spatial impulse response as described by Tupholme-Stepanishen [102–104] to calculate linear fields. Therefore, the symbolic expression in (4.1) at the focus reduces to

$$g(x, y, z, t) = e(t) * emir_t(t) * emir_r(t). \tag{4.3}$$

The spatial impulse response before (Fig. 4.3) and after (Fig. 4.4) the focus behaves like a low-pass filter, although the spatial impulse response changes more slowly after the focus.

In the development of the REC technique, the compression was achieved throughout the depth of field of a source by assuming the spatial impulse response was constant or non-spatially-varying. The pre-enhanced chirp was obtained by convolution equivalence [18] as follows:

$$V_{pre}(f) = V_{lin}(f) \times \frac{H_2(f)}{H_1(f)}. \tag{4.4}$$

The pre-enhanced chirp as constructed in (4.4) was optimized for imaging targets at the focus of the source. As the target moves away from the focus, in either direction, the spatial impulse response is no longer a δ-function, which changes the characteristics of the echo and as a result deteriorates the quality of the compression due to this mismatch. To prevent a mismatch, the pre-enhanced chirp could be designed for each spatial location as follows:

$$V_{pre}(f, x) = V_{lin}(f, x) \times \frac{H_2(f, x)}{H_1(f, x)}. \tag{4.5}$$

However, while such a solution is feasible, the tradeoff is that multiple excitations would reduce the imaging frame rate. In certain applications this is not desirable. An alternative would be to compensate for these spatially varying changes in the compression or the receive stage rather than in the transmission of the excitation signal. In this scenario H_2 is kept constant throughout x.

In the compression of REC echoes, a modified linear chirp, $V_{lin}^{'}(f)$, is generated in order to restore convolution equivalence and obtain a better match between the MATLAB generated linear chirp, $V_{lin}(f)$, and the actual received echo. Previously, $V_{lin}^{'}(f)$ was generated by the expression in (1.3). However, to compensate for the spatially varying nature of the impulse response, (1.3) was modified as follows:

$$V_{lin}^{'}(f,x) = \frac{H_2^*(f)}{|H_2(f)|^2 + |H_2(f)|^{-2}} \cdot H_{out}(f,x), \tag{4.6}$$

where $H_{out}(f,x)$ represents echoes from a planar reflector obtained as a reference at different axial locations x within the depth of field. The hypothesis is that these references would result in improved compression because the references more closely follow (4.1), i.e., they include the spatial impulse response corresponding to the spatial location of the target. Therefore, by having multiple references generated at various locations throughout the depth of field, a spatially varying Wiener filter could be constructed:

$$\beta_{REC}(f,x) = \frac{V_{lin}^{'*}(f,x)}{|V_{lin}^{'}(f,x)| + \gamma\overline{eSNR}^{-1}(f)}. \tag{4.7}$$

4.2.2 Experimental setup

Experiments were performed to test the spatially varying Wiener filter compression scheme. A single-element weakly focused (f/2.66) transducer (Panametrics, Waltham, MA) with a center frequency of 2.25 MHz and a 50% (at -3-dB) fractional bandwidth was used. These parameters were measured using the wire technique [97] for transducer characterization. The experimental setup utilized is described as follows:

The pre-enhanced chirp was generated in MATLAB and downloaded to an arbitrary waveform generator (Tabor Electronics W1281A, Tel Hanan, Israel). The excitation signal was amplified by a radio frequency power amplifier (ENI 2100L, Rochester, NY).

The amplified signal (50 dB) was connected to the transducer through a diplexer (Ritec RDX-6, Warwick, RI). The echo signal was received by a pulser-receiver (Panametrics 5800, Waltham, MA), which was displayed on an oscilloscope (Lecroy 9354 TM, Chester Ridge, NY) for visual verification. The echo signal was recorded at a rate of 200 MHz by a 14-bit analog-to-digital converter (Signatec PDA14-200, Newport Beach, CA) for further processing by a PC.

Measurements from a Plexiglas planar reflector, a 100 μm tungsten wire target surrounded by degassed water and a 120 μm nylon wire in a urethane rubber material were obtained to evaluate the compression performance of the spatially varying Wiener filter (4.7) vs. the conventional Wiener filter in (1.2). At a minimum, measurements were obtained for objects placed at the focus and at the depths before and after where the pressure amplitude was 6 dB below the focus.

4.2.3 Image quality metrics

To substantiate the improvements in the performance of the spatially varying Wiener filter, the following imaging quality metrics were used:

1. Sidelobe-to-mainlobe ratio (SMR): See Sec. 2.1.2 for more information.

2. Modulation transfer function (MTF): See Sec. 2.1.2 for more information.

4.2.4 Results

Planar reflector study

Experimental measurements from a planar reflector were obtained in increments of a wavelength throughout the depth of field. The resulting echoes were compressed using two methods: Compression with the conventional Wiener filtering with a $V_{lin}^{'}(f)$ reference from the focus as outlined by Oelze [18] and compression with a spatially varying Wiener filter that accounted for spatially varying $V_{lin}^{'}(f,x)$ references.

A snapshot of a few of the results highlighting the whole depth of field are displayed in Fig. 4.5. Note that in Fig. 4.5(a-c) multiple reflections from the planar reflector were visible and were only included to show the whole extent of the depth of field. The

results in Fig. 4.5(a) indicated that a maximum reduction in the sidelobe levels of 15 dB for the spatially varying Wiener filter was achieved. However, the average reduction in sidelobe levels when using the spatially varying Wiener filter was 10 dB. As the target approached the focus, Fig. 4.5(b), the reduction in sidelobe levels when using the spatially varying Wiener filter decreased with the maximum reduction at 13 dB and the average reduction at 8 dB. Furthermore, for targets closer to the focus, as shown in Fig. 4.5(c), the sidelobe levels for the spatially varying Wiener filter decreased with the maximum reduction at 10 dB and the average reduction of 5 dB. The echoes for both filters, the conventional Wiener filter and the spatially varying Wiener filter, should provide the same result when at the focus because the references used for compression were the same. This result is verified in Fig. 4.5(d). The results in Fig. 4.5(e-g) show the compression results when the target was located after the focus. Overall, the results in Fig. 4.5 suggest that the SVWF was more helpful at reducing the sidelobe levels as the target moved away from the focus.

Spatial resolution estimates based on the MTF for the plots in Fig. 4.5 are shown in Table 4.1. As expected, the spatial resolution when compressing with the Wiener filter and the spatially varying Wiener filter at the focus were the same, i.e., 302 μm. Moreover, when compressing targets outside the focus with the spatially varying Wiener filter, the spatial resolution estimates were consistently around the same spatial resolution value as the focus. When using the conventional Wiener filtering scheme, the spatial resolution estimates outside the focus degraded compared to the estimates at the focus. When using the conventional Wiener filter, the axial resolution deteriorated by 45% for the target located prior to the focus at the edge of the -6 dB depth of field. In addition, the axial resolution using the conventional Wiener filter at the same location was actually 2% worse than the axial resolution of CP. For the spatially varying Wiener filter, a gain of 43% in spatial resolution was obtained at the same location when compared to REC compressed with a conventional Wiener filter. These results suggest that the spatially varying Wiener filter was able to make all targets within the depth of field appear as if the target was being imaged at the focus. Therefore, the spatially varying Wiener filter improved the compression performance by increasing the axial resolution and decreasing sidelobe levels for the planar reflector target.

Tungsten wire targets

Experimental measurements of ultrasonic backscatter from a 100 μm tungsten wire were obtained at the focus and at the edges of the -6 dB depth of field. The resulting echoes were compressed using two methods: compression with the conventional Wiener filtering and compression with a spatially varying Wiener filter. While the imaging target was a wire, the reference waveforms for compression were taken from a planar Plexiglas plate.

The compressed images for wire targets at various locations in the -6 dB depth of field are shown in Figs. 4.6-4.8. When compressing signals from the edges of the depth of field with the spatially varying Wiener filter an increase in the eSNR of almost 5 dB was achieved compared to the conventional Wiener filter. In terms of sidelobe levels and spatial resolution, no significant improvements were obtained using qualitatively visual inspection of Figs. 4.6-4.8(a).

To get a better picture of the sidelobes, the on-axis plots in Figs. 4.6-4.8(b) were evaluated with quantitative metrics. The SMR for the long-range sidelobe were reduced by 3 to 5 dB in some locations while increases of 2 to 8 dB were observed in other locations. Similar increases were observed for the short-range sidelobes. Spatial resolution estimates based on the MTF for the plots in Fig. 4.6-4.8 are tabulated in Table 4.2. As expected, the spatial resolution values when compressing with the conventional Wiener filter and the spatially varying Wiener filter at the focus were the same, i.e., 426 μm. However, estimates of spatial resolution away from the focus were not as promising when using the spatially varying Wiener filter scheme for the wire targets. Examination of the spatial resolution estimated for points outside the focus revealed that the conventional Wiener filtering yielded better results for the wire target than the spatially varying Wiener filter.

The conclusion drawn from the the planar reflector study was that the spatially varying Wiener filter was helpful at improving the performance of the compression when the target was the same as the reference. However, for the wire target study, improvements were not observed in the spatial resolution and were marginal in the reduction of sidelobes and gain in eSNR. The system-dependent effects were partially compensated by using the spatially varying Wiener filter and compressing with references obtained at

the same spatial location as the target being imaged. Therefore, the main differences between the two studies were the shape and material of the imaging targets. Specifically, the scattering functions between the two targets were different because the collection of spatial impulse responses on the surface of the target were different. The scattering function for an object is related to the summation of the spatial impulse response of the field across the surface of the object.

To illustrate the collection of spatial impulse responses corresponding to the surface of an object more carefully, Field II simulations [108,109] of a planar reflector and a wire target were generated. The planar reflector and the wire target are continuous objects that were discretized in MATLAB as a collection of points, as shown in Fig. 4.9. The planar reflector was 10 mm wide and 10 mm high with grid points separated by 50 μm, which is much smaller than a wavelength. The wire was 150 μm wide and 10 mm high with grid points separated by 50 μm. For each grid point a spatial impulse response was calculated. The contribution of the spatial impulse responses or the sum is shown in the Field II simulation [108, 109] in Fig. 4.10.

The results in Fig. 4.10 suggest that a significant mismatch existed between references obtained from a planar reflector and the optimal filter design for the wire target. Therefore, it is hypothesized that for optimal compression the scattering function, which is related to the summation of spatial impulse responses incident on the target, should be taken into account. However, in a real imaging scenario only the spatial impulse response and the scattering function related to the reference geometry, i.e., planar reflector, are known. For the case of the planar reflector study, the imaging target was a planar reflector while the references were also from a planar reflector. Consequently, the improvements observed in the planar reflector study were due to "self-compression." Self-compression is the act of compressing echo signals with references made from the same object. With self-compression, both the collection of spatial impulse responses and the scattering function of the imaging object are compensated upon compression. Therefore, to further validate this hypothesis, the wire target's echoes were self-compressed (i.e., instead of using planar reflector references as usual, references were made from tungsten wire targets located at the same depth being imaged).

The self-compressed images for wire targets located at the edges of the -6 dB depth

of field are shown in Figs. 4.11-4.12(a). In the self-compressed cases, there were no improvements observed in eSNR similar to the gains observed using a spatially varying Wiener filter with a planar reflector as a reference. At first glance at Figs. 4.11-4.12, it would appear that noise was boosted. However, the apparent increase in noise is explained by the increase in the sidelobe levels slightly above the dynamic range of the imaging system. Overall, the sidelobe levels appeared to decrease in the self-compressed images when compared to the conventional compression scheme. In fact, the sidelobes were barely above the -50 dB amplitude level for both self-compressed cases as shown in the on-axis plots in Figs. 4.11-4.12(b). A significant improvement in the long-range sidelobe levels was observed when compared to the spatially varying Wiener filtering case when compressing with a planar reflector as a reference. For the self-compressed scenario where the reference was obtained at the same spatial location the target was imaged, the long range sidelobes were reduced by 5 dB in some locations and increased by about 2 dB in others. Overall there was a net reduction in sidelobe levels. In terms of the short-range sidelobe levels, a maximum reduction of 12 dB was observed. The short-range sidelobes were contained within the mainlobe of the conventional compression cases (planar reflector reference), which suggests that the self-compressed case had improved axial resolution.

Spatial resolution values obtained by evaluating the MTF for the targets plotted in Fig. 4.11-4.12 are listed in Table 4.2. The MTF results indicated that self-compression provided significant improvement in terms of axial resolution compared to compression with a planar reflector reference. For the self-compressed scattered signal, the axial resolution at the edge of the -6 dB depth of field prior to the focus improved by 26%. At the edge of the -6 dB depth of field after the focus, the improvement in axial resoltuion was 14%. Compared to CP, the improvements were 68% and 23%, respectively. These results suggested that by using a self-compressed spatially varying Wiener filter (wire target as a reference) not only were system effects partially compensated for, but target-dependent effects were also taken into account.

In summary, four compression scenarios were evaluated with the wire target:

1. Conventional Wiener filtering with the reference from a planar reflector obtained at the focus of the source. Results are shown in blue in Figs. 4.7(b) and 4.8(b).

This result did not compensate for spatially varying field effects or scattering.

2. Spatially varying Wiener filtering with the reference off of a planar reflector obtained at the same spatial location at which the target was located. Results are shown in green in Figs. 4.7(b) and 4.8(b). This result compensated for spatially varying field effects but not scattering.

3. Conventional Wiener filtering with the reference obtained from a wire located at the focus of the source. Results are shown in blue in Figs. 4.11(b) and 4.12(b). This result compensated for the scattering of the wire but not for the spatially varying effects.

4. Spatially varying Wiener filtering with the reference off of a wire target obtained at the same spatial location that the target was located. Results are shown in green in Figs. 4.11(b) and 4.12(b). This result compensated for both spatially varying effects and scattering.

The best results were achieved under scenario four as it reduced sidelobe levels and improved the axial resolution. Nonetheless, the results in scenario four pose a problem as it may potentially suggest that more than the system-dependent information must be known in order to significantly improve the compression performance. Specifically, information about the frequency dependent scattering from the object function must be known to account for scattering-dependent compression effects. Unfortunately, in most imaging scenarios this information is not given.

Nylon wire targets in the ATS phantom

Experimental measurements of a 120 μm nylon wire target inside the ATS tissue-mimicking phantom were obtained. The targets were imaged at the focus and at the edge of the -6 dB depth of field prior to the focus.

The compressed images for the target located at the focus are shown in Fig. 4.13(a). These images are shown as a reference for comparison because they are the gold standard for the entire depth of field. The compressed images for the target located prior to the focus are shown in Fig. 4.14(a). In Fig. 4.14(a) it was observed qualitatively that the spatially varying Wiener filter obtained a slightly better image in some regions where

the image appeared more crisp; however, sidelobes beyond the target appeared to have been accentuated. Although the sidelobe levels appeared higher for the spatially varying Wiener filter case, it was hard to assess the sidelobe levels in this scenario because the speckle due to subresolution scatterers may have compressed with more efficiency than the nylon wire target (i.e., the bandwidth matched the speckle response more for the spatially varying Wiener filter). Therefore, a significant roadblock exists to quantifying the sidelobe levels from these results. Furthermore, the ATS phantom images contain speckle in the background as opposed to a wire target in water. Therefore, the significant improvements in sidelobe levels could be buried beneath the speckle floor. Hence, only improvements in the axial resolution could be directly quantified.

For the ATS phantom results, instead of using MTF to obtain an estimate of spatial resolution, the more appropriate metric of speckle correlation length [32] was used. When compressing with the Wiener filter and the spatially varying Wiener filter, the speckle correlation lengths were estimated to be equal, i.e., 200 μm. For CP the correlation length was 606 μm. These results indicated that there were no significant differences between compressing REC echoes with a conventional Wiener filter and spatially varying Wiener filter.

In addition, the ATS data was compressed with references from a tungsten wire. The idea is that these references, although not made out of nylon, are still cylindrical in shape and would partially remove the scattering-dependent effects due to the wires and provide improved compression performance as observed with the tungsten wire targets. There were two scenarios studied: one using a tungsten wire located at the focus of the source as a reference. In this case, the effects of scattering were partially considered, but the spatially varying effects due to diffraction were not. The other scenario used a tungsten wire reference from the same spatial location at which the target was located. Therefore, both the spatially varying effect due to diffraction and scattering were partially taken into account.

The images of the target located at the edge of the -6 dB depth of field and compressed with a tungsten wire target reference are shown in Fig. 4.15(a). The speckle in the conventional Wiener filtering case appeared similar to the speckle in the CP case. This similarity in speckle would suggest that the axial resolution gain from using a pre-

enhanced chirp with REC was diminished. This similarity in speckle may have occurred because of a mismatch in the spectral content between the echo data and the reference. However, upon evaluating the on-axis plot in Fig. 4.15(b), a loss in resolution was not observed when comparing images produced with the conventional Wiener filter to the spatially varying Wiener filter. For images produced with the spatially varying Wiener filter case, the portion of the image near the target appeared to be slightly blurry. Similarly, the width of sidelobes for the spatially varying Wiener filter in Fig. 4.15(b) appeared slightly wider, indicating some loss in axial resolution. The spatial resolution as determined by the speckle correlation length for the conventional Wiener filter case was 266 μm. For the conventional Wiener filter case, the speckle correlation length increased by 29% when the reference changed from a planar reflector to a tungsten wire target. For the spatially varying Wiener filter, the spatial resolution as determined by the correlation length was 200 μm. In terms of sidelobes, the spatially-varying wiener filter (wire reference) appeared to have a lower amplitude level compared to using a planar reflector reference. Moreover, there was a decrease in the mainlobe amplitude. The decrease in mainlobe amplitude resulted from a difference in echo amplitude level between the planar reflector and wire target reference. Overall, compressing with a wire added what appeared to be sidelobes by an average of 6 dB when compared to the case when the references were planar reflectors. Overall, the spatially varying Wiener filter when the reference was a tungsten wire target did not add any benefits to the compression performance.

Finally, for completion of the study, the ATS data was self-compressed with references obtained from the nylon wire targets inside the ATS phantom. Because echoes from wire target were stronger than the background, careful extraction of the reference was possible so that information from the speckle background was not part of the reference. Two scenarios were studied. In secenario one, the reference was a nylon wire located at the focus of the source. In this case, the effects of scattering were considered but the spatially varying effects were not. The other scenario used a nylon wire reference from the same spatial location at which the target was located. Therefore, the spatially varying effects and scattering were taken into account.

The compressed images for the scenario when the target was located at the edge

of the -6 dB depth of field and compressed with a nylon wire target are shown in Fig. 4.16(a). The speckle before and after the target in the spatially varying Wiener filtering case appeared slightly blurry. However, the overall image excluding these regions appeared quite crisp and full of detail. Evaluating the on-axis plot in 4.16(b) it was observed that a decrease in the sidelobe levels of about 2 dB was obtained when comparing the spatially varying Wiener filtered case using a nylon target reference to the conventional Wiener filtering using a planar reflector reference. However, a large decrease in the axial resolution was visible. The spatial resolution as determined by the speckle correlation length for the conventional Wiener filter case was 902 μm. For the conventional Wiener filter case, the speckle correlation length increased by 337% when the reference changed from a planar reflector to a nylon wire target. For the spatially varying Wiener filter, the spatial resolution as determined by the correlation length was 754 μm. Overall, compressing with nylon targets as references did not improve the compression performance, regardless of whether the Wiener filter was spatially varying or not.

4.3 Spatially Varying Wiener Filter with a Spatially Varying $\overline{eSNR}$

In the original design of the REC technique [18], the compression of each scan line utilized the Wiener filter as described in (1.2) with a constant $\overline{eSNR(f)}$. $\overline{eSNR}$ (1.4) was defined as the average eSNR per frequency channel in each scan line. In this subsection, the effects of the spatially varying nature of the $\overline{eSNR}$ were evaluated. In addition, a technique to adaptively compensate for the changes in $\overline{eSNR}$ spatially in the compression scheme (Wiener filter) were examined. The overall objective is to improve the compression performance (sidelobes, spatial resolution, and eSNR) throughout the image.

4.3.1 $\overline{eSNR}$

Estimating a single $\overline{eSNR(f)}$ per scan line could be problematic in various scenarios. For example, in one scenario, one scan line could have a large amount of electronic

noise compared to other scan lines making up an image. In another example, a portion of a scan line could have a very strong specular reflection from a point target and the remaining portion of the scan line contain speckle from weak scatterers. Consequently, the specular reflector would increase the eSNR estimated for the scan line, which would in turn adjust the operating point of the Weiner filter. An increase in the eSNR would move the Weiner filter closer to an inverse filter. As a Wiener filter approaches an inverse filter the sidelobes are reduced, the resolution is improved and the noise is amplified. As a result, depending on the exact location of the operating point, the filter could be more efficient in compressing the strong specular reflector but could increase the noise in the portion of the signal with speckle only. The end result would be an image with poor quality. The image could partially be improved by adjusting the gamma parameter to shift the operating point towards a matched filter. In this scenario, the speckle portion of the signal would be above the noise floor, but the specular reflection would be characterized by larger sidelobes and a decrease in axial resolution. Therefore, to ameliorate these effects a spatially varying Wiener filter that takes into account the spatially varying nature of the eSNR was studied.

The spatially varying Wiener filter based on a spatially varying eSNR is described by the following equation:

$$\beta_{REC}(f) = \frac{V_{lin}^{'*}(f)}{|V_{lin}^{'}(f)|^2 + \gamma \overline{eSNR_0}^{-1}(f, x_0)}, \tag{4.8}$$

where $\overline{eSNR_0}$ is the echo-signal-to-noise ratio per frequency channel for the spatial region of interest defined by the axial location, x_0. $\overline{eSNR_0}$ can be described by the following expression:

$$\overline{eSNR_0(f, x_0)} = \overline{eSNR(f, x)} var(g(x_0)), \tag{4.9}$$

where the variance of the echo signal $g(x_0)$ is taken over a windowed segment using a rectangular window centered at x_0. To obtain the variance of the echo signal at location x_0, the backscattered data are compressed twice. The first compression creates a spatial map of signal strength throughout the whole image region by assuming a uniform eSNR for the scan line. From there, a map of the variance of the compressed

echoes for smaller sub-regions of the image is determined. This map is used in the spatially varying Wiener filter to adaptively select the operating point of the Wiener filter for each particular region of interest. Consequently, regions containing stronger signals will be filtered closer to an inverse filter to improve spatial resolution and sidelobe levels. Regions containing weaker echoes will be filtered closer to a matched filter to make targets visible by removing the noise at the expense of increasing the sidelobe levels and deteriorating the axial resolution. Compressing with the spatial map of eSNR can become significant when frequency-dependent attenuation is present because the image quality can be improved at all depths. The final image is constructed by stitching together each of the the compressed regions of interest.

4.3.2 Computer simulations

Computer simulations were carried out in MATLAB (Mathworks, Natick, MA) to characterize the performance of the spatially varying Wiener filter based on spatially varying maps of $\overline{eSNR}$. Computer simulations were chosen over experimental measurements in order to control image parameters more carefully. The simulations used a received pulse-echo pressure field model [93] described as

$$g'[x, y, t] = h_1(t) * f(x, y) * h_{pe}(y, t), \tag{4.10}$$

where x represents the axial spatial coordinate, y represents the lateral spatial coordinate, $f(x, y)$ is the scattering function, and $h_{pe}(y, t)$ is the modified pulse-echo spatial impulse response that takes into consideration the geometry of the transducer to the spatial extent of the scattered field (beam diffraction).

The pulse-echo impulse response, $h_1(nT, x)$, for CP was approximated by

$$h_1(t) = e^{-\frac{t^2-\tau}{\sigma_t^2}} \cos(\omega t), \tag{4.11}$$

where σ_t^2 is the second central moment of the Gaussian pulse which dictates the bandwidth of the pulse. A shift, τ, was added to $h_1(t)$ to make the pulse causal. The generated pulse-echo impulse response was located at the focus of a 2.25 MHz single-element transducer (f/4) with a -6 dB fractional bandwidth of 70%.

For REC, the impulse response function, $h_2(t)$, was constructed to have a -6 dB fractional bandwidth of 150% by gating a sinusoid of four cycles with a Hanning window

$$w(n) = \begin{cases} 0.5(1 - \cos(\frac{2\pi n}{L_H - 1})), & 0 \leq n \leq L_H - 1 \\ 0, & \text{otherwise,} \end{cases} \tag{4.12}$$

where n is an integer and L_H is the number of samples in the window. A Hanning window of length of $L_H = 96$ was used.

The spatial response for a circular focused piston source was simulated as a circular Gaussian beam, which is defined as

$$h_{pe}(y,t) = \delta(t - \frac{2R_d}{c}) e^{\frac{-y^2}{\sigma_y^2}}, \tag{4.13}$$

where R_d is the distance from the source to target in space, c is the speed of sound of the medium which was set to 1540 m/s, and σ_y is the -6 dB lateral beamwidth which is equal to 2.05 mm.

To assess the performance of the spatially varying Wiener filter, several imaging targets were evaluated. First, a simulation of a phantom S1 containing 12 point targets spaced 5 mm apart in water was evaluated. Attenuation of 2 dB $\text{MHz}^{-1}\text{cm}^{-1}$ was added to the simulation so that a decrease in backscattered energy from the point targets away from the source was achieved. Phantom S1 was evaluated for two different cases of noise floors: low noise and high noise. For the low noise case, the $eSNR$ for the region including the first point target was 62 dB. For the high noise case, the $eSNR$ in the region including the first point target was 22 dB. In the next simulation, phantom S2 was the same as the first phantom except that the wire targets were embedded in a medium producing speckle. Finally, phantom S3 contained a cystic target at the center of the phantom. Only the high noise scenario was evaluated with phantoms S2 and S3.

4.3.3 Results

The B-mode images for phantom S1 under the low noise scenario are shown in Fig. 4.17 along with an axial profile through the center of the B-mode images. Compared to CP, the B-mode images constructed using conventional REC resulted in improved axial

resolution but increases in sidelobe levels and deterioration in lateral resolution. For REC-SVWF the sidelobe levels decreased when compared to REC echoes compressed with a conventional Wiener filter. The spatial resolutions as determined by MTF for CP and for REC echoes compressed with a conventional Wiener filter and a spatially varying Wiener filter are listed in Table 4.3. Overall, the spatially varying Wiener filter had a slight degradation in axial resolution in order to improve the sidelobe levels and the eSNR. Furthermore, the amplitude of the echoes from each target was more correct with the spatially varying Wiener filter than with a conventional Wiener filter. For the conventional Wiener filter both the signal and the noise floor were boosted. The purpose of evaluating phantom S1 in a low noise environment was to show that no artifacts or significant degradation in image quality occurred.

The B-mode images for phantom S1 under the high noise scenario are shown in Fig. 4.18 along with an axial profile through the center of the B-mode images. In the high noise scenario, the spatially varying Wiener filter allowed the operating point of the Wiener filter to remain at the same operating point as in the low-noise scenario. Consequently, when using the spatially varying Wiener filter the axial resolution was nearly the same as in the low noise scenario with the added benefit that the noise floor was pushed below the dynamic range of the image. In the scenario where a conventional Wiener filter was used for compression in the high noise case, the γ parameter was adjusted until the noise was removed. This adjustment increased sidelobe levels and degraded the axial resolution in order to improve the eSNR. Therefore, the benefits of the spatially varying Wiener filter were clearly observed in this case. The spatial resolution as determined by MTF for CP and for REC echoes compressed with a conventional Wiener filter and a spatially varying Wiener filter are listed in Table 4.4. Similar to the low noise case, the spatially varying Wiener filter had a slight degradation in axial resolution in order to improve the sidelobe levels and the eSNR. Overall, the results for phantom S1 suggested that the spatially varying Wiener filter improved the image quality over CP and REC using with a conventional Wiener filter.

The B-mode images for phantom S2 under the high noise scenario are shown in Fig. 4.19 an axial profile through the center of the B-mode images. In the REC case shown in Fig. 4.19(a), i.e., echoes compressed with a conventional Wiener filter, the point

targets that were further away from the source became blurry in the image. The blurry targets were a result of the effects of frequency-dependent attenuation that decreased the eSNR as a function of depth. Consequently, the γ parameter forced the operating point of the Wiener filter towards an inverse filter in order to reduce sidelobe levels and obtain improved resolution at the expense of boosting the noise. The noise boost degraded the image as the imaging depth increased. When compared to CP, the results obtained with conventional REC were still a slight improvement because of the increased depth of penetration into phantom S2. However, when using the spatially varying Wiener filter, results were further improved by reducing the amount of blur in the speckle at depths greater than 60 mm. The spatially varying Wiener filter was adjusting the operating point as a function of depth as the eSNR was decreasing. Therefore, the spatially varying Wiener filter improved results by reducing the amount of blurring of speckle at depths greater than 60 mm. However, the tradeoff was that a degradation in axial resolution was obtained and a slight increase in sidelobe levels was observed at these depths. Overall, the spatially varying Wiener filter applied on phantom S2 showed promising results as image quality improved at depths where CP had low eSNR and conventional REC contained a large amount of noise and sidelobes.

Finally, phantom S3 was evaluated under the high noise scenario. The B-mode images for phantom S3 under the high noise scenario are shown in Fig. 4.20 an axial profile through the center of the B-mode is shown in Fig. 4.21. Phantom S3 consisted of a cystic target surrounded by tissue-mimicking material. The cystic target evaluated was equivalent to a fluid-filled target with no internal scattering objects. Therefore, the only backscattered signal present in that region would be additive noise. By applying a spatially varying Wiener filter, the noise in the cystic region could be removed by shifting the operating point of the Wiener filter towards a matched filter. With conventional Wiener filtering the cystic region is smeared by either sidelobes or noise. Consequently, the dimensions of the cystic target became much smaller. This could potentially be a problem if the region was small because the sidelobes and noise could mask the region. Therefore, the results of the spatially varying Wiener filter compression scheme for this target clearly displayed the benefit of using a spatially varying Wiener filter. Note that in this simulation there was no attenuation present; therefore, the amplitude did

not decrease with increasing depth. However, with the spatially varying Wiener filter the speckle appeared to have increased because regions that were buried in noise using conventional Wiener filtering and CP were now anechoic and noise-free. To quantify the improvement using the spatially varying Wiener filter, the CNR metric was applied to obtain a measure of contrast between the cyst and the background region. CNR for CP was 1.69. For REC, the CNR was 1.92 and 3.29 for the conventional Wiener filter and the spatially varying Wiener filter, respectively. Overall, the spatially varying Wiener filter based on spatially varying maps of the signal-to-noise ratio significantly improved image quality by increasing the contrast when compared to CP and REC echoes compressed with a conventional Wiener filter.

4.4 Conclusion

In this chapter several spatially varying Wiener filters were evaluated. Initially, a spatially varying Wiener filter that corrects for diffraction effects locally was tested. It was observed that the spatially varying Wiener filter worked for large specular objects such as a planar reflector. Moreover, another spatially varying Wiener filter was implemented that corrects for scattering effects locally as evaluated in the wire target study. The conclusion of that study was that the spatially varying Wiener filter based on planar references offered little help at improving the compression performance. Therefore, the new filter was limited in improving only planar-surface-like targets and not targets with curved surfaces.

Furthermore, another spatially varying Wiener was evaluated by correcting for both scattering and diffraction locally. Under this spatially varying Wiener filter, it was established that improved results were obtained because of self-compression. Self-compression is not easily implementable as frequency-dependent scattering because the object function must be known to account for scattering-dependent effects.

Finally, the most promising spatially varying Wiener filter evaluated corrected for $\overline{eSNR}$ locally to improve compression performance. Specifically, the eSNR was increased in deeper areas imaged at the expense of a small degradation in spatial resolution and slight increase in sidelobe levels. Images of wire targets and anechoic lesion were observed to improve in simulations compared to conventional methods of imaging.

4.5 Figures and Tables

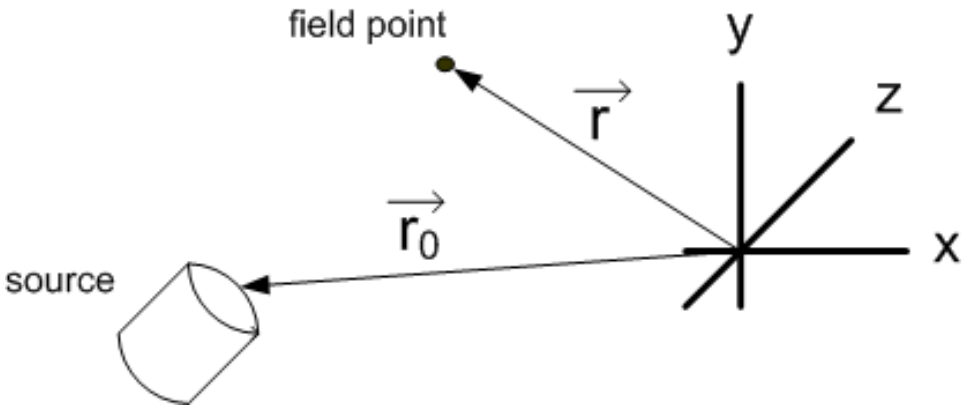

Figure 4.1: Description of coordinate system for calculation of spatial impulse responses.

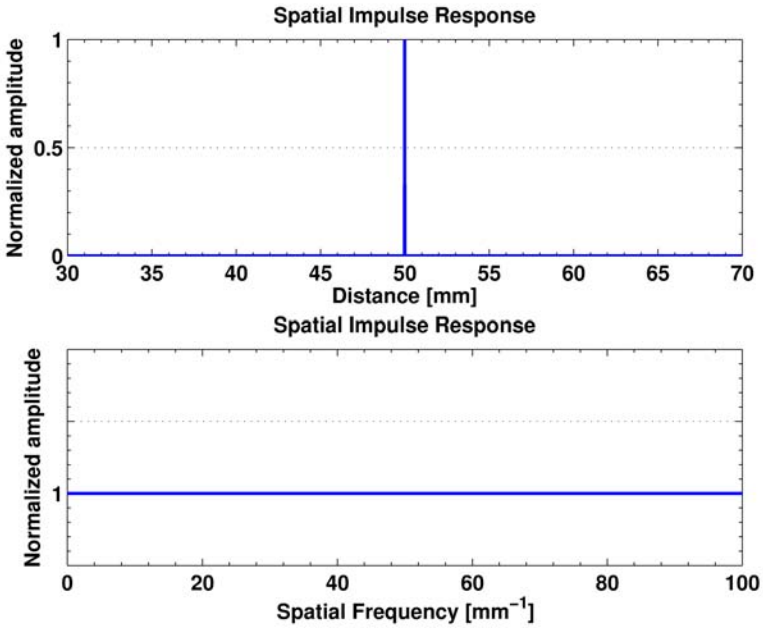

Figure 4.2: Spatial impulse response as a function of distance and as function of spatial frequency for a 2.25 MHz (f/3) source. The field point is located at the focus, i.e., $x = 0$, $y = 0$, and $z = 50$ mm.

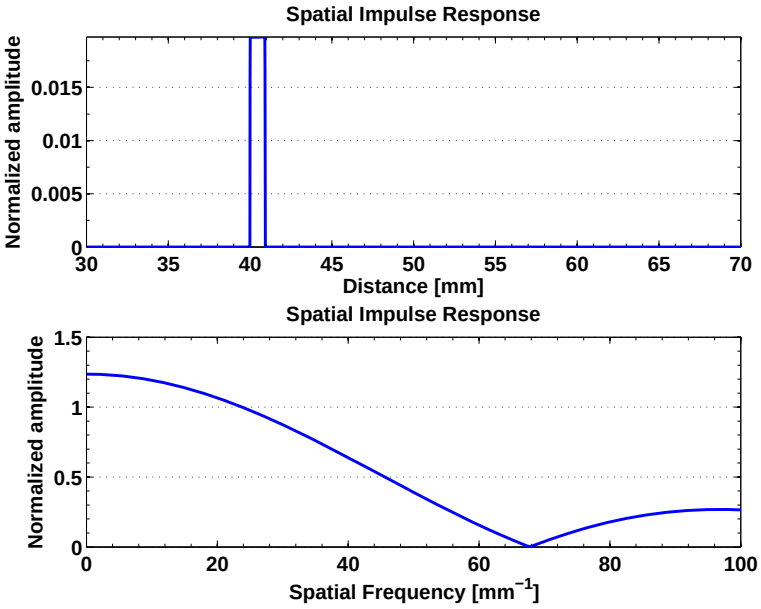

Figure 4.3: Spatial impulse response as a function of distance and as function of spatial frequency for a 2.25 MHz (f/3) source. The field point is located 10 mm before the focus, i.e., $x = 0$, $y = 0$, and $z = 40$ mm. These plots have been normalized with respect to the spatial impulse response at the focus.

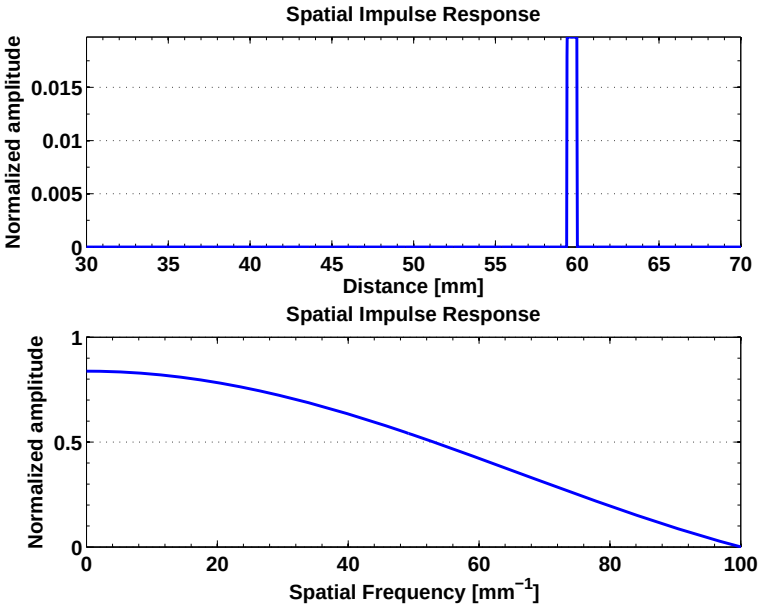

Figure 4.4: Spatial impulse response as a function of distance and as function of spatial frequency for a 2.25 MHz (f/3) source. The field point is located 10 mm after the focus, i.e., $x = 0$, $y = 0$, and $z = 60$ mm. These plots have been normalized with respect to the spatial impulse response at the focus.

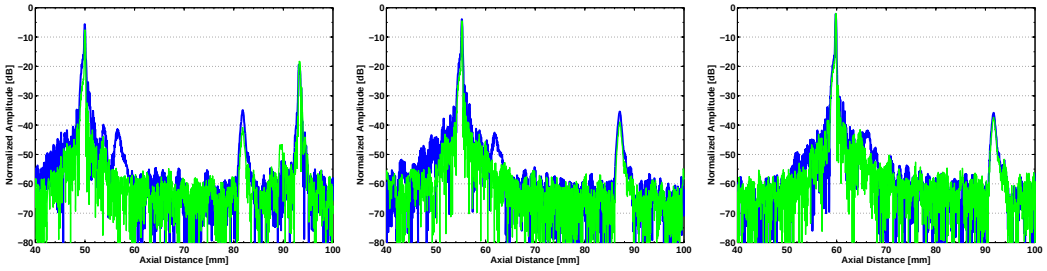

(a) @ -6 dB amplitude before the focus

(b) @ -4 dB amplitude before the focus

(c) @ -2 dB amplitude before the focus

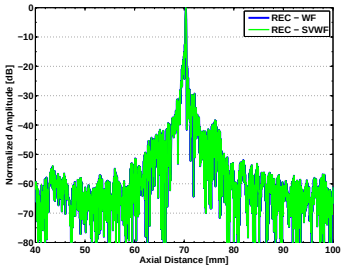

(d) @ focus

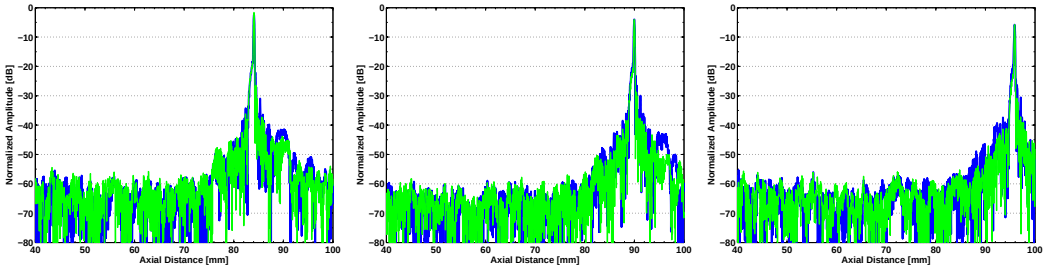

(e) @ -2 dB amplitude after the focus

(f) @ -4 dB amplitude after the focus

(g) @ -6 dB amplitude after the focus

Figure 4.5: The compression results from a spatially varying Wiener filter (SVWF) versus a conventional Wiener filtering (WF) at various locations throughout the depth of field.

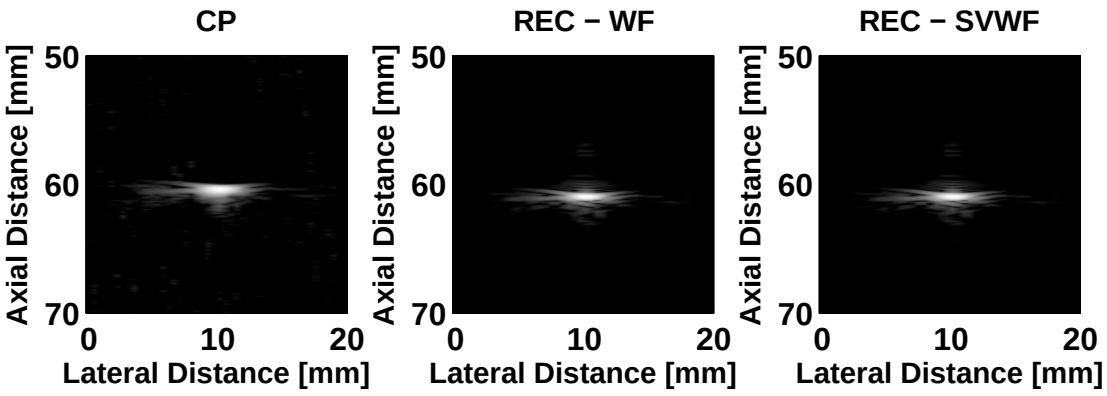

(a)

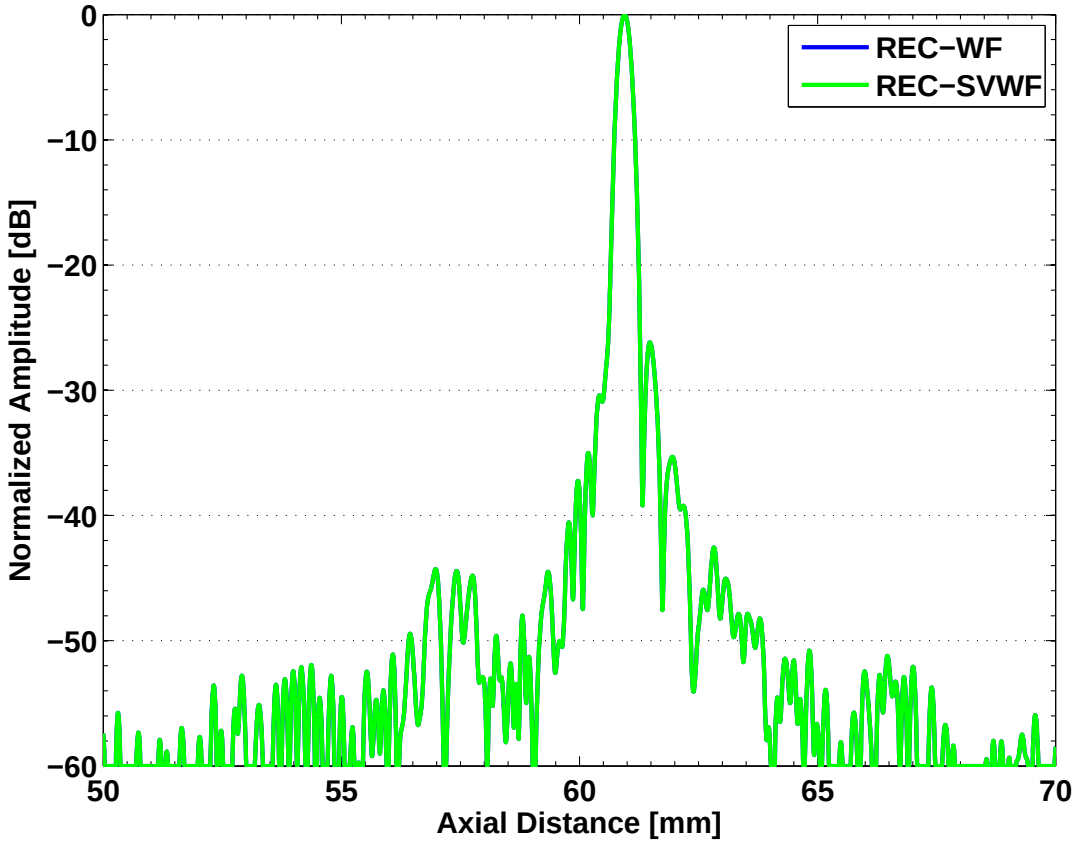

(b)

Figure 4.6: (a) B-mode image and (b) on-axis plot of a 100 μm tungsten wire target located at the focus for both conventional Wiener filtering (WF) and spatially varying Wiener filtering (SVWF). Image dynamic range = -50 dB.

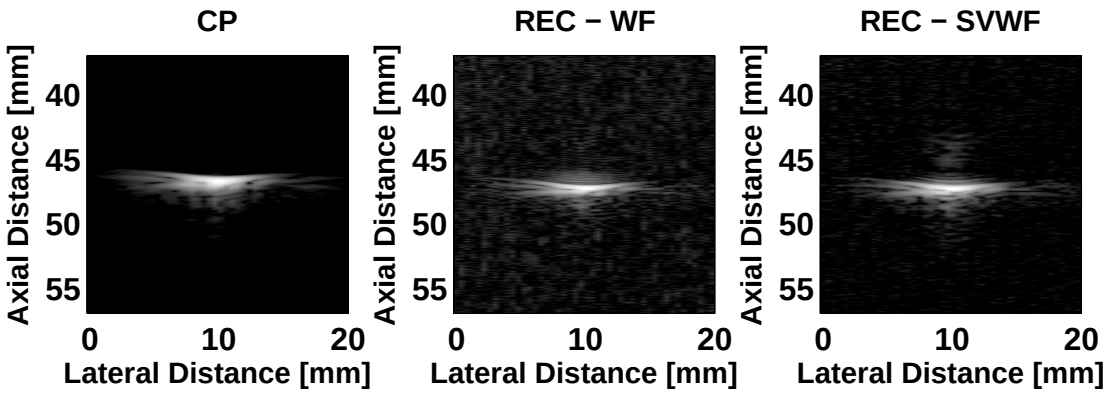

(a)

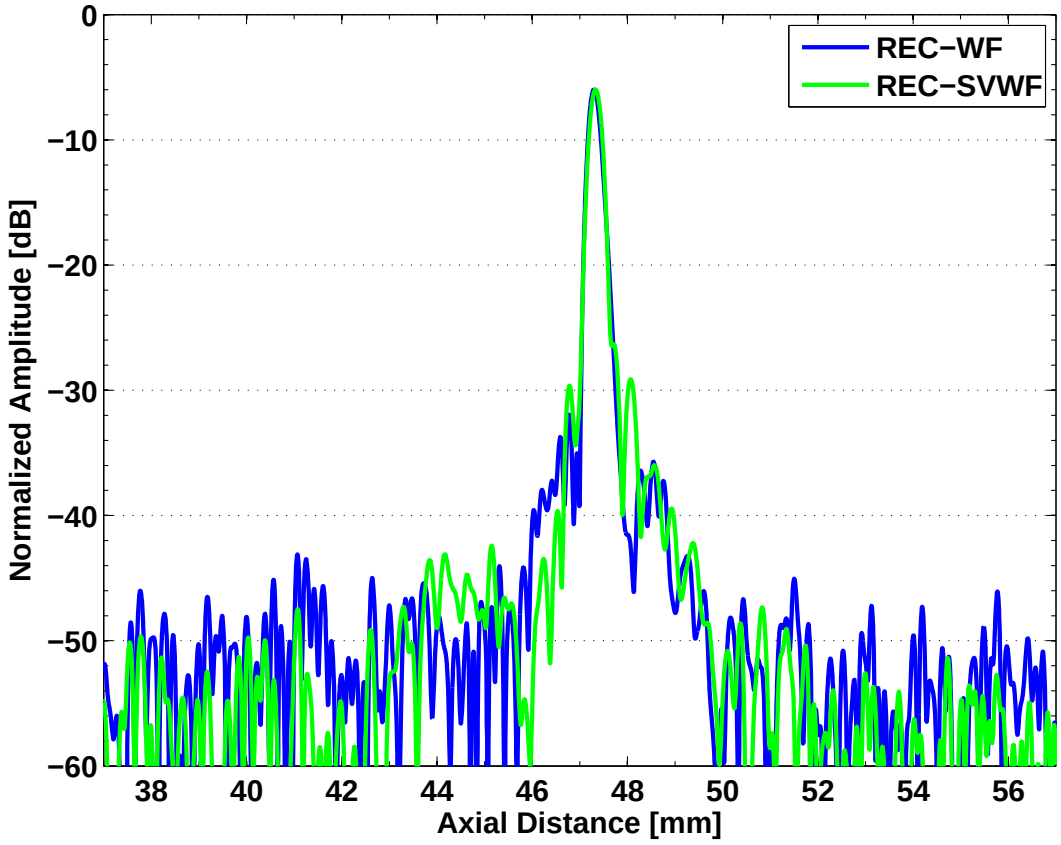

(b)

Figure 4.7: (a) B-mode image and (b) on-axis plot of a 100 μm tungsten wire target located at -6 dB amplitude point before the focus for both conventional Wiener filtering (WF) and spatially varying Wiener filtering (SVWF). Image dynamic range = -50 dB.

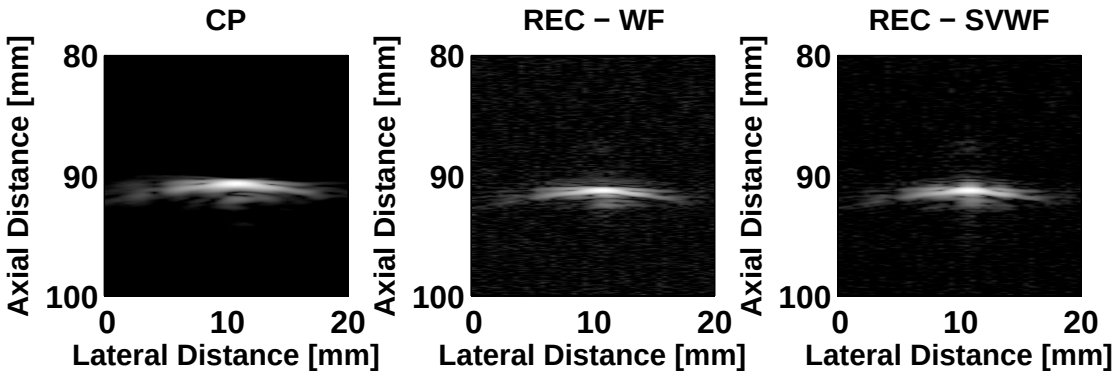

(a)

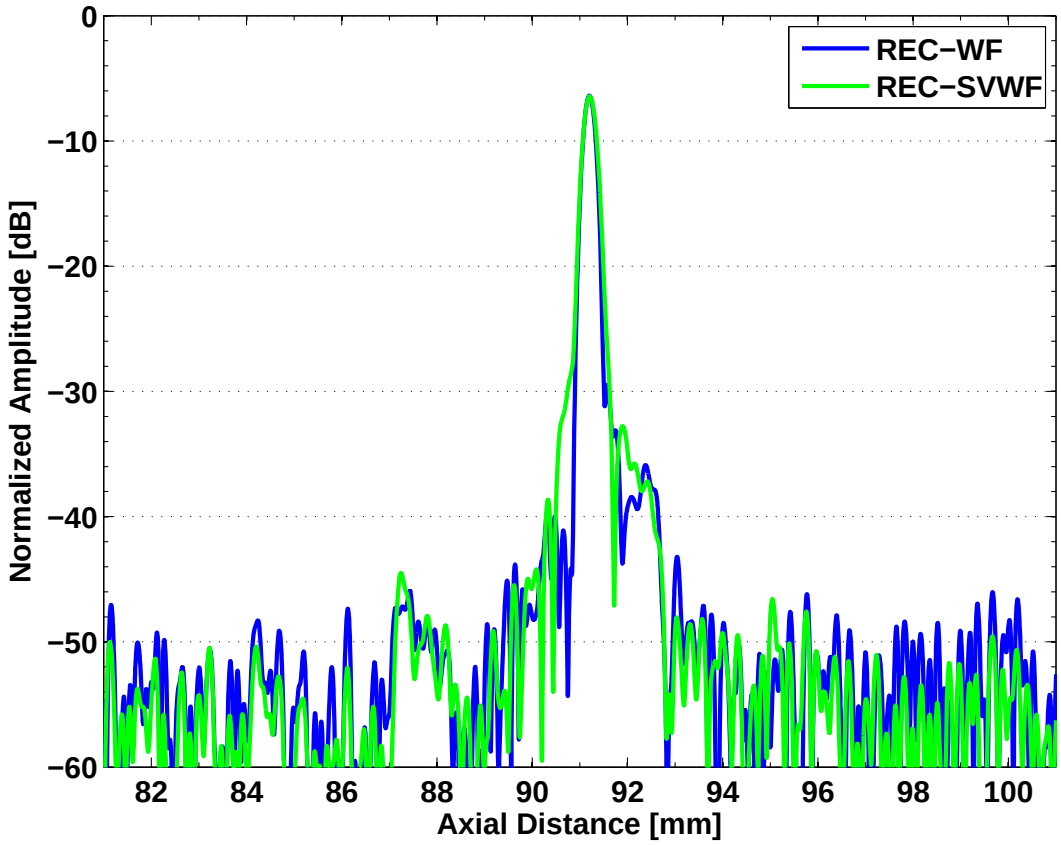

(b)

Figure 4.8: (a) B-mode image and (b) on-axis plot of a 100 μm tungsten wire target located at -6 dB amplitude point after the focus for both conventional Wiener filtering (WF) and spatially varying Wiener filtering (SVWF). Image dynamic range = -50 dB.

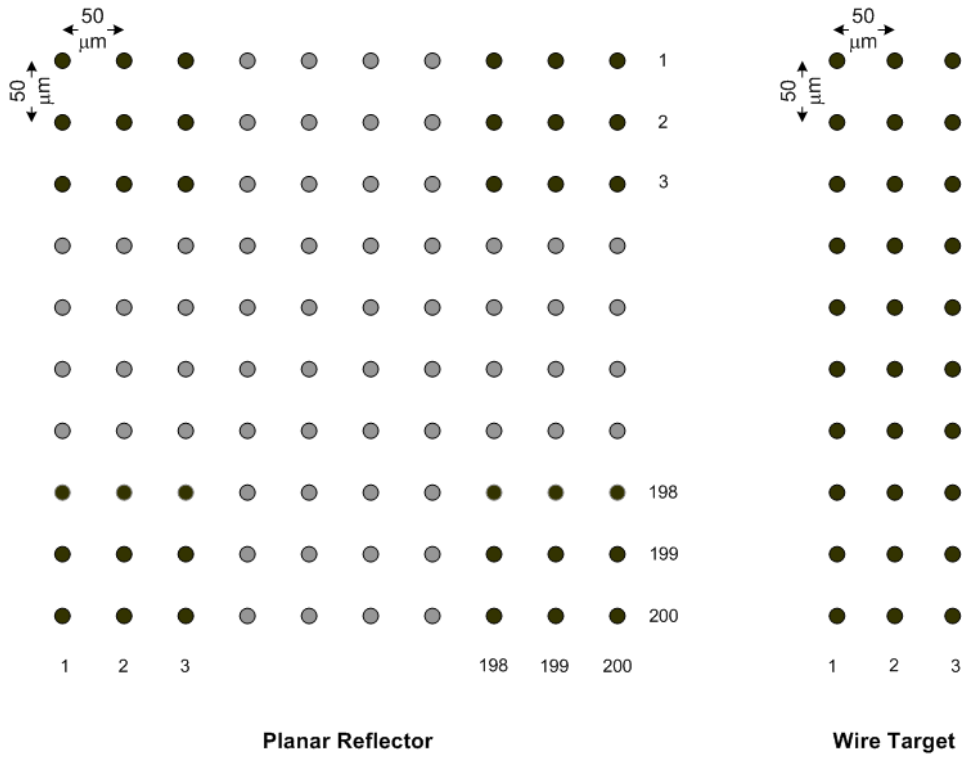

Figure 4.9: Input grid used for planar reflector and wire target in Field II simulations.

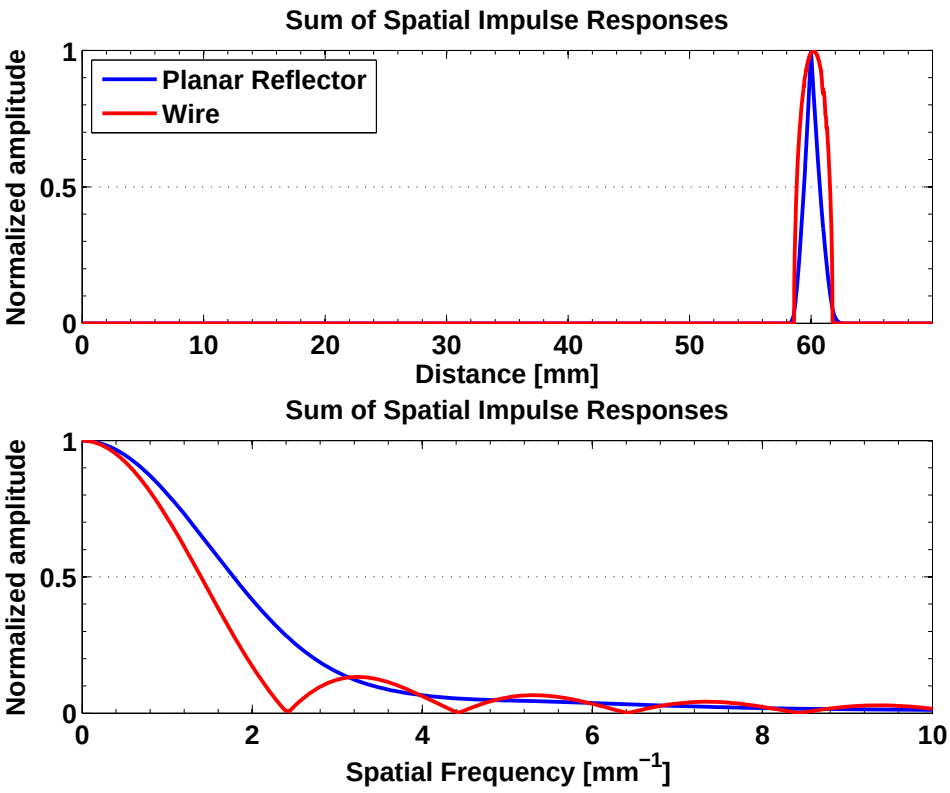

Figure 4.10: Sum of the spatial impulse response from each grid point as a function of distance and as function of spatial frequency for a 2.25 MHz (f/3) source with a focal depth of 60 mm for planar reflector (blue) and a wire target (red). These plots have been normalized to their respective maximum amplitude for shape comparison. The ratio of maximum amplitude between the wire and planar reflector was 0.82%.

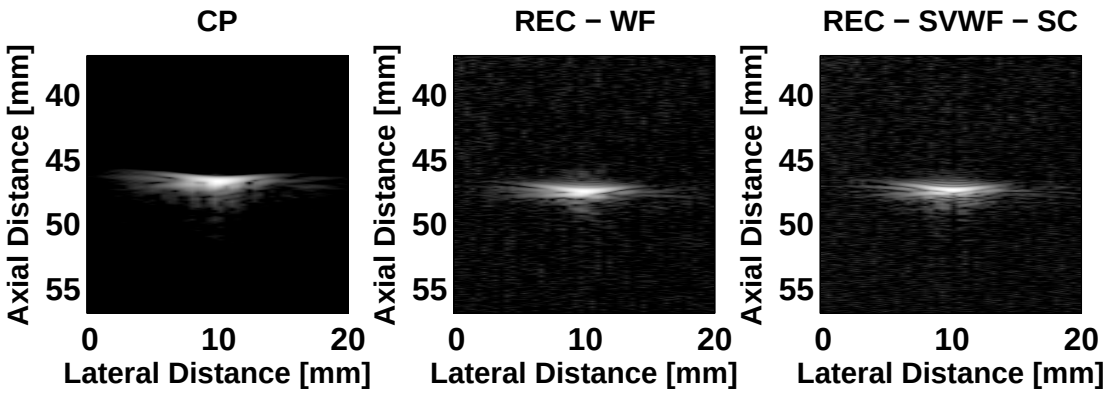

(a)

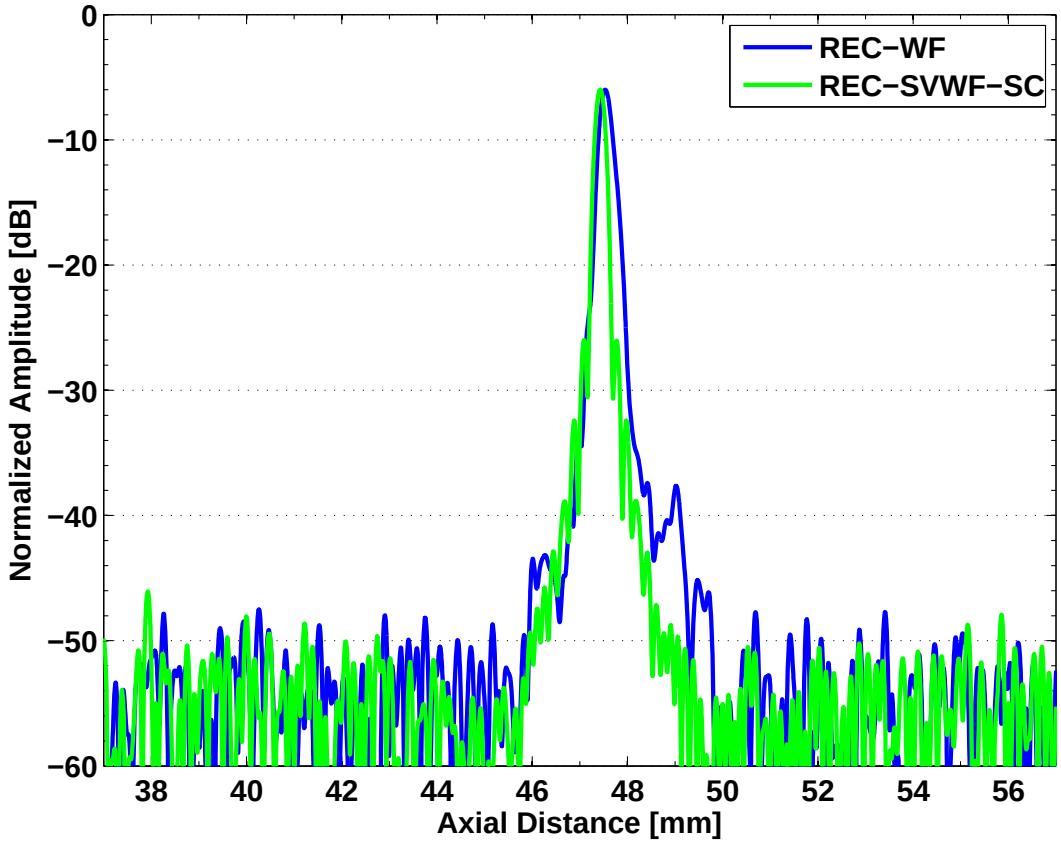

(b)

Figure 4.11: (a) B-mode image and (b) on-axis plot of a 100 μm tungsten wire target located at the edge of -6 dB depth of field before the focus for both conventional Wiener filtering (WF) and spatially varying Wiener filtering (SVWF). In this case, WF identifies echoes that have been compressed with a tungsten wire target located at the focus. SVWF-SC identifies echoes that have been self-compressed (i.e., the reference is from a tungsten wire located at the same depth the target was imaged). Image dynamic range = -50 dB.

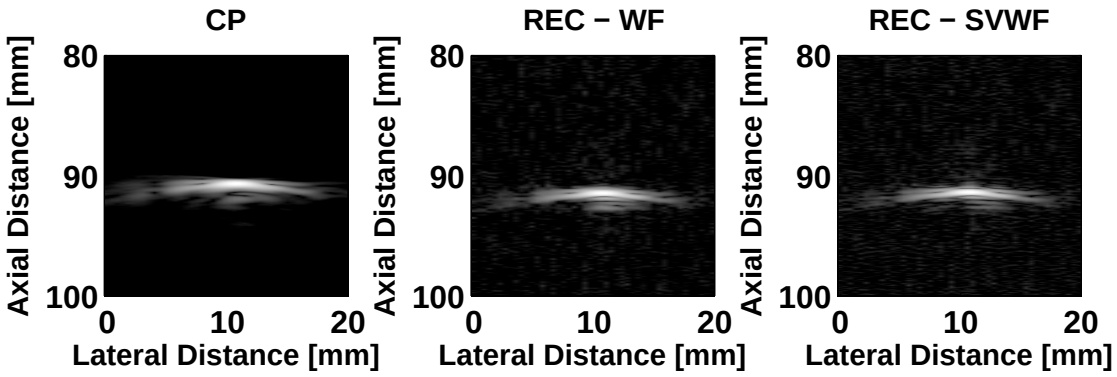

(a)

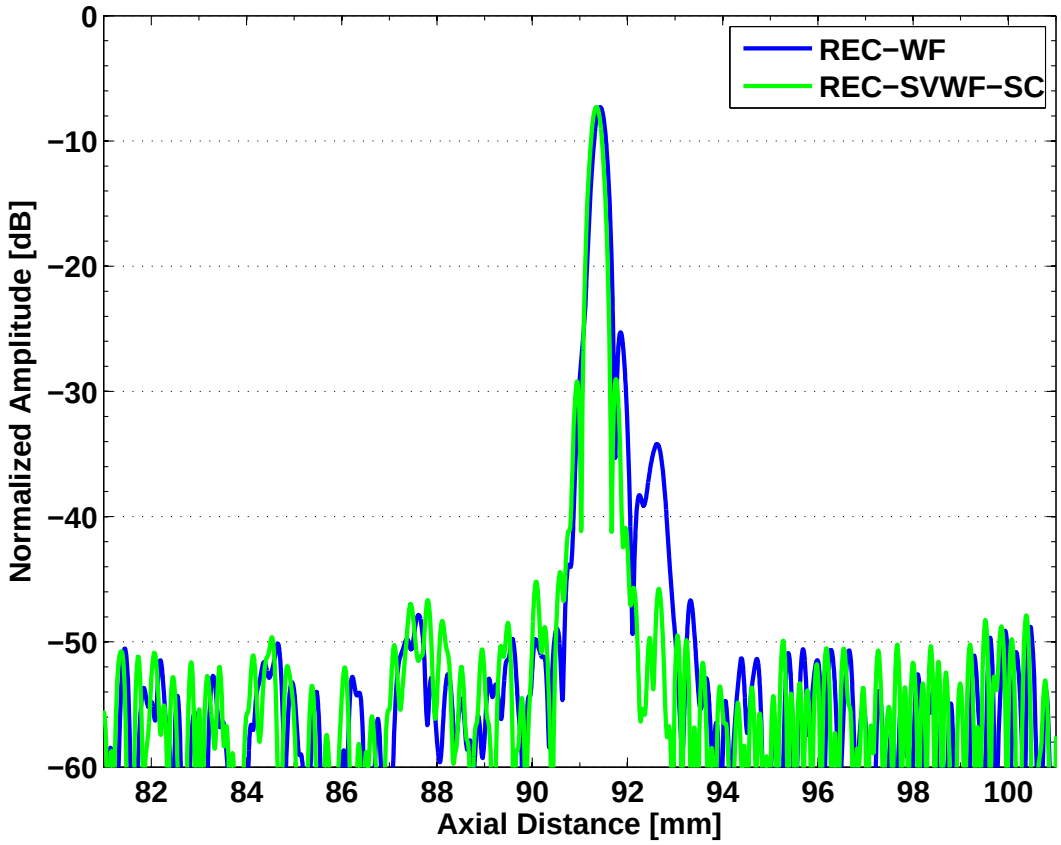

(b)

Figure 4.12: (a) B-mode image and (b) on-axis plot of a 100 μm tungsten wire target located at the edge of the -6 dB depth of field after the focus. In this case, WF identifies echoes that have been compressed with a tungsten wire target located at the focus. SVWF-SC identifies echoes that have been self-compressed (i.e., the reference is from a tungsten wire located at the same depth the target was imaged). Image dynamic range = -50 dB.

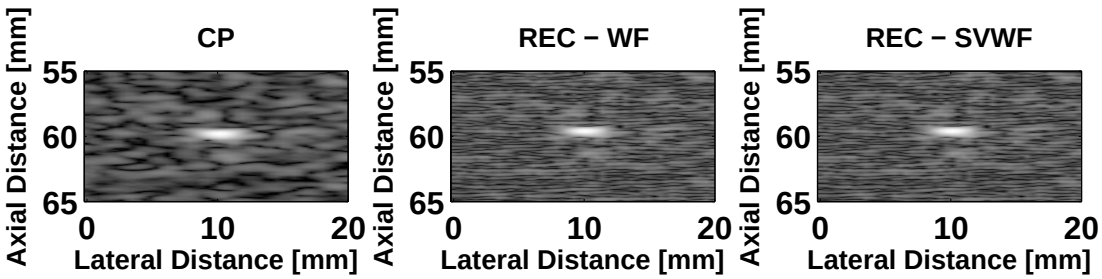

(a)

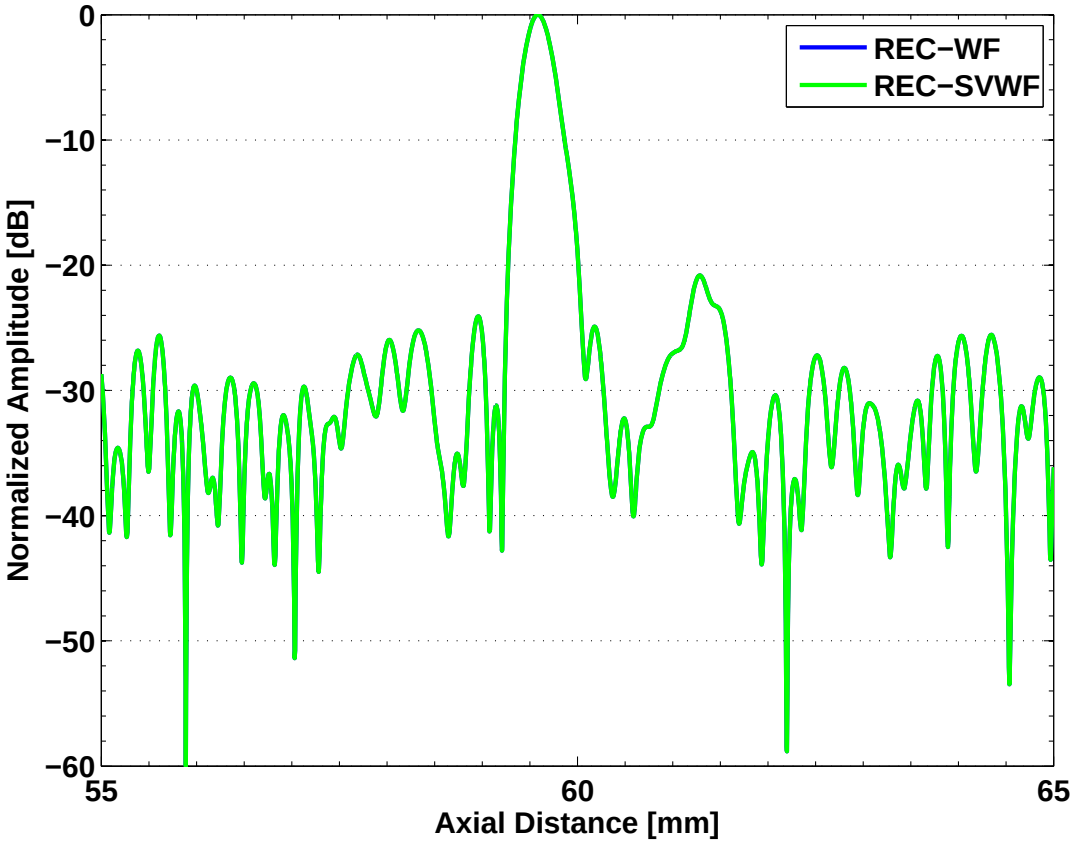

(b)

Figure 4.13: (a) B-mode image and (b) on-axis plot of a 120 μm ATS nylon wire target located at the focus for both conventional Wiener filtering (WF) and spatially varying Wiener filtering (SVWF). Image dynamic range = -50 dB.

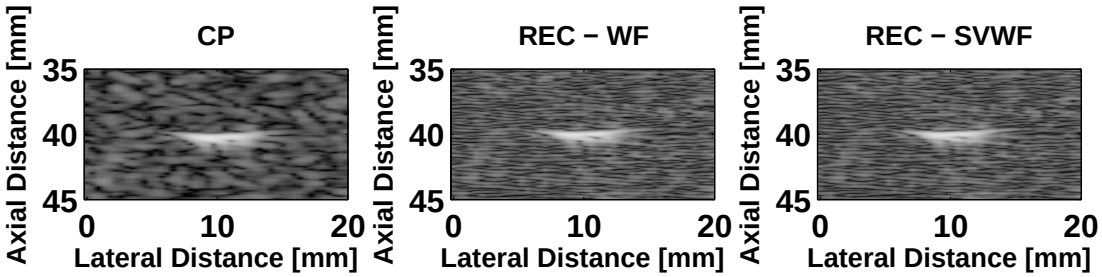

(a)

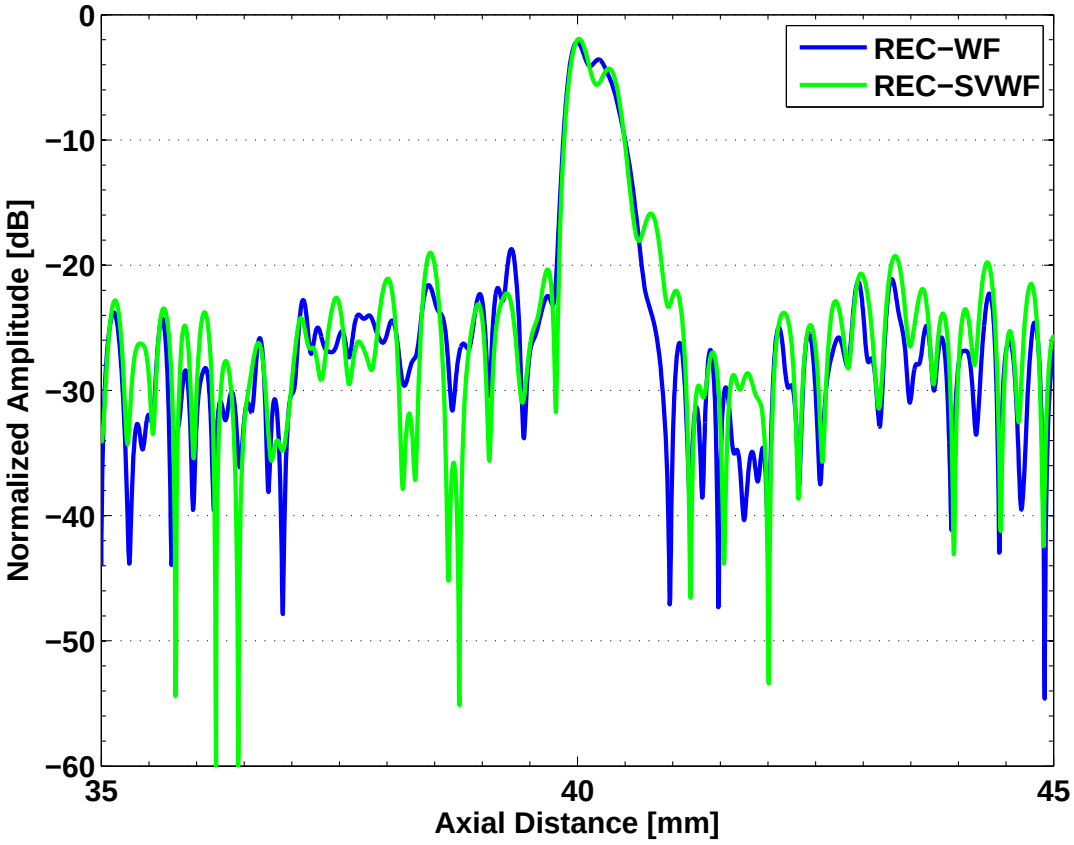

(b)

Figure 4.14: (a) B-mode image and (b) on-axis plot of a 120 μm ATS nylon wire target located at the edge of the -6 dB depth of field prior to the focus for both conventional Wiener filtering (WF) and spatially varying Wiener filtering (SVWF). Image dynamic range = -50 dB.

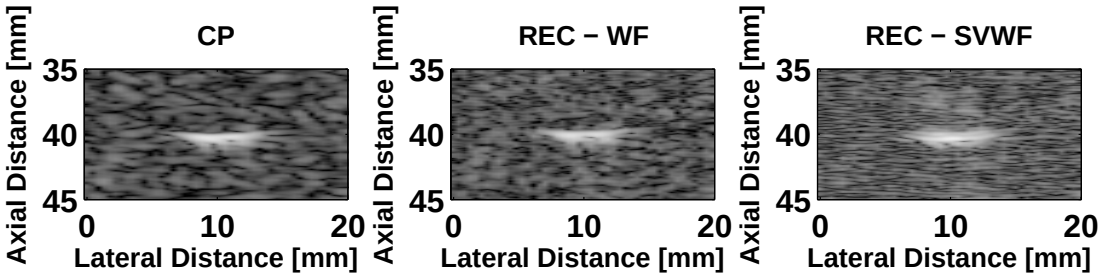

(a)

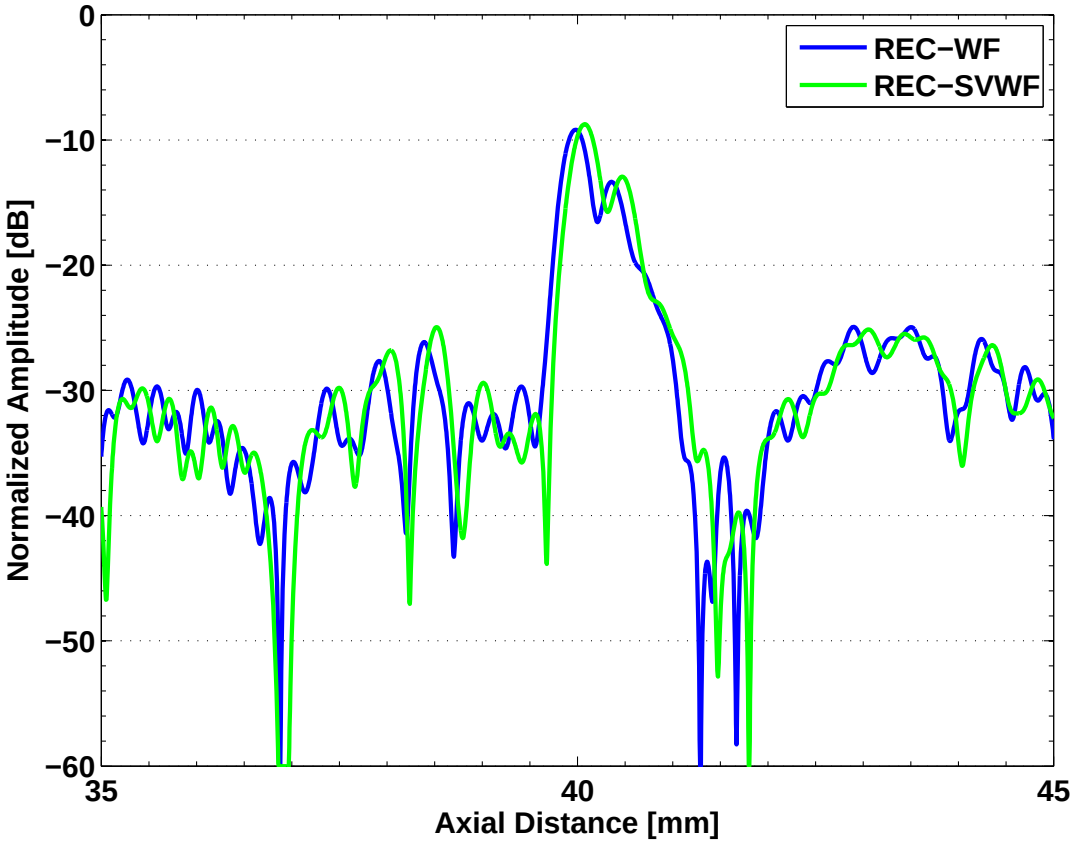

(b)

Figure 4.15: (a) B-mode image and (b) on-axis plot of a 120 μm ATS nylon wire target located at the edge of the -6 dB depth of field before the focus for both conventional Wiener filtering (WF) and spatially varying Wiener filtering (SVWF). In this case, WF refers to the echoes have been compressed with a tungsten wire target that was located at the focus. SVWF refers to the echoes have been compressed with a reference target obtained at the same spatial location (the reference is from a tungsten wire). Image dynamic range = -50 dB.

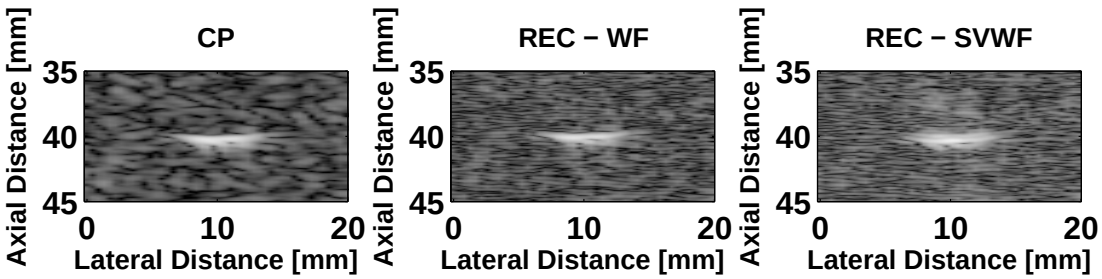

(a)

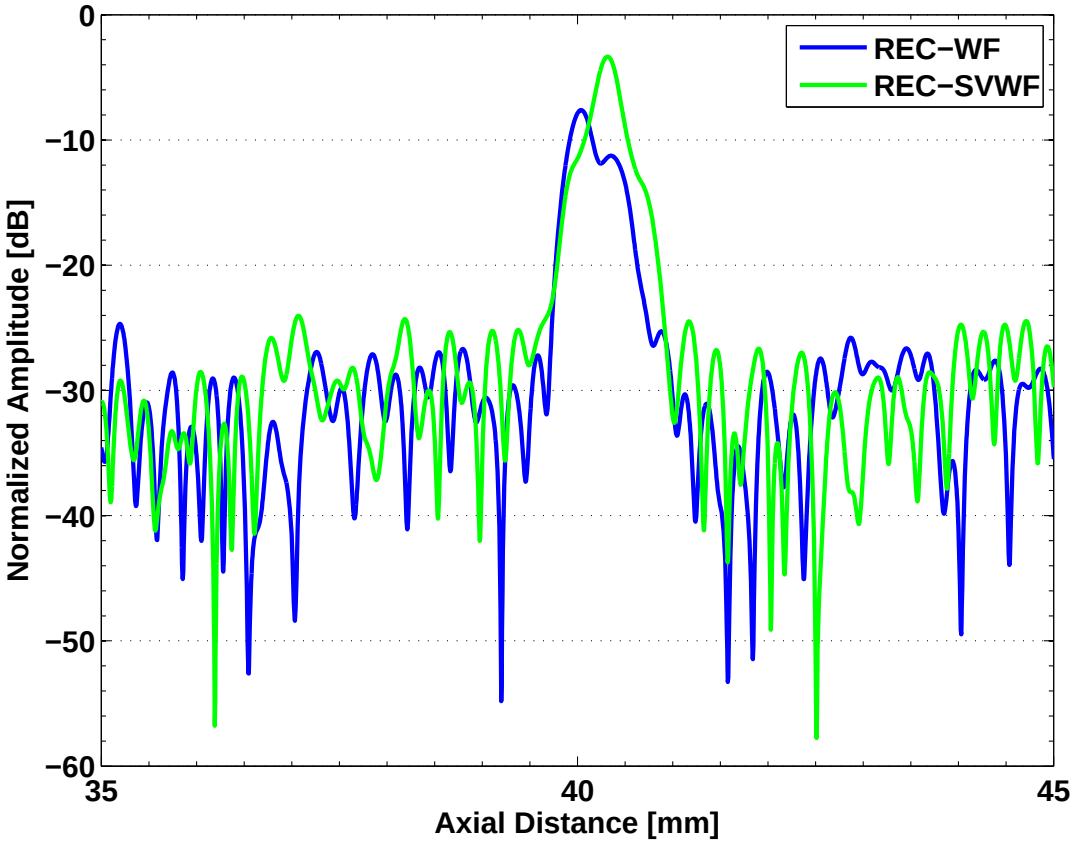

(b)

Figure 4.16: (a) B-mode image and (b) on-axis plot of a 120 μm ATS nylon wire target located at the edge of the -6 dB depth of field before the focus for both conventional Wiener filtering (WF) and spatially varying Wiener filtering (SVWF). In this case, WF refers to the echoes have been compressed with a nylon wire target that was located at the focus. SVWF refers to the echoes have been self-compressed (i.e., the reference is from a nylon wire located at the same depth the target was imaged). Image dynamic range = -50 dB.

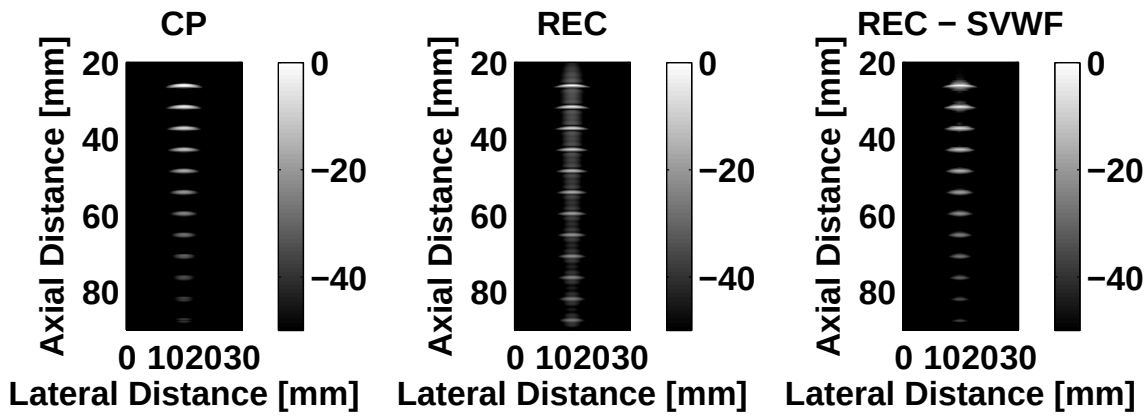

(a)

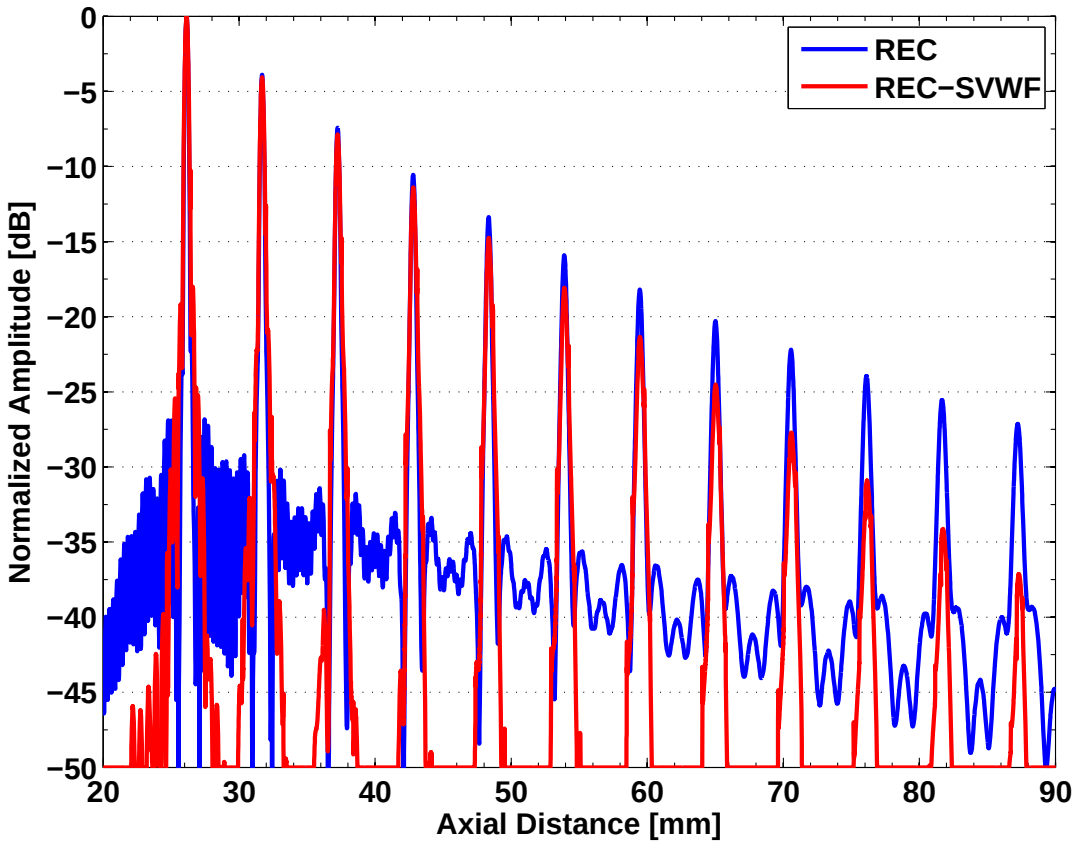

(b)

Figure 4.17: (a) B-mode image and (b) on-axis plot of 12 wire targets for CP, REC and REC-SVWF for a low noise scenario.

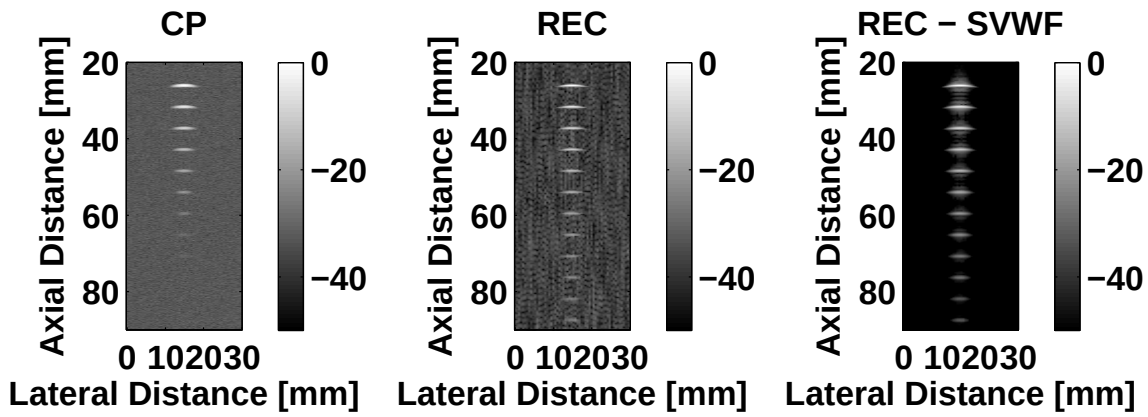

(a)

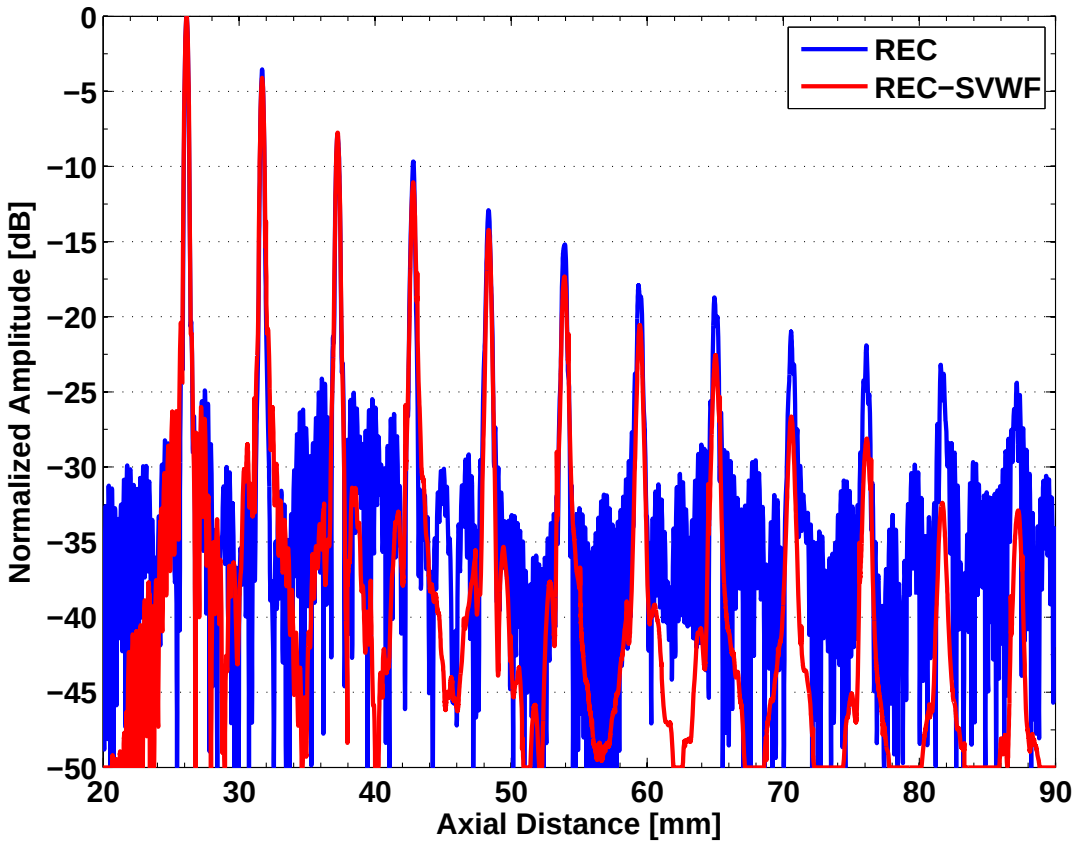

(b)

Figure 4.18: (a) B-mode image and (b) on-axis plot of 12 wire targets for CP, REC and REC-SVWF for a high noise scenario.

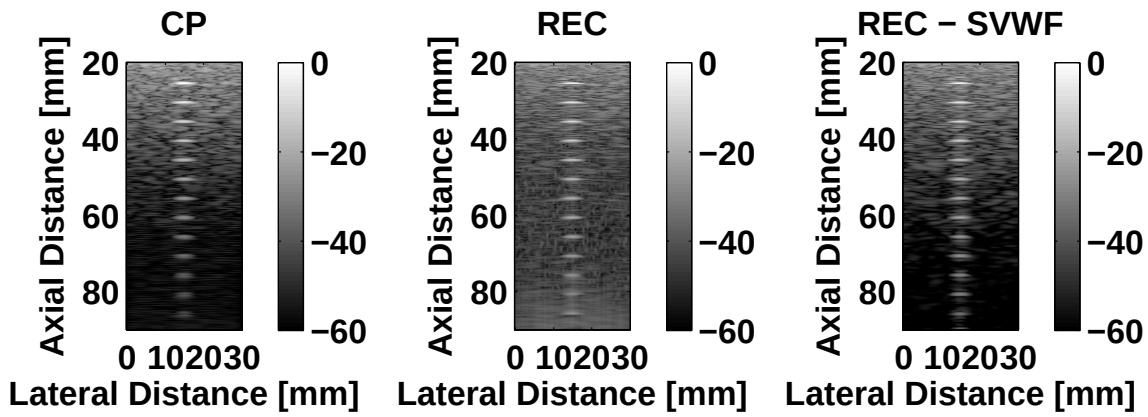

(a)

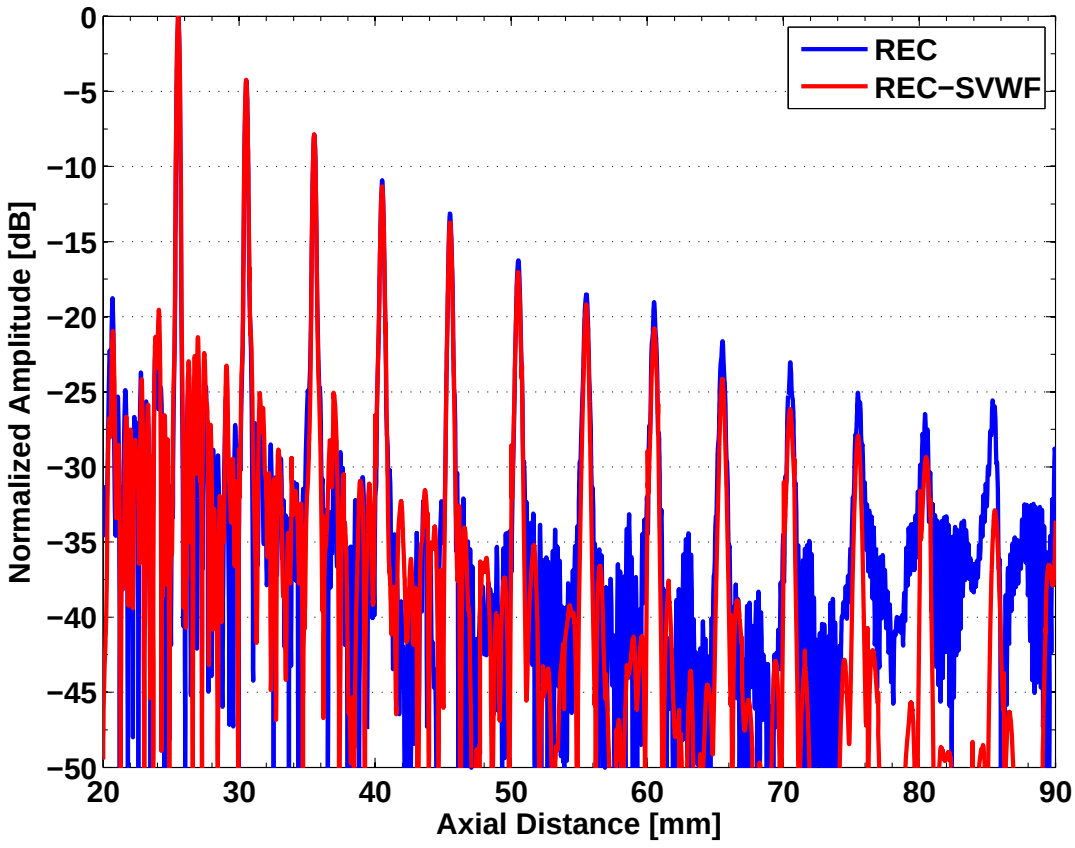

(b)

Figure 4.19: (a) B-mode image and (b) on-axis plot of 12 wire targets buried in tissue-mimicking material for CP, REC and REC-SVWF.

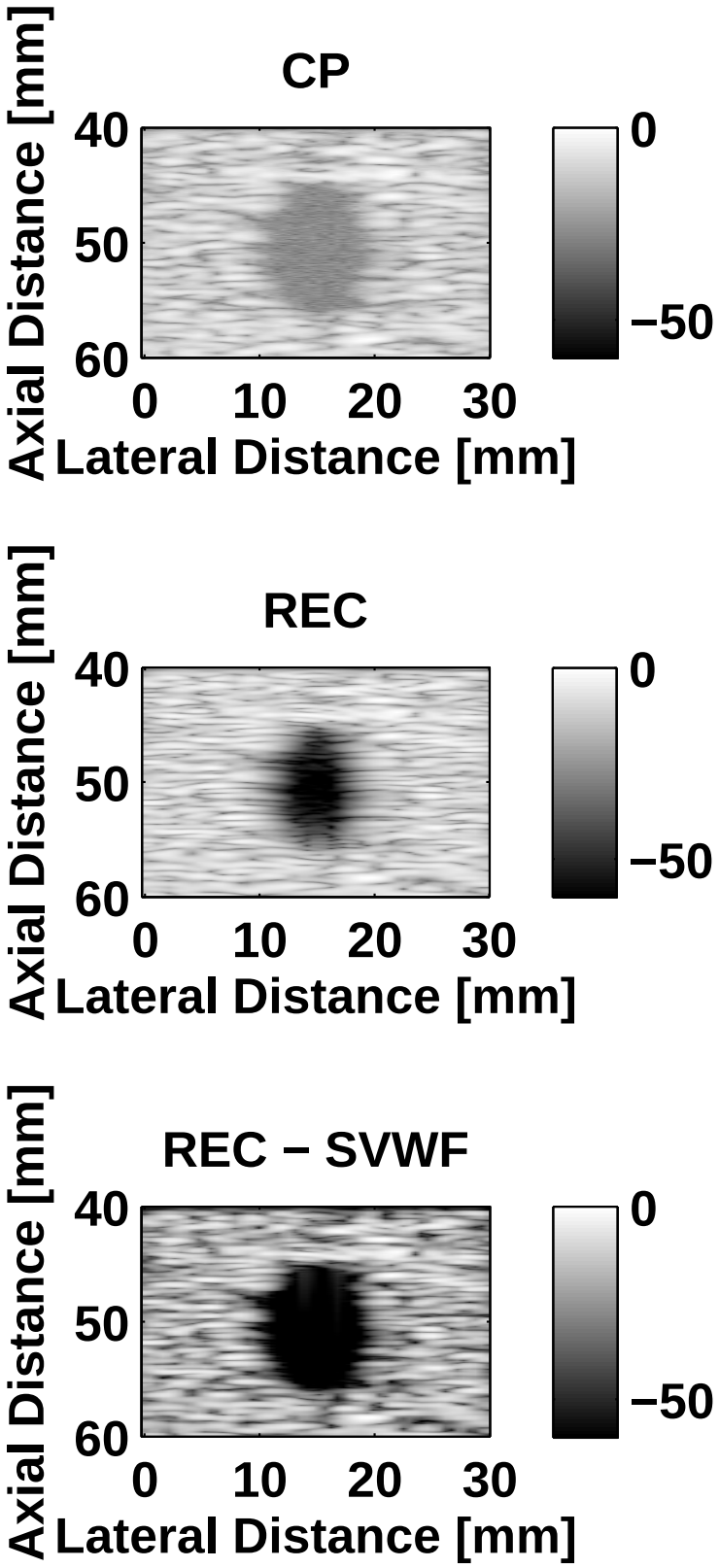

Figure 4.20: B-mode image of a cystic target surrounded by tissue-mimicking material for CP, REC and REC-SVWF.

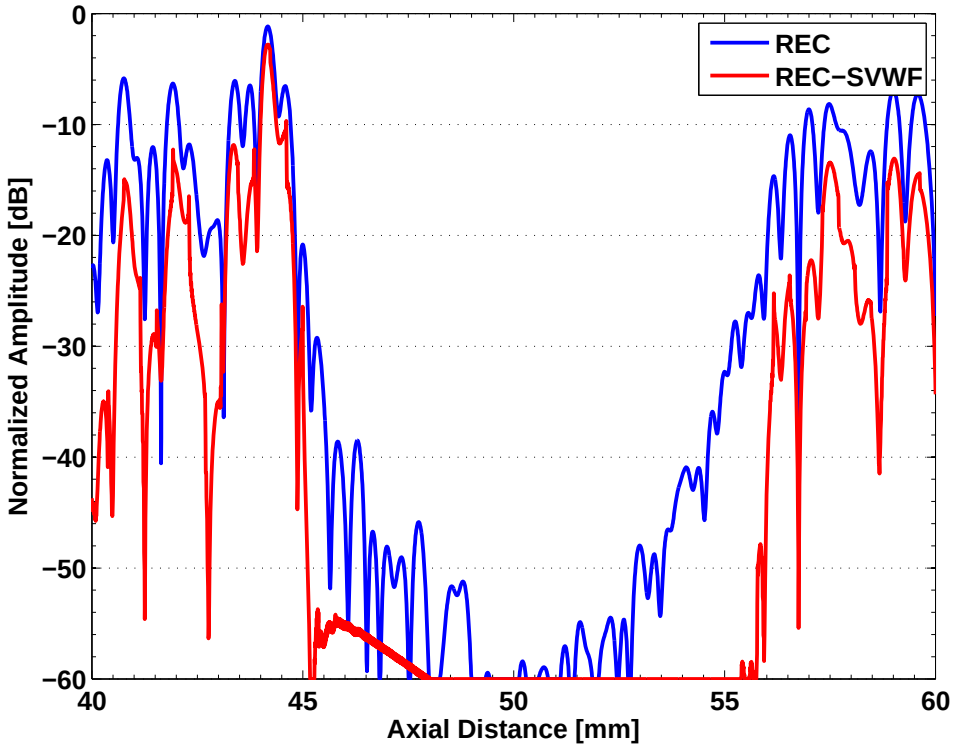

Figure 4.21: On-axis plot of a cystic target surrounded by tissue-mimicking material for REC and REC-SVWF.

Table 4.1: Axial resolution estimates from the MTF for the two compressed outputs: conventional Wiener filtering (WF) and spatially varying Wiener filtering (SVWF) along with CP as a reference for the planar reflector target.

Location	REC-WF (μm)	REC-SVWF (μm)	CP (μm)
-6-dB amplitude before focus	440.3	300.4	431.1
-4-dB amplitude before focus	413.4	301.1	451.7
-2-dB amplitude before focus	346.5	303.4	451.7
focus	302.0	302.0	421.0
-2-dB amplitude after focus	311.9	301.9	420.6
-4-dB amplitude after focus	331.5	301.9	437.2
-6-dB amplitude after focus	376.5	301.2	450.1

Table 4.2: Spatial resolution values determined from the MTF for the conventional Wiener filtering (WF), and the spatially varying Wiener filtering (SVWF). Two different types of references were used: planar reflector and wire target (self-compression). CP results are shown as a reference for the tungsten wire target.

	Reference				
	Planar		Wire		
Location	REC-WF (μm)	REC-SVWF (μm)	REC-WF (μm)	REC-SVWF (μm)	CP (μm)
-6 dB amplitude					
before focus	396.0	426.4	489.8	338.8	569.9
focus	426.4	426.4	434.0	434.0	508.2
-6 dB amplitude					
after focus	422.1	470.9	417.7	412.1	510.3

Table 4.3: Spatial resolution values determined from the MTF for REC with conventional Wiener filtering (WF) and spatially varying Wiener filtering (SVWF) along with CP as a reference for the tungsten wire target. These results are for the low noise scenario.

Target #	REC-WF (μm)	REC-SVWF (μm)	CP (μm)
1	368.9	392.6	658.1
2	401.7	424.8	667.5
3	442.2	458.1	687.1
4	491.8	502.4	718.8
5	554.0	543.3	876.1
6	623.0	581.6	824.5
7	690.5	591.5	910.2
8	753.6	922.1	1015.8
9	839.7	973.4	1121.4
10	922.2	1070.0	1274.3
11	1008.5	1240.5	1430.3
12	1103.7	1103.7	1592.8

Table 4.4: Spatial resolution values determined from the MTF for REC with conventional Wiener filtering (WF) and spatially varying Wiener filtering (SVWF) along with CP as a reference for the tungsten wire target. These results are for the high noise scenario.

Target #	REC-WF (μm)	REC-SVWF (μm)	CP (μm)
1	379.8	388.3	658.1
2	407.5	422.2	667.5
3	443.6	461.1	687.1
4	537.1	526.9	718.8
5	631.4	556.2	876.1
6	697.3	622.9	824.5
7	697.4	640.1	910.2
8	805.6	922.1	1015.8
9	1112.5	881.6	1121.4
10	960.1	1062.0	1274.3
11	1649.1	1158.5	1430.3
12	5607.0	1103.7	1592.8

CHAPTER 5

CONCLUSIONS AND FURTHER OUTLOOK

The goal of this study was to establish some of the practical limitations of the REC technique and to evaluate applications where the REC technique would improve the quality of ultrasound imaging. In this final chapter, the conclusions formulated are summarized and future directions and extensions to the work presented are described.

5.1 Characterization of REC

In Chapter 2, the REC technique was characterized and practical limitations were discussed. Specifically, the detrimental effect of nonlinear distortion on the compression of REC echoes was established. The effects consisted of amplification of the harmonics when the Wiener filter operated near inverse filter mode which resulted in high sidelobe levels being produced. The compression performance was improved by pre-filtering the higher harmonics. Pre-filtering the higher harmonics reduced the sidelobe levels significantly.

Moreover, the practical limitations of the REC technique that were encountered during the course of these studies were assessed. Specifically, the effects of frequency-dependent attenuation and pre-enhanced chirp construction limitations were examined. In terms of attenuation, the main effect evaluated was the center frequency shift and bandwidth loss. It was observed in that study that REC suffered from a larger center frequency shift when compared to CP because of its larger bandwidth. Furthermore, the pre-enhanced chirp was evaluated in terms of center frequency amplitude versus peak amplitude. The findings suggest that, when attempting to increase the resolution by a factor of two, a loss in signal-to-noise ratio was obtained when compared to a linear chirp excitation under the voltage limited scenario. Nonetheless, by exciting a source with a pre-enhanced chirp, an increase in signal-to-noise ratio is obtained when

compared to conventional pulsing because of the larger time-bandwidth product of the coded signal.

Finally, the possible heating of the source when the source was excited with a pre-enhanced chirp was evaluated. It was observed in the heating study that the pre-enhanced chirp did not produce any significant source heating greater than would be achieved with a similar linear chirp. Therefore, it was concluded that heating of the source was not of greater concern using the REC method.

5.2 Applications for REC

In Chapter 3 various applications where the use of the REC technique improved image quality were evaluated.

The first application evaluated was REC-FC. With REC-FC the contrast of ultrasound B-mode images was improved by reducing the speckle variance. This reduction in variance came from subdividing the bandwidth into subbands to generate partially uncorrelated images that could be compounded to improve the contrast. Because REC had a larger bandwidth when compared to conventional methods, the bandwidth was subdivided into more subbands, which increased the amount of speckle reduction that occurred. A major benefit observed for the REC-FC full width case was that there were no significant losses in axial resolution when compared to conventional imaging schemes; however, an improvement in contrast was obtained. Therefore, it would be interesting to evaluate other speckle reduction schemes for the REC-FC full width case. These speckle reduction schemes include speckle reduction geometric filtering, homomorphic deconvolution, anisotropic diffusion, and wavelet denoising and shrinkage. A complete study would apply the same technique to the REC reference image and the CP reference image.

Similarly, the same techniques could be applied to the eREC-FC image obtained. In eREC-FC, all of the frequency compounded images were summed together to the reference image. The eREC-FC technique improved both resolution and contrast when compared to the REC-FC full-width case.

The REC-FC images appeared to have better boundary definition when compared to CP. A simple edge detection scheme was applied in order to verify this assertion.

However, future studies should examine a method that quantifies the apparent edge enhancement obtained by using REC-FC and eREC-FC. Furthermore, the REC-FC technique on an array imaging system could be combined with spatial compounding to improve contrast even further.

The second application evaluated was REC-QUS. With REC-QUS, REC was used to obtain improved parametric images using estimates of ESD. These improved estimates were obtained because the larger bandwidth resulting from REC meant that more information was contained in the power spectrum representing the scattering function. Therefore, a reduction in variance was obtained. Furthermore, the reduction in variance translated into improved contrast of the parametric images of ESD. In addition to obtaining the ESD, the effective acoustic concentration could be obtained. Further studies should examine the REC-QUS technique for improvements in the estimates of the effective acoustic concentration because the effective acoustic concentration is dependent on the initial estimate of ESD. Adding another parameter could be beneficial in the differentiation of tissues. Furthermore, because the ESD results for REC-QUS had a smaller variance when compared to conventional QUS, the effective acoustic concentration results should improve. Therefore, REC-QUS could have the potential to significantly improve the diagnostic capabilities of ultrasound. In addition to reducing the variance, REC-QUS obtained improved estimates of ESD for a smaller axial pixel size. Angular compounding studies demonstrated that improved estimates of ESD can be obtained for a smaller lateral pixel length. Therefore, by combining REC-QUS with angular compounding, the estimates of ESD could be further improved and smaller pixels sizes, both laterally and axially, could be used in parametric imaging.

The significance of smaller pixel sizes could be an increased ability to detect and diagnose smaller lesions. The work involving REC-QUS in this study only utilized phantoms in both simulations and experiments. Studies of REC-QUS where the ability to differentiate between different kinds of tumors should be evaluated in future studies.

Finally, a study where the analysis bandwidth was partitioned into smaller bands so that the power spectrum could be evaluated using different frequency scales would be interesting. Scatterer sensitivity to particular frequencies varies with scatterer size. Therefore, by splitting the spectrum into different scales, several images could be gener-

ated that might be sensitive to different scales of scatterers as if the interrogated tissue was being imaged by multiple sources.

5.3 Spatially Varying Weiner Filter

In Chapter 4, the detrimental effect that the spatially varying impulse response had on the compression of REC echoes was examined and quantified. Furthermore, several schemes were devised and assessed to mitigate the spatially varying effect in the compression scheme. Specifically, schemes that partially corrected for the diffraction, frequency-dependent scattering, and both diffraction and frequency-dependent scattering locally were evaluated. Improved results in terms of sidelobe reduction were obtained, but only when the targets were isolated (i.e., no speckle content surrounded the target). When the target was isolated echoes from the targets were used as references to self-compress the echoes and improve the compression performance. However, when speckle was present, the improvements were nearly nonexistent because it was hard to ascertain the frequency-dependent scattering function of the object.

A different spatially varying Wiener filter that compensated for the $\overline{eSNR}$ locally was devised. The spatially varying filter created a signal strength map to improve the compression performance. The spatially varying Wiener filter improved image contrast and improved the $eSNR$ in deeper regions of the object imaged. The tradeoff was a slight degradation in resolution and a slight increase in sidelobe levels in order to improve the eSNR and image quality as a function of depth.

RELEVANT PUBLICATIONS

The work presented herein has been funded by National Institutes of Health (NIH R21 EB006741) and has been directed by Prof. Michael L. Oelze. Throughout the tenure of this four-year project, the following manuscripts and presentations regarding this work have been published:

- (Invited) D. P. Hruska, J. R.Sanchez, and M. L. Oelze, "Improved diagnostics through quantitative ultrasound imaging," *Proceedings of the 2009 IEEE Engineering in Medicine and Biology Society*, pp. 1956-1959, 2009.

- J. R. Sanchez, D. Pocci, and M. L. Oelze, "Use of a novel coded excitation scheme to improve spatial and contrast resolution of quantitative ultrasound imaging," *IEEE Trans. Ultrason. Ferroelect. Freq. Contr.*, vol. 56, 10, pp. 2111-2123, Oct. 2009.

- J. R. Sanchez and M. L. Oelze, "An ultrasonic imaging speckle-suppression and contrast-enhancement technique by means of frequency compounding and coded excitation," *IEEE Trans. Ultrason. Ferroelect. Freq. Contr.*, vol. 56, pp. 1327-1339, Jul. 2009.

- J. R. Sanchez, D. Pocci, and M. L. Oelze, "On the use of coded excitation and pulse compression to reduce estimate errors of average scatterer diameters obtained from ultrasonic backscatter," *Journal of the Acoustical Society of America*, vol. 125, pp. 2513, 2009.

- J. R. Sanchez and M. L. Oelze, "Improvements in compression of coded excitation echoes by using a spatially varying Wiener filter," *Journal of the Acoustical Society of America*, vol. 125, pp. 2513, 2009.

- (Invited) M. L. Oelze and J. R. Sanchez, "Improving biomedical ultrasonic imaging systems through coded excitation and pulse compression," *Journal of the Acoustical Society of America*, vol. 124, pp. 2473, 2008.

- J. R. Sanchez, D. Pocci, and M. L. Oelze, "Using resolution enhancement compression to reduce variance of scatterer size estimates from ultrasonic backscattered signals," *Proceedings of the 2008 IEEE Ultrasonics Symposium*, pp. 36-39, 2008.

- J. R. Sanchez and M. L. Oelze, "An ultrasonic imaging speckle suppression and contrast enhancement technique by means of frequency compounding and coded excitation," *Proceedings of the 2007 IEEE Ultrasonics Symposium*, pp. 464-467, 2007.

- J. R. Sanchez and M. L. Oelze, "An ultrasonic imaging speckle suppression technique by means of frequency compounding and coded excitation," *Journal of the Acoustical Society of America*, vol. 121, pp. 3154, 2007.

REFERENCES

[1] R. A. Harris, D. H. Follets, M. Halliwell, and P. N. T. Wells, "Ultimate limits in ultrasonic imaging resolution," *Ultrasound in Med. &. Biol.*, pp. 547-558, 1991.

[2] J. F. Zachary, J. M. Sempsrott, L. A. Frizzell, D. G. Simpson, and W. D. O'Brien, Jr., "Superthreshold behavior and threshold estimation of ultrasound-induced lung hemorrhage in adult mice and rats," *IEEE Trans. Ultrason., Ferroelectr., Freq. Control*, vol. 48, pp. 581-592, 2001.

[3] R. Y. Chiao and H. Xiaohui, "Coded excitation for diagnostic ultrasound: A system developer's perspective," *IEEE Trans. Ultrason., Ferroelectr., Freq. Contol*, vol. 52, pp. 160-170, Feb. 2005.

[4] M. O'Donnell and W. Yao, "Coded excitation for synthetic aperture ultrasound imaging," *IEEE Trans. Ultrason., Ferroelectr., Freq. Control*, vol. 52, pp. 171-176, Feb. 2005.

[5] T. Misaridis and J. A. Jensen, "Use of modulated excitation signals in medical ultrasound. Part I: Basic concepts and expected benefits," *IEEE Trans. Ultrason., Ferroelectr. Freq. Control*, vol. 52, pp. 177-191, Feb. 2005.

[6] C. E. Cook and W. M. Siebert, "The early history of pulse compression radar," *IEEE Trans. Aerospace and Elec. Systems*, vol. 24, no. 6, pp. 825-833, Nov. 1988.

[7] Y. Takeuchi, "An investigation of a spread energy method for medical ultrasound systems - Part one: Theory and investigation," *Ultrasonics*, vol. 17, pp. 175-182, 1979.

[8] Y. Takeuchi, "An investigation of a spread energy method for medical ultrasound systems - Part two: Proposed system and possible problems," *Ultrasonics*, vol. 17, pp. 175-182, 1979.

[9] M. O'Donnell, "Coded excitation system for improving the penetration of real-time phased-array imaging systems," *IEEE Trans. Ultrason., Ferroelectr. Freq. Control*, vol. 39, pp. 341-351, 1992.

[10] N. A. H. K. Rao, "Investigation of a pulse compression technique for medical ultrasound: A simulation study," *Med. Biol. Eng. Comp.*, vol. 32, pp. 181188, 1994.

[11] M. Pollakowski and H. Ermert, "Chirp signal matching and signal power optimization in pulse-echo mode ultrasonic nondestructive testing," *IEEE Trans. Ultrason., Ferroelectr., Freq. Control*, vol. 41, pp. 655659, 1994.

[12] J. Shen and E. S. Ebbini, "A new coded-excitation ultrasound imaging system - Part I: Basic principles," *IEEE Trans. Ultrason., Ferroelectr., Freq. Control*, vol. 43, pp. 131-140, Jan. 1996.

[13] J. Shen and E. S. Ebbini, "A new coded-excitation ultrasound imaging system - Part II: Operator design," *IEEE Trans. Ultrason., Ferroelec., Freq. Contr.*, vol. 43, pp. 141-148, Jan. 1996.

[14] C. Passmann and H. Ermert, "A 100-MHz ultrasound imaging system for dermatological and ophtalmological diagnostics," *IEEE Trans. Ultrason., Ferroelec., Freq. Contr.*, vol 43, pp. 545-552, Jul 1996.

[15] B. Haider, P. A. Lewin, and K. E. Thomenius, "Pulse elongation and deconvolution filtering for medical ultrasonic imaging," *IEEE Trans. Ultrason., Ferroelec., Freq. Contr.*, vol 45, pp. 98113, 1998.

[16] T Misaridis and J. A. Jensen, "Use of modulated excitation signals in medical ultrasound. Part II: Design and performance for medical imaging applications," *IEEE Trans. Ultrason. Ferroelectr. Freq. Control*, vol. 52, pp. 192-207, Feb. 2005.

[17] T Misaridis and J. A. Jensen, "Use of modulated excitation signals in medical ultrasound. Part III: High frame rate imaging," *IEEE Trans. Ultrason. Ferroelectr. Freq. Control*, vol. 52, pp. 208-219, Feb. 2005.

[18] M. L. Oelze, "Bandwidth and resolution enhancement through pulse compression," *IEEE Trans. Ultrason. Ferroelectr. Freq. Control*, vol. 54, pp. 768-781, Apr. 2007.

[19] J. K. Tsou, J. Liu, and M. F. Insana, "Modeling and phantom studies of ultrasonic wall shear rate measurements using coded excitation," *IEEE Trans. Ultrason. Ferroelectr. Freq. Control*, vol. 53, pp. 724-734, 2006.

[20] L. E. . Kinsler, A. R. Frey, A. B. Coppens, and J. V. Sanders. *Fundamental of Acoustics*. New York, NY: John Wiley & Sons, Inc., 1999.

[21] M. F. Hamilton and D. T. Blackstock, *Nonlinear Acoustics*. San Diego, CA: Academic Press, 1998.

[22] R. T. Beyer, *Nonlinear Acoustics*. Woodbury, NY: Acoustical Society of America Press, 1997.

[23] J. Borsboom, T. C. Chien, A. Bouakaz, N. de Jong, "Nonlinear coded excitation method for contrast imaging," *Ultrasonics Symposium*, vol. 2, pp. 1729-1732, Oct. 2001.

[24] J. Borsboom, T. C. Chien, N. de Jong, "Nonlinear coded excitation method for ultrasound contrast imaging," *Ultrasound Med. Biol.*, vol. 29, pp. 277-284, Feb. 2003.

[25] T. A. Bigelow and W. D. O'Brien, Jr., "Experimental evaluation of indicators of nonlinearity for use in ultrasound transducer characterizations," *Ultrasound Med. Biol.*, vol. 28, pp. 1509-1520, 2002.

[26] J. Beutel, H. L. Kundel, and R. L. Van Metter, *Handbook of Medical Imaging.* Bellingham, WA: SPIE Press, 2000.

[27] T. D. Mast, "Empirical relationships between acoustic parameters in human soft tissues," *Acoustics Res. Lett.*, vol. 1, pp. 37-42, 2000.

[28] R. C. Cobbold, *Foundations of Biomedical Ultrasound.* New York, NY: Oxford University Press, 2007.

[29] F. W. Reckling and W. L. Dillon, "The bone-cement interface temperature during total joint replacement," *J. Bone and Joint Surg.*, vol. 59, pp. 80-82, 1977.

[30] R. Krimholtz, D. A. Leedom, and G. L. Matthaei, "New equivalent circuits for elementary piezoelectric transducers," *Electronics Lett.*, vol. 6, pp. 398-399, 1970.

[31] R. S. Weis and T. K. Gaylord, "Lithium niobate: Summary of physical properties and crystal structure ," *Applied Physics A: Materials Science & Processing*, vol. 37, pp.191-203, Aug. 1985.

[32] C. Burckhardt, "Speckle in ultrasound B-Mode scans," *IEEE Trans. Sonics Ultrason.*, vol. SU-25, pp. 1-6, Jan. 1978.

[33] A. Webb, *Introduction to Biomedical Imaging.* Hoboken, NJ: John Wiley & Sons, Inc., 2003.

[34] M. S. Patterson and F. S. Foster, "The improvement and quantitative assessment of B-mode images produced by an annular array/cone hybrid," *Utrason. Imag.*, vol. 5, pp. 195-213, 1983.

[35] "GE Healthcare-Applications-Oncology-Ultrasound," March 21, 2005. [Online]. Available: http://www.gehealthcare.com/usen/oncology/products/ultrasound.html,[Sep 7, 2009].

[36] J. C. Bamber and C. Daft, "Adaptive filtering for reduction of speckle in ultrasound pulse-echo images," *Ultrasonics*, vol. 24, pp. 41-44, Jan. 1986.

[37] Y. Chen, R. Yin, P. Flynn, and S. Broschat, "Aggressive region growing for speckle reduction in ultrasound images," *Pattern Recognit. Lett.*, vol. 24, pp. 667-691, 2003.

[38] D. C. Crawford, D. S. Bell, and J. C. Bamber, "Compensation for the signal processing characteristics of ultrasound B-mode scanners in adaptive speckle reduction," *Ultrasound Med. Biol.*, vol. 19, pp. 469-485, 1993.

[39] V. Dutt and J. F. Greenleaf, "Adaptive speckle reduction filter for log compressed B-scan images," *IEEE Trans. Med. Imag.*, vol. 15, pp. 802-813, Dec. 1996.

[40] T. Loupas, W. N. McDicken, and P. L. Allan, "Adaptive weighted median filter for speckle suppression in medical ultrasound images," *IEEE Trans. Circuits Syst.*, vol. 36, pp. 129-135, Jan. 1989.

[41] J. A. Jensen and S. Leeman, "Nonparametric estimation of ultrasound pulses," *IEEE Trans. Biomed. Eng.*, vol. 41, pp. 929-936, Oct. 1994.

[42] W. Yeoh and C. Zhang, "Constrained least squares filtering algorithm for ultrasound image deconvolution," *IEEE Trans. Biomed. Eng.*, vol. 53, pp. 2001-2007, Oct. 2006.

[43] O. V. Michailovich and A. Tannenbaum, "Despeckling of medical ultrasound images," *IEEE Trans. Ultrason. Ferroelectr. Freq. Control*, vol. 53, pp. 64-78, Jan. 2006.

[44] Y. Yue, M. M. Croitoru, A. Bidani, J. B. Zwischenberger, and J. W. Clark Jr., "Nonlinear multiscale wavelet diffusion for speckle suppression and edge enhancement in ultrasound images," *IEEE Trans. Med. Imag.*, vol. 25, pp. 297-311, Mar. 2006.

[45] S. K. Jespersen, J. E. Wilhjelm, and H. Sillesen, "Multi-angle compound imaging," *Ultrason. Imag.*, vol. 20, pp. 81-102, 1998.

[46] G. E. Trahey, S. W. Smith, and O. T. von Ramm, "Speckle pattern correlation with lateral aperture translation: experimental results and implications for spatial compounding," *IEEE Trans. Ultrason. Ferroelectr. Freq. Control*, vol. UFFC-33, pp. 257-264, May 1986.

[47] A. R. Groves and R. N. Rohling, "Two-dimensional spatial compounding with warping," *Ultras. in Med. & Biol.*, vol. 30, No. 7, pp. 929-942, 2004.

[48] P. Soler, G. Delso, N. Villain, E. Angelini, and I. Bloch, "Superresolution spatial compounding techniques with application to 3D breast ultrasound imaging," *Proc. of SPIE*, vol. 6147, Mar. 2006.

[49] J. G. Abbot, and F. L. Thurstone, "Acoustic speckle: Theory and experimental analysis," *Ultrason. Imag.*, vol. 1, pp. 303-324, 1979.

[50] S. M. Gehlbach and F. G. Sommer, "Frequency diversity speckle processing," *Ultrason. Imag.*, vol. 9, pp. 92-105, Apr. 1987.

[51] P. A. Magnin, O. T. von Ramm, and F. L. Thurstone, "Frequency compounding for speckle contrast reduction in phased array images," *Ultrason. Imag.*, vol. 4, pp. 267-281, 1982.

[52] H. E. Melton and P. A. Magnin, "A-Mode speckle reduction with compound frequencies and compound bandwidths," *Ultrason. Imag.*, vol. 6, pp. 159-173, 1984.

[53] V. L. Newhouse, N. M. Bilgutay, J. Saniie, and E. S. Furgason, "Flaw-to-grain echo enhancement by split-spectrum processing," *Ultrason. Imag.*, pp. 59-68, Mar 1982.

[54] G. E. Trahey, J. W. Allison, S. W. Smith, and O. T. von Ramm,, "A quantitative approach to speckle reduction via frequency compounding," *Ultrason. Imag.*, vol. 8, pp. 151-164, July 1986.

[55] F. L. Lizzi, M. E. Elbaum, and E. Feleppa, "Frequency diversity for image enhancement," *U.S. Patent 4561019*, Dec. 24, 1985.

[56] P. F. Stetson, F. G. Sommer, and A. Macovski, "Lesion contrast enhancement in medical ultrasound imaging," *IEEE Trans. Med. Imag.*, vol. 16, pp. 416-425, Aug. 1997.

[57] S. W. Smith, R. F. Wagner, J. M. Sandrik, and H. Lopez, "Low contrast detectability and contrast/detail analysis in medical ultrasound," *IEEE Trans. Sonics and Ultrason.*, vol. 30, pp. 164-173, 1983.

[58] S. W. Smith, H. Lopez, and W. J. Bodine, Jr., "Frequency independent ultrasound contrast-detail analysis," *Ultrasound in Med. & Biol.*, vol. 11, pp. 467-477, 1985.

[59] R. F. Wagner, S. W. Smith, J. M. Sandrik, and H. Lopez, "Statistics of speckle in ultrasound B-Scans," *IEEE Trans. Sonics Ultrason.*, vol. 30, pp. 156-163, May 1983.

[60] J. A. Jensen, "A model for the propagation and scattering of ultrasound tissue," *J. Acoust. Soc. Am.*, vol. 89, pp. 182-190, Jan. 1991.

[61] T. A. Bigelow and W. D. O'Brien, Jr. "Scatterer size estimation in pulse-echo ultrasound using focused sources: theoretical approximations and simulation analysis," *J. Acoust. Soc. Am.*, vol. 116, pp. 578-593, 2004.

[62] P. M. Shankar, V. A. Dumane, C. W. Piccoli, J. M. Reid, F. Forsberg, and B. B. Goldberg, "Computer-aided classification of breast masses in ultrasonic B-scans using a multiparameter approach," *IEEE Trans. Ultrason. Ferroelect. Freq. Contr.*, vol. 50, 2003.

[63] F. L. Lizzi, M. Greenebaum, E. J. Feleppa, M. Elbaum, and D. J. Coleman, "Theoretical framework for spectrum analysis in ultrasonic characterization," *J. Acoust. Soc. Am.*, vol. 73, pp. 1366-1373, Jan. 1983.

[64] D. J. Coleman, and F. L. Lizzi, "Computerized ultrasonic tissue characterization of occular tumors," *Am. J. Ophthal.*, vol. 96, pp. 165-175, 1983.

[65] E. J. Feleppa, F. L. Lizzi, D. J. Coleman, and M. M. Yaremko, "Diagnostic spectrum analysis in ophtalmology: A physical perspective," *Ultrasound Med. Biol.*, vol. 12, pp. 623-631, 1986.

[66] F. L. Lizzi, M. Ostromogilsky, E. J. Feleppa, M. C. Rorke, and M. M. Yaremko, "Relationship of ultrasonic spectral parameters to features of tissue microstructures," *IEEE Trans. Ultrason., Ferroelectr., Freq. Control*, vol. 33, pp. 319-329, 1986.

[67] R. H. Silverman, D. J. Coleman, F. L. Lizzi, J. H. Torpey, J. Driller, T. Iwamoto, S. E. P. Burgess, and A. Rosado, "Ultrasonic tissue characterization and histopathology in tumor xenografts following ultrasonically induced hyperthermia," *Ultrasound Med. Biol.*, vol. 12, pp. 639-645, 1986.

[68] D. J. Coleman, R. H. Silverman, M. J. Rondeau, F. L. Lizzi, J. W. McLean, and F. A. Jakobiec, "Correlations of acoustic tissue typing of malignant-melanoma and histopathologic features as a predictor of death," *Am. J. Ophthal.*, vol. 110, pp. 380-388, 1990.

[69] D. J. Coleman, R. H. Silverman, M. J. Rondeau, J. A. Coleman, D. Rosberger, R. M. Ellsworth, and F. L. Lizzi, "Ultrasonic tissue characterization of uveal melanoma and prediction of patient survival after enucleation and brachytherapy," *Am. J. Ophthal.*, vol. 112, pp. 682-688, 1991.

[70] R. L. Romijn, J. M. Thijssen, B. J. Oosterveld, and A. M. Verbeek, "Ultrasonic differentiation of intraocular melanomas: Parameters and estimation methods," *Ultrasound Imag.*, vol. 13, pp. 27-55, 1991.

[71] F. L. Lizzi, M. Astor, T. Liu, C. Deng, D. J. Coleman, and R. H. Silverman, "Ultrasonic spectrum analysis for tissue assays and therapy evaluation," *Int. J. Imaging Syst. Technol.*, vol. 8, pp. 3-10, 1997.

[72] R. C. Waag, P. P. K. Lee, H. W. Persson, E. A. Schenk, and R. Gramiak "Frequency-dependent angle scattering of ultrasound by liver," *J. Acoust. Soc. Am.*, vol. 72, pp. 343-352, Jan 1982.

[73] F. L. Lizzi, D. L. King, M. C. Rorke, M. Ostromogilsky, M. M. Yaremko, E. J. Feleppa and P. Wai, "Comparison of theoretical scattering results and ultrasonic data from clinical liver examinations," *Ultrasound Med. Biol.*, vol. 14, pp. 377-385, 1988.

[74] M. F. Insana, J. G. Wood, and T. J. Hall, "Identifying acoustic scattering sources in normal renal parenchyma in vitro by varying arterial and ureteral pressures," *Ultrasound Med. Biol.*, vol. 18, pp. 587-599, 1992.

[75] J. A. Zagzebski, Z. Flu, and L. X. Xao, "Quantitative ultrasound imaging: In Vivo results in normal liver," *Ultrasound Imag.*, vol. 15, pp. 335-351, 1993.

[76] E. J. Feleppa, A. Kalisz, J. B. Sokil-Melgar, F. L. Lizzi, L. Tian, A. L. Rosado, M. C. Shao, W. R. Fair, W. Yu, M. S. Cookson, V. .E Reuter, and W. D. .W Heston, "Typing of prostate tissue by ultrasonic spectrum analysis," *IEEE Trans. Ultrason. Ferroelect. Freq. Control*, vol. 43, pp. 609-619, Jul 1996.

[77] E. J. Feleppa, T. Liu, A. Kalisz, M. C. Shao, N. Fleshner,and V. Reuter, "Ultrasonic spectral-parameter imaging of the prostate," *Int. J. Imaging Syst. Technol.*, vol. 8, pp. 11-25, 1997.

[78] F. T. D'Astous and F. S. Foster, "Frequency dependence of ultrasound attenuation and backscatter in breast tissue," *Ultrasound Med. Biol.*, vol. 12, pp. 795 - 808, 1986.

[79] R. M. Golub, R. E. Parsons, B. Sigel, E. J. Feleppa, J. Justin, H. A. Zaren, M. Rorke, J. Sokil-Melgar, and H. Kimitsuki, "Differentiation of breast tumors by ultrasonic tissue characterization," *J. Ultrasound Med.*, vol. 12, pp. 601-608, 1993.

[80] K. A. Topp, J. F. Zachary, and W. D. O'Brien, Jr., "Quantifying B-mode images of in vivo rat mamary tumor with frequency dependence of backscatter," *J. Ultrasound Med.*, vol. 20, pp. 605-612, 2001.

[81] M. L. Oelze, J. F. Zachary, and W. D. O'Brien, Jr., "Parametric imaging of rat mamammary tumors in vivo for purposes of tissue characterization," *J. Ultrasound Med.*, vol. 21, pp. 1201-1210, 2002.

[82] M. L. Oelze, J. F. Zachary, and W. D. O'Brien, Jr., "Characterization of tissue microstructure using ultrasonic backscatter: theory and technique optimization using a Gaussian form factor," *J. Acoust. Soc. Am.*, vol. 112, pp. 1202-1211, 2002.

[83] M. L. Oelze, J. F. Zachary, and W. D. O'Brien, Jr., "Differentiation and characterization of mammary fibroadenomas and 4T1 Carcinomas using ultrasound parametric imgaing," *IEEE Trans. Med. Imag.*, vol. 23, pp. 764-771, 2004.

[84] M. L. Oelze and J. F. Zachary, "Examination of cancer in mouse models using high frequency quantitative ultrasound," *Ultrasound Med. Biol.*, vol 32, pp. 1639-1648, 2006.

[85] L. Bridal, P. Fornès, P. Bruneval, G. Berger, "Parametric (Integrated backscatter and attenuation) images constructed using backscattered radio frequency signals (25-56 MHz) from human aortae in vitro," *Ultrasound Med. Biol.*, vol. 23, pp. 215-229, 1997.

[86] A. Nair, B. D. Kuban, N. Obuchowski, D. G Vince, "Assessing spectral algorithms to predict atherosclerotic plaque composition with normalized and raw intravascular ultrasound data," *Ultrasound Med. Biol.*, vol. 27, pp. 1319-1331, 2001.

[87] M. F. Insana, "Modeling acoustic backscatter from kidney microstructure using an anisotropic correlation function," *J. Acoust. Soc. Am.*, vol. 97, pp. 649655, 1995.

[88] M. L. Oelze and W. D. O'Brien, Jr., "Defining optimal axial and lateral resolution for estimating scatterer properties from volumes using ultrasound backscatterer," *J. Acoust. Soc. Am.*, vol. 115, pp. 3226-3234, June 2004.

[89] S. G. Kanzler, and M. L. Oelze, "Improved scatterer size estimation using backscatter coefficient measurements with coded excitation and pulse compression," *J. Acoust. Soc. Am.*, vol. 123, pp. 4599-4607, June 2008.

[90] P. Chaturvedi and M. F. Insana, "Error bounds on ultrasonic scatterer size estimates," *J. Acoust. Soc. Am.*, vol. 100, pp. 392-399, 1996.

[91] M. F. Insana, R. F. Wagner, D. G. Brown, and T. J. Hall, "Describing small-scale structure in random media using pulse-echo ultrasound," *J. Acoust. Soc. Am.*, vol. 87, pp. 179-192, 1990.

[92] M. F. Insana and T. J. Hall, "Parametric ultrasound imaging from backscatter coefficient measurements: Image formation and interpretation," *Ultrason. Imaging*, vol. 12, pp. 245-267, 1990.

[93] J. A. Jensen, "A model for the propagation and scattering of ultrasound tissue," *J. Acoust. Soc. Am.*, vol. 89, pp. 182-190, Jan. 1991.

[94] D. Nicholas, "Evaluation of backscattering coefficients for excised human tissues: Results, interpretation, and associated measurements," *Ultrasound Med. Biol.*, vol. 8, pp. 17-28, 1982.

[95] D. K. Nassiri and C. R. Hill, "The use of angular scattering measurements to estimate structural parameters of human and animal tissues," *J. Acoust. Soc. Am.*, vol. 79, pp. 2048-2054, Jan. 1986.

[96] M. F. Insana and T. J. Hall, "Parametric ultrasound imaging from backscatter coefficient measurements: Image formation and interpretation," *Ultrason. Imaging*, vol. 12, pp. 245-267, 1990.

[97] K. Raum and W. D. O'Brien, Jr., "Pulse-echo field distribution measurement technique for high-frequency ultrasound sources," *IEEE Trans. Ultrason. Ferroelect. Freq. Contr.*, vol. 44, pp. 810-815, 1997.

[98] K A. Wear, T. A Stiles, G. R. Frank, E. L. Madsen, F. Cheng, E. J. Feleppa, C. S. Hall, B. S. Kim, P. Lee, W. D. O'Brien, Jr., M. L. Oelze, B. I. Raju, K. K. Shung, T. A. Wilson, and J. R. Yuan, "Interlaboratory comparison of ultrasonic backscatter coefficient measurements from 2 to 9 MHz," *J. Ultrasound Med.*, vol. 24, pp. 1235-1250, 2005.

[99] E. L. Madsen, F. Dong, G. R. Frank, B. S. Garra, K. A. Wear, T. A. Wilson, J. A. Zagzebski, H. L. Miller, K. K. Shung, S. H. Wang, E. J. Feleppa, T. Liu, W. D. O'Brien, Jr., K. A. Topp, N. T. Sanghvi, A. V. Zaitsev, T. J. Hall, J. B. Fowlkes, O. D. Kripfgans, and J. G. Miller "Interlaboratory comparison of ultrasonic backscatter, attenuation, and speed measurements," *J. Ultrasound Med.*, vol. 18, pp. 615-631, 1999.

[100] J. J. Faran, "Sound scattering by solid cylinders and spheres," *J. Acoust. Soc. Am.*, vol. 23, pp. 405-418, 1951.

[101] R. Hickling, "Analysis of Echoes from a Solid Elastic Sphere in Water," *J. Acoust. Soc. Am.*, vol. 34, pp. 1582-1592, 1962.

[102] G. E. Tupholme, "Generation of acoustic pulses by baffled plane pistons," *Mathematika*, vol. 16, pp. 209-224, 1969.

[103] P. R. Stepanishen, "Transient radiation form pistons in an infinite planer baffle," *J. Acost. Soc. Am.*, vol. 49 pp. 1629-1638, 1971.

[104] P. R. Stepanishen, "An approach to computing the time-dependent interaction forces and mutual radiation impedances between pistons and a rigid planar baffle,"' *J. Acost. Soc. Am.*, vol. 49 pp. 283-292, 1971.

[105] J. A. Ketterling and F. L. Lizzi, "Time-domain pressure response of arrays with periodic excitation," *J. Acoust. Soc. Am.*, vol. 114, pp. 48-51, July 2003.

[106] P. Penttinen, and M. Luukkala, "The impulse response and pressure nearfield of a curved ultrasonic radiator," *J. Phys.*, vol. 9, pp. 1547-1557, 1976.

[107] M. Arditi, F. S. Foster, and J. W. Hunt, "Transient fields of concave annular arrays," *Ultrason. Imaging*, vol. 3, pp. 37-61, 1981.

[108] J. A. Jensen, "Field: A program for simulating ultrasound systems," *Medical and Biological Engineering and Computing*, vol. 34, pp. 351-353, 1996.

[109] J. A. Jensen and N. B. Svendsen, "Calculation of pressure fields from arbitrarily shaped, apodized, and excited ultrasound transducers," *IEEE Trans. Ultrason., Ferroelec., Freq. Contr.*, vol. 39, pp. 262-267, 1992.